1-1-2021

Nonreciprocity Applications in Acoustics and Microfluidic Systems

Masoud Naghdi
University of Mississippi

NONRECIPROCITY APPLICATIONS IN ACOUSTICS AND MICROFLUIDIC SYSTEMS

A Dissertation
for the Degree of Doctor of Philosophy (Ph.D.)
the Department of Mechanical Engineering
The University of Mississippi

by

MASOUD NAGHDI

August 2021

ABSTRACT

Breaking reciprocity in linear acoustic systems and designing a novel actuator for the nonreciprocal valveless pumps are studied in this dissertation. The first part was started by deriving the acoustic governing equations in a moving wave propagation medium. It was shown thatthe Coriolis acceleration term appears ina cross-product term with the wave vector. It means the main reason for breaking reciprocity in the circular fluid flow is the Coriolis acceleration term. Finally, the governing equations were solved numerically by COMSOL Multiphysics software. Moreover, Green`s second identity was used as a complimentary method to prove breaking reciprocityin such a system with moving medium. It is concluded that the non-reciprocity is magnified by increasing the angular velocity of the fluid system. The second part of this thesis is about achieving non-reciprocity utilizing the arrangement of a nozzle and diffuser as the inlet and outlet ports. This part's goal is to design a novel flexible actuator design for a valveless pump. The actuation mechanism which is novel in its own term, uses liquid metal called galinstan, a non-magnetic but electrically conducting alloy. In the designed device, an alternating current (AC) is applied onto a microchannel filled with galinstan. This device is placed between two permanent magnets with opposing poles. Due to the Lorentz force law, there will be radial in-plane forces on the polymeric flexible substrate. These in-plane forces radially contract and expand the circular diaphragm to provide an upward and downward out of plane bending moment, which causes an oscillatory reciprocating movement similar to a piezoelectric actuator`s movement. Compared to the traditional piezo electric materials such as Lead Zirconate Titanate (PZT), this actuator has numerous advantages such as being flexible, having the ability to be scaled down, being formed

as an integrated structure, and being fabricated by a considerably simple process. The prototype of the pump could be fabricated easily with Platinum Silicone rubber and some low-cost 3D printed elements. Although the prototype has been fabricated in a relatively large size, it is considered as a proper conceptual model representing the performance of the pump.

.

DEDICATION

This dissertation is dedicated to my dear parents, without whose tireless encouragement I would never complete my Ph.D.

LIST OF ABBREVIATIONS AND SYMBOLS

ρ	Density
u	The x-component of the velocity
P (or p)	Pressure
$\emptyset$	Velocity Potential function
$\delta(\vec{\boldsymbol{r}} - \vec{\boldsymbol{r}}_{\boldsymbol{0}})$	Kronecker Delta Function
$\hat{n}$	Unite normal vector
z	Acoustic Impedance
$\vec{\nabla}$	Gradient Vector
ω	Angular Velocity
u_1, u_2	The x and y components of the velocity field, respectively
$\hat{\boldsymbol{r}}$	Unit vector in the r-direction
$\breve{\omega}$	Frequency of the motivating acoustic sinusoidal wave
B	magnetic field
ν	Poisson Ratio
μ_0	Free Space Permeability
$\emptyset_o, \emptyset_i$	Volume Flow rate of input and output, respectively
η	Loss Pressure ratio in Nozzle/Diffuser
ψ	Stream Function
Re	Reynolds Number

S	Cross-sectional area
$\vec{\boldsymbol{u}}$	Velocity field
c	Velocity of sound
$\vec{\boldsymbol{u}}_F$	Fourier Transform of Velocity
G	Green Function
$G_F(\vec{\boldsymbol{r}}, \vec{\boldsymbol{r}}_\mathbf{0})$	Fourier Transform of Green Function
ΔG	Laplacian of the Green Function
TRM	Time Reversal Mirrors
$\vec{\boldsymbol{V}}$	Velocity Field resulted from the Angular Velocity
Ω	Frequency of the motivating acoustic sinusoidal wave
c_0	The speed of sound in the ambient temperature (constant)
E	Young Modulus
S	Durometer Hardness
μ	Dynamic Viscosity
J_v	Current Density
ζ_n & ζ_d	Pressure loss coefficient in nozzle and diffuser, respectively
j	Imaginary Number
ξ	Vorticity

ACKNOWLEDGMENTS

I would like to thank Dr Farhad Farzbod for his help and advices during my Ph.D program. I would also like to thank Christopher Sevigney and Parker Brewster for proofreading and editing the final report of this dissertation.

TABLE OF CONTENTS

ABSTRACT ii

DEDICATION iv

LIST OF ABBREVIATIONS AND SYMBOLS v

ACKNOWLEDGMENTS vii

TABLE OF CONTENTS viii

LIST OF TABLES ix

LIST OF FIGURES x

CHAPTER I ACOUSTICS BACKGROUND 1

CHAPTER II BREAKING RECIPROCITY IN ACOUSTICS 15

CHAPTER III NONRECIPROCITY SIMULATION IN COMSOL 24

CHAPTER IV LIQUID METAL AS AN ACTUATOR 35

CHAPTER V PERSITALTIC AND VALVELESS MICROPUMP 46

CHAPTER VI MICROPUMP WITH LIQUID METAL 67

REFERENCES 88

APPENDIX 96

VITA 105

LIST OF TABLES

1. The global parameters defined in the COMSOL (constant values). 25

2. First resonant frequency, calculated by model and measured experimentally. 44

3. The advantages and disdavantages of the actoutors. 60

4. The Reynolds number for all the critical cross-sectional areas 76

LIST OF FIGURES

1. Free body diagram for one-dimensional system 2
2. Volume of the System. 7
3. Source Points. 9
4. Boundary Conditions 10
5. The difference between the reflector and TRM performance 12
6. Concentration on the signal reflected by a target in a shallow water area 13
7. Time Reversal Symmetry 14
8. The process of breaking kidney stones using TRM 14
9. Acoustic Isolator and Circulator. 15
10. Full and Half Duplex Operation. 16
11. Sketch of an acoustic circulator. 20
12. Smooth Function versus Step Function. 26
13. The geometry of the circulator simulated in COMSOL. 29
14. Results of Deviation. 29
15. Propagation of one period sine wave. 30
16. The location of two source points. 31
17. Numerical results for the absolute value of velocity U 33
18. The setup of the helix actuator. 37
19. The sketch of actuator and setup 38
20. Displacement vs frequency for PFA 40

21. Displacement vs frequency for Polyurethane 41
22. Displacement vs frequency for PVC..... 42
23. Fundamental frequency of the tube..... 43
24. Schematic representation of NED actuators 50
25. The concept of an IPMC during a working period 51
26. Reciprocating plunger..... 55
27. Utilizing a plunger pushing a flexible membrane..... 56
28. The idea of a rotating membrane. 56
29. The model of single chamber diffuser/nozzle pump..... 62
30. The figures illustrating the pressure loss coefficient. 64
31. Bloodsucking system of mosquitos. 65
32. Model of double chamber system. 66
33. Geometry model of the source.. 71
34. The model of the pump. 74
35. Geometry of the model. 77
36. The four points on the center line. 78
37. One-nozzle/diffuser simulation results. 79
38. The model of the micropump in COMSOL. 80
39. The results for different velocities and frequencies. 81
40. All sections of the pump. 83
41. Simulation of the diaphragm deflection. 84

42. The top view of the experimental setup 86

CHAPTER I

ACOUSTICS BACKGROUND

Focusing on the theory of reciprocity is not the goal of this dissertation; the emphasis, instead, is on the application of breaking reciprocity in both acoustics and fluid flow. Breaking reciprocity, as it relates to electrical current transmission, has framed the concept of diodes and transistors fabrication: a concept that has had significant impact on electronic and logical circuits. Conversely,devices with a performance based on non-reciprocity will change the acoustic industry, especially in communicative systems. For instance, a nonreciprocal acoustic circulator can provide permanent and continuous sonar communication. This dissertation will first focus on mathematical analysis involving the second Green identity and numerical simulation using COMSOL Multiphysics software.

Breaking reciprocity has yet another application in fluid flow systems. Valveless micro-pumps utilizing a non-reciprocal arrangement of a nozzle and diffuser in the inlet and outlet ports have formed a new generation of micro devices. These devices can be embedded inside chip (LOC) systems. These systems need a uniform and flexible actuator to be consistent with the biological fluid systems. Additionally, miniaturizing actuator parts is necessary in LOC systems.

Finally, this dissertation focuses on the novel design of an actuator that is both flexible and scalable. The actuator consists of a polymeric substrate that has a narrow micro-channel filled with galinstan carrying an alternating current. Following the Lorents force law, the liquid metal applies in-plane forces. These in-plane forces provide the alternating pressure in the chamber that is required for the net pumping effect. The designed actuator can be fabricated in minuscule sizes and easily integrated with other parts of an LOC system. Flexural modulus and the density of the

pump both depend on the utilized polymeric substrates and the geometry of the microchannel networks. The designed actuator is based on a bio-inspired double chamber suction system: a system observed in blood-sucking insects such as butterflies, bugs, and mosquitos. The new actuator can potentially be used in the microfluidic industries because of its simple performance, low-cost fabrication process, and uniformly flexible characteristics.

1. Governing equations in a non-moving medium

The conservation of mass and momentum are the two fundamental equations required to derive the wave equation. We begin by deriving the fundamental formulas since they lead us to

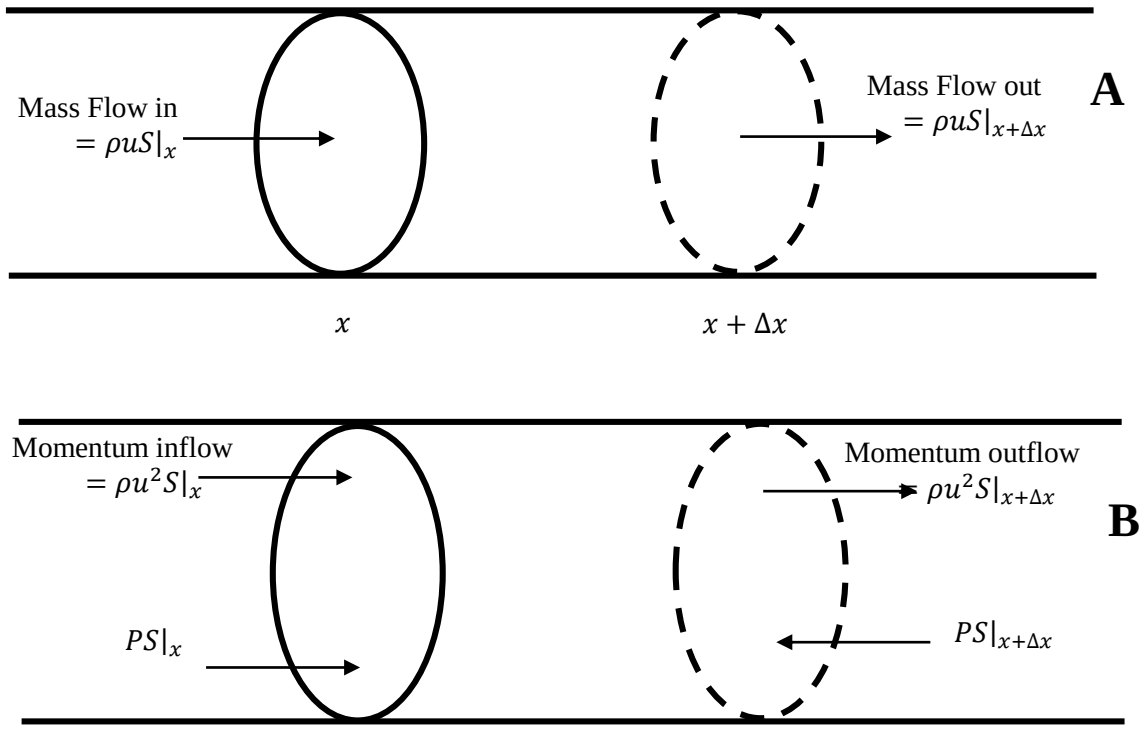

Figure 1 Free body diagram for one-dimensional system A) Conservation of mass B) Conservation of momentum [1]

the wave equation in which we have nonreciprocal terms. Figure 1 shows the free body diagram of a one-dimensional system. The resulting formulas for this system can then be expanded to a

three-dimensional system.

The conservation of mass equation is [1]:

$$\rho uS|_x - \rho uS|_{x+\Delta x} = \frac{\partial}{\partial t}(\rho \Delta x S) \quad \text{Eq. (1)}$$

And for conservation of momentum:

$$\rho u^2 S|_x - \rho u^2 S|_{x+\Delta x} + PS|_x - PS|_{x+\Delta x} = \frac{\partial}{\partial t}(\rho u \Delta x S), \quad \text{Eq. (2)}$$

where P is pressure, S is the cross-sectional area, ρ is density, and u is a physical property associated with the disturbance or signal. In the limit as Δx→0, the equations have the final forms [1]:

$$\rho_t + (\rho u)_x = 0 \; or \; \rho_t + u\rho_x + \rho u_x = 0 \quad \text{Eq. (3a)}$$

$$\frac{D\rho}{Dt} + \rho u_x = 0 \quad \text{Eq. (3b)}$$

$$(\rho u)_t + (\rho u^2)_x + P_x = 0 \quad \text{Eq. (4a)}$$

$$\rho \frac{Du}{Dt} + P_x = 0, \quad \text{Eq. (4b)}$$

where D/Dt is the total or material derivative, and the subscripts denote partial derivatives. Equations 3 and 4 are the general forms of conservation of mass and momentum respectively, where the longitudinal force due to viscosity has not been included in the free body diagram. In otherwords, the losses in the wave propagation were considered to be negligible. Three-dimensional formulas can be derived based on similar formulation in the y and z directions [1].

$$\rho_t + \nabla.(\rho \vec{\boldsymbol{u}}) = 0 \quad \text{Eq. (5)}$$

$$\rho[\vec{\boldsymbol{u}}_t + (\vec{\boldsymbol{u}}.\nabla)\vec{\boldsymbol{u}}] + \nabla P = 0, \quad \text{Eq. (6)}$$

where $\vec{\boldsymbol{u}} = u_x\vec{\boldsymbol{i}} + u_y\vec{\boldsymbol{j}} + u_z\vec{\boldsymbol{k}}$.

2. Equation of state

Equation of state represents a relationship between two thermodynamic variables, which must be considered with the conservation of momentum equation. The equation of state relevant to acoustics represents the relationship between pressure, entropy and density. It is stated as P=P(ρ,s); where s is entropy, ρ is density and P is pressure. The quiet fluid is homogeneous; consequently, $\nabla(\rho_0) = 0 \ \ and \ \nabla(p_0) = 0$. It is safe to assume that in low energy acoustics, the viscosity effects can be taken as negligible. Thus, in the final governing equations, the entropy remains constant; i.e., the process is isentropic. When the pressure is just the function of density, it can be stated as the Taylor series [1]:

$$P = p_0 + A\left(\frac{\rho - \rho_0}{\rho_0}\right) + \frac{B}{2!}\left(\frac{\rho - \rho_0}{\rho_0}\right)^2 + \frac{C}{3!}\left(\frac{\rho - \rho_0}{\rho_0}\right)^3 + \cdots, \qquad \text{Eq. (7)}$$

where the zero subscript denotes the equilibrium state, or when the system is quiet. The coefficients A, B, C, … are determined from experiments. The sound speed c, is defined by:

$$c^2 \equiv \left.\frac{\partial P}{\partial \rho}\right|_{s=const.} = \frac{dP}{d\rho} \ (isentropic \ process) \qquad \text{Eq. (8)}$$

Taking a derivative from equation 7, the sound speed can be formulated as:

$$c^2 = \frac{A}{\rho_0} + \frac{B}{\rho_0}\left(\frac{\rho - \rho_0}{\rho_0}\right) + \frac{C}{2!\,\rho_0}\left(\frac{\rho - \rho_0}{\rho_0}\right)^2 + \cdots \qquad \text{Eq. (9)}$$

For better simplification, we can separate the static component of pressure and density, which means:

$$p \equiv P - p_0 \quad \& \quad \delta\rho \equiv \rho - \rho_0 \qquad \text{Eq. (10)}$$

Therefore, the isentropic equation of state becomes [1]:

$$p = c_0^2 \delta\rho \left[1 + \frac{B}{2!\,A}\frac{\delta\rho}{\rho_0} + \frac{C}{3!\,\rho_0}\left(\frac{\delta\rho}{\rho_0}\right)^2 + \cdots\right] \qquad \text{Eq. (11)}$$

Governing equations 5 and 6, as well as equation of state 11, have some nonlinear components. When the energy of the acoustice wave under consideration does not cause the state of the medium to deviate substantially from the equilibrium state, we can assume that the linear approximation represents the system with sufficient accuracy. Therefore, the next step is to derive the proper linearized forms. When the disturbance of sound waves is considerably small compared to the equilibrium state of the system, we can assume that the excess pressure p, excess density δρ, and particle velocity u can be considered as small first-ordered quantities. Thus, these approximations are mathematically stated as:

$$|\delta\rho| \ll \rho_0 \quad \Rightarrow \quad |p| \ll \rho_0 c_0^2 \quad \& \quad |u| \ll c_0 \qquad \text{Eq. (12)}$$

Considering the inequalities in equation 12, the governing equations 5 and 6 can be modified as:

$$\delta\rho_t + \rho_0 \nabla . \vec{\boldsymbol{u}} = 0 \quad \& \quad \rho_0 \vec{\boldsymbol{u}}_t + \nabla \mathrm{p} = 0 \qquad \text{Eq. (13)}$$

And the equation of state is stated as:

$$p = c_0^2 \delta\rho \qquad \text{Eq. (14)}$$

Because the medium is initially at rest, it is possible to use the velocity potential function:

$$\vec{\boldsymbol{u}} = \nabla\emptyset \quad \& \quad p = -\rho_0 \emptyset_t \qquad \text{Eq. (15)}$$

We can then combine the equations 13, 14, and 15 into one equation:

$$\nabla^2\emptyset - \frac{1}{c_0^2}\emptyset_{tt} = 0 \qquad \text{Eq. (16)}$$

Equation 16 can be derived with respect to particle velocity $\vec{\boldsymbol{u}}$ [1]:

$$\nabla^2\vec{\boldsymbol{u}} - \frac{1}{c_0^2}\vec{\boldsymbol{u}}_{tt} = 0 \qquad \text{Eq. (17)}$$

3. Helmholtz equation

We now use the Fourier transform and apply it to equation 17 to turn it into the Helmholtz equation. The Fourier transform properties that we use in our derivation are [13]:

$$\vec{\boldsymbol{u}}_F(\vec{\boldsymbol{r}},\vec{\boldsymbol{\omega}}) = \frac{1}{2\pi}\int_{-\infty}^{+\infty}\vec{\boldsymbol{u}}\,(\vec{\boldsymbol{r}},t)e^{j\omega t}dt \quad \& \quad \mathcal{F}\left(\frac{\partial^n}{\partial t^n}\vec{\boldsymbol{u}}(\vec{\boldsymbol{r}},t)\right) = (j\omega)^n\mathcal{F}\big(\vec{\boldsymbol{u}}(\vec{\boldsymbol{r}},t)\big), \qquad \text{Eq. (18)}$$

where $\vec{\boldsymbol{u}}_F$ is the Fourier transform of $\vec{\boldsymbol{u}}$. Because the Fourier operator $\mathcal{F}$ is linear, the Fourier transform of equation 16 is:

$$(\nabla^2 + k^2)\vec{\boldsymbol{u}}_F = 0, \qquad \text{Eq. (19)}$$

where $k^2 = \frac{\omega^2}{c_0^2}$, which means equation 19 gives us the potential velocity in frequency domain.Converted back to the time domain by the inverse Fourier transform, we get:

$$\vec{\boldsymbol{u}}(\vec{\boldsymbol{r}},\boldsymbol{t}) = \int_{-\infty}^{+\infty}\vec{\boldsymbol{u}}_F\,(\vec{\boldsymbol{r}},\omega)e^{-j\omega t}d\omega \qquad \text{Eq. (20)}$$

4. Dirichlet problem with point source

We are interested in focusing on the simplest problem: the medium is at rest except in one (or more) source points, and the system is homogeneous. The Kronecker delta function is helpful to describe the point source.

$$\delta(\vec{\boldsymbol{r}} - \vec{\boldsymbol{r}}_{\boldsymbol{0}}) = \begin{cases} 1 & \vec{\boldsymbol{r}} = \vec{\boldsymbol{r}}_{\boldsymbol{0}} \in D \\ 0 & \vec{\boldsymbol{r}} \neq \vec{\boldsymbol{r}}_{\boldsymbol{0}} \in D \end{cases}, \quad \text{Eq. (21)}$$

where D is the volume of the system shown in figure 2. The singular source point is excluded; therefore, the Helmholtz equation can be rewritten as the following form [13]:

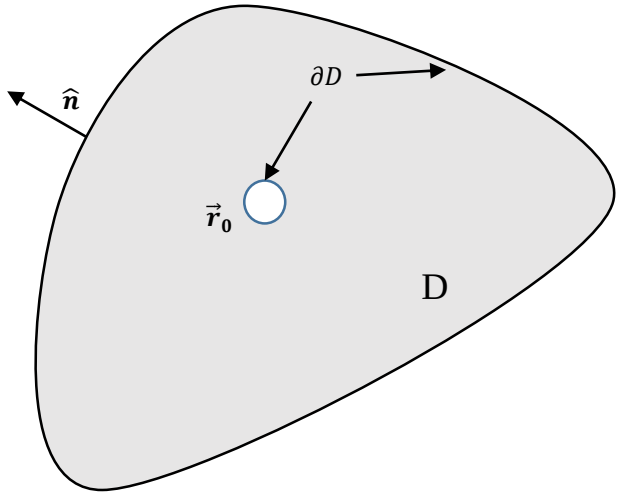

Figure 2. Volume of the System. The volume D, the boundary ∂D, and the point source located at $\vec{\boldsymbol{r}}_{\boldsymbol{0}}$. An infinitesimally circle around the point source exclude the singular source from the volume D.

$$(\nabla^2 + k^2)\vec{\boldsymbol{u}}_F = V_F \delta(\vec{\boldsymbol{r}} - \vec{\boldsymbol{r}}_{\boldsymbol{0}}), \quad \text{Eq. (22)}$$

where V_F is the Fourier transform of point source intensity. The Green function is defined as the solution of the following equation:

$$(\nabla^2 + k^2)G_F(\vec{\boldsymbol{r}}, \vec{\boldsymbol{r}}_{\boldsymbol{0}}) = \delta(\vec{\boldsymbol{r}} - \vec{\boldsymbol{r}}_{\boldsymbol{0}}), \quad \text{Eq. (23)}$$

where the G_F is the Fourier transform of Green`s function G. The potential velocity is calculated by the following integral form:

$$\vec{\boldsymbol{u}}_F(\vec{\boldsymbol{r}}, \omega) = \int V_F \, G_F(\vec{\boldsymbol{r}}, \vec{\boldsymbol{r}}')d\vec{\boldsymbol{r}}' \quad \text{Eq. (24)}$$

The Green function $G_F(\vec{\boldsymbol{r}}, \vec{\boldsymbol{r}}_{\boldsymbol{0}})$ has to satisfy the following conditions [13]:

1. It should be harmonic in D (ΔG=0) and possess the continuous second partial derivatives in the entire D except at $\vec{\boldsymbol{r}} = \vec{\boldsymbol{r}}_{\boldsymbol{0}}$
2. $G_F(\vec{\boldsymbol{r}}, \vec{\boldsymbol{r}}_{\boldsymbol{0}}) = 0$ at boundaries (∂D)
3. The function $G_F(\vec{\boldsymbol{r}}, \vec{\boldsymbol{r}}_{\boldsymbol{0}}) + \frac{1}{4\pi|\vec{\boldsymbol{r}} - \vec{\boldsymbol{r}}_{\boldsymbol{0}}|}$ is defined at the source point $\vec{\boldsymbol{r}} = \vec{\boldsymbol{r}}_{\boldsymbol{0}}$; in addition, it is harmonic and has a continuous second derivative in the entire D (including the point source)

The source point value can be calculated by the following formula [13]:

$$\vec{\boldsymbol{u}}_F(\vec{\boldsymbol{r}}_{\boldsymbol{0}}, \omega) = \oiint_{\partial D} \vec{\boldsymbol{u}}_F(\vec{\boldsymbol{r}}, \vec{\boldsymbol{r}}_{\boldsymbol{0}}) \frac{\partial G_F(\vec{\boldsymbol{r}}, \vec{\boldsymbol{r}}_{\boldsymbol{0}})}{\partial n} dS \qquad \text{Eq. (25)}$$

Equation 25 can be expanded for a system with other boundary conditions too [13]:

$$\vec{\boldsymbol{u}}_F(\vec{\boldsymbol{r}}_{\boldsymbol{0}}, \omega) = \oiint_{\partial D} h(\vec{\boldsymbol{r}}) \frac{\partial G_F(\vec{\boldsymbol{r}}, \vec{\boldsymbol{r}}_{\boldsymbol{0}})}{\partial n} dS \iiint_D f(\vec{\boldsymbol{r}})\, G_F(\vec{\boldsymbol{r}}, \vec{\boldsymbol{r}}_{\boldsymbol{0}}) d\vec{\boldsymbol{r}} \qquad \text{Eq. (26a)}$$

$$\Delta \vec{\boldsymbol{u}}_F = f(\vec{\boldsymbol{r}})\ in\ D \qquad \& \qquad \vec{\boldsymbol{u}}_F = h(\vec{\boldsymbol{r}})\ in\ \partial D \qquad \text{Eq. (26b)}$$

5. principle of reciprocity concluded from the Green`s function

Helmholtz [14] first discussed reciprocity in acoustics during an analysis of open-ended pipes. Later Strutt (Lord Rayleigh) [15] generalized this theorem for any linear system, including those with energy dissipation. Lyamshev [16] presented this theory in a general case of anisotropic media. In order to have reciprocity in an acoustic medium, it is not necessary to preserve energy, i.e., a linear system can have damping in any form while satisfying the reciprocity condition [17, 18]. However, the medium should be at rest for the theorem to hold true [19, 20]. One way to break reciprocity is to have a moving medium in the system. Fleury et al. [7, 21, 22] recently used this effect to devise an acoustic circulator and a conceptual resonator lattice structure [23, 24].

In order to prove that an acoustic system is reciprocal, utilizing Green`s function is helpful. Green`s function is symmetric, which is one of the most important characteristics. It states that if

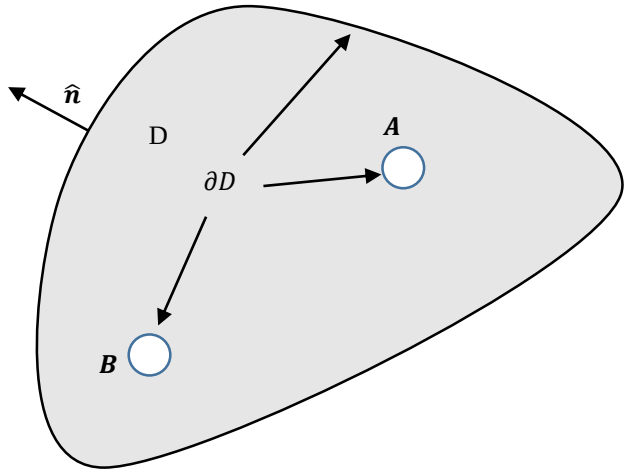

Figure 3. Source Points. The volume D, the boundary ∂D, and the point sources A & B which is arbitrarily located inside the volume D. An infinitesimally circle around the point sources exclude the singular sources from the volume D.

there are two source points at A and B, according to figure 3, the symmetricity of the Green`s function shows that $G(\boldsymbol{a}, \boldsymbol{b}) = G(\boldsymbol{b}, \boldsymbol{a})$. This equality states the principle of reciprocity. It means that the effect on point B due to a source at point A is interchangeable with the effect on point A due to the same source at point B. Though, mathematically, the principle of reciprocity is proved in a non-moving system, the physical concept of reciprocity requires further explanation.

$$G(\vec{\boldsymbol{r}}, \vec{\boldsymbol{r}}_{\boldsymbol{0}}) = G(\vec{\boldsymbol{r}}_{\boldsymbol{0}}, \vec{\boldsymbol{r}}) \quad for\ \vec{\boldsymbol{r}} \neq \vec{\boldsymbol{r}}_{\boldsymbol{0}} \qquad \text{Eq. (27)}$$

Suppose there is a non-moving heterogeneous medium, shown in figure 4. There are two arbitrary points called A and B inside the system. When a transmitter is placed at point A, a receiver at point B detects the sound wave. The second step uses the same test, but with the transmitter and receiver locations reversed. The principle of reciprocity states that the waves detected by the receiver should be the same for both of the transmitter/receiver configurations. One common example of this acoustic phenomenon is seen in those instances where we hear the voice of a neighbor outside of our room. The neighbor will likely hear our voice in the same way. The

principle of reciprocity is true for other boundary conditions as well.

Consider two single frequency sources in a general space such as the one depicted in Figure 4. We cut out an infinitesimally small volume around the two sources. By changing which source is active and inactive successively, we get two acoustic fields, named A and B. By assuming the medium to be at rest, we can conclude that the velocity field is irrotational. Thus we can express $\vec{\boldsymbol{u}} = u_1\vec{\boldsymbol{i}} + u_2\vec{\boldsymbol{j}}$ as the gradient of a scalar, i.e. velocity potential; $\vec{\boldsymbol{u}} = \nabla\emptyset$. Using Green's second identity for two fields A and B, we have [25]:

$$\int_V (\Phi_A \nabla^2\Phi_B - \Phi_B\nabla^2\Phi_A) = \oint_{\partial V} (\Phi_A\nabla\Phi_B - \Phi_B\nabla\Phi_A)\hat{\boldsymbol{n}}, \qquad \text{Eq.(28)}$$

in which V is the volume of interest and ∂V is the surface boundary of the volume. Velocity potential fields are due to two different sources with the same frequency, so for both potentials we have:

$$\nabla^2\Phi_A + k\Phi_A = 0, \qquad \nabla^2\Phi_A + k\Phi_A = 0, \qquad \text{Eq.(29)}$$

$$P_A = -j\omega\Phi_A, \qquad P_B = -j\omega\Phi_B, \qquad \text{Eq.(30)}$$

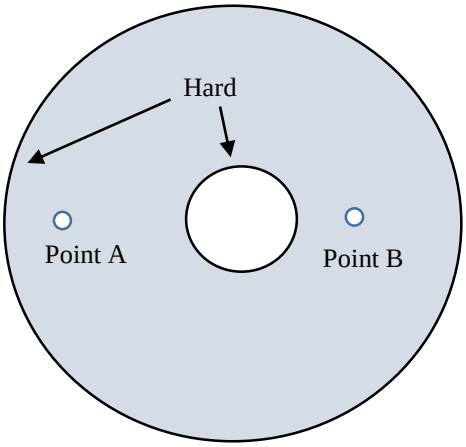

Figure 4. Boundary Conditions The system with two points A and B to examine the reciprocity of the acoustic field. When one point is a source, another one is a measurement point.

in which $k = \omega^2/c^2$. Eq. (29) makes the left hand side of eq. (28) vanish. Then by using $\vec{\boldsymbol{u}} = \nabla\emptyset$ and Eq. (30), we have:

$$\oint_{\partial V} (\mathrm{P}_A \mathbf{u}_B \cdot \hat{\boldsymbol{n}} - \mathrm{P}_B \mathbf{u}_A \cdot \hat{\boldsymbol{n}}) = 0. \qquad \text{Eq.(31)}$$

This integral vanishes on areas of the surface ∂V where we have a perfectly rigid boundary (that is to say: $\vec{\boldsymbol{u}}.\hat{n} = 0$), pressure release boundary (i.e. P = 0) or a boundary in which the pressure is impedance times normal velocity ($P = z\vec{\boldsymbol{u}}.\hat{n}$). In addition, if the boundary is far from the sources and we have some absorption in the system, then since the area increases as r^2 and intensity $P\vec{\boldsymbol{u}}$ decreases, the integral approaches zero. In these situations, what is left is the infinitesimal surface areas around the sources. This now becomes a reciprocity relation.

6 Time reversal symmetry

Time reversal symmetry is a concept that is similar to reciprocity, but has some nuanced differences. Since these two concepts are sometimes erroneously used interchangeably, we will be discussing time reversal symmetry as well. Suppose that the governing equation of an acoustic field $p(\vec{\boldsymbol{r}}, t)$ is determined by the following equations [26]:

$$(L_r + L_t)p(\vec{\boldsymbol{r}}, t) = 0 \qquad \text{Eq. (32a)}$$

$$L_r = \vec{\nabla}.\left(\frac{1}{\rho(\vec{\boldsymbol{r}})}\vec{\nabla}\right) \;\; \& \;\; L_t = -k(\vec{\boldsymbol{r}})\partial_{tt} \qquad \text{Eq. (32b)}$$

Where ρ is density, k is compressibility, and $\vec{\boldsymbol{r}}$ is displacement vector. The equation 32b is time reversal invariant because the order of derivatives with respect to time is two. Therefore, it means that if $p(\vec{\boldsymbol{r}}, t)\ t: t_1 \to t_2$ is the function, which satisfies the governing equation 32a, then $p(\vec{\boldsymbol{r}}, \acute{t} = -t)\ \acute{t}: -t_2 \to -t_1$ is also a solution. It is obvious that the order of time derivatives is

important; for instance, a viscous damping or friction can violate the time reversal reciprocity because it appears as a first order time derivative term in the final governing equation.

Time reversal mirrors (TRM) are used in applications which utilize the concept of time reversal symmetry. Figure 5 explains the difference between the performances of TRM and a normal acoustic reflector. For instance, when a source says “HELLO,” the letters go in a time

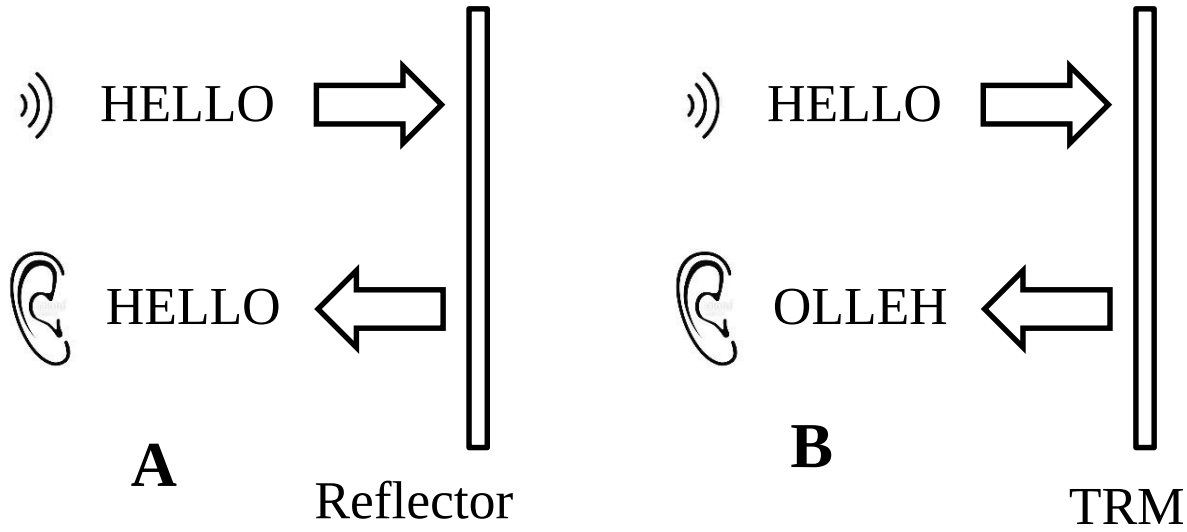

Figure 5. The difference between the reflector and TRM performance A) a reflected wave is heard as same as the incident wave B) the returned back wave by TRM is heard different compared to the incident wave

sequence. It means the letter “H” is heard at time t_1 and the last letter “O” at time t_5, where the time sequence is ($t_1 < t_2 < t_3 < t_4 < t_5$) [9].

Therefore, the reflector returns all of the letters in the same sequence. Thus, the receiver can hear the real word “HELLO” when it reflects by any reflector. However, TRM changes the sequence because the negative time sequence means ($-t_5 < -t_4 < -t_3 < -t_2 < -t_1$); consequently, the receiver hears a different word “OLLEH” returned by TRM. This concept is used in applicatios such as: the destruction of tumors, the targeting of kidney stones, the detection of defects in metals, and the detection of mines in the ocean. One of the common uses of TRM is underwater communication in shallow water (depth<120 m); the concept of the system is described in figure

6. The transponder arrays on each side are located in such a way to cancel out the reflection of a sound beam from the water`s surface and the seabed. Thus, monitoring the exact location of any target is possible using TRM arrays over 30 km.

Utilizing TRM in order to target kidney stones is another application described in figure 7. The receiver detects the distorted echo reflected by the stone, and the time-reversed pulse of the echo breaks down the stone inside the tissue without needing surgery. It should be noted that time

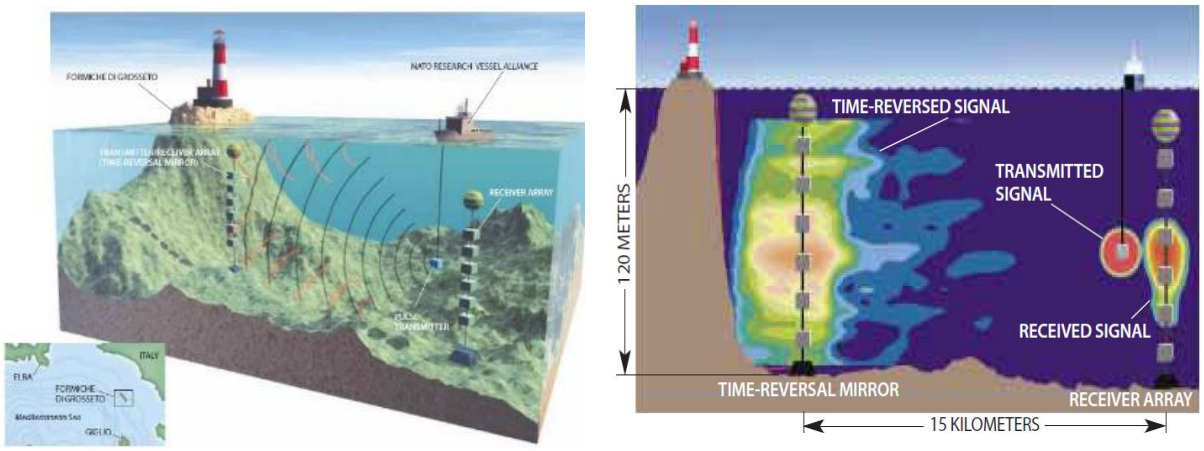

Figure 6. Concentration on the signal reflected by a target in a shallow water area A) The incident wave is received with some refracted noises from water surface and seabed (red color) B) TRM arrangement on the right side cancels the noises and precisely determine the target location (red color) [9]

reversal symmetry is different from reversing the time, i.e., going back in time [27]. For example, in a system with viscous damping, if we march back in time, the energy is going back to the system, and entropy decreases. This concept of marching back in time, or active time reversal, can be utilized to focus acoustic energy in a very small area [26, 28]. Figure 8 shows this difference between TRM and reversing back in time.

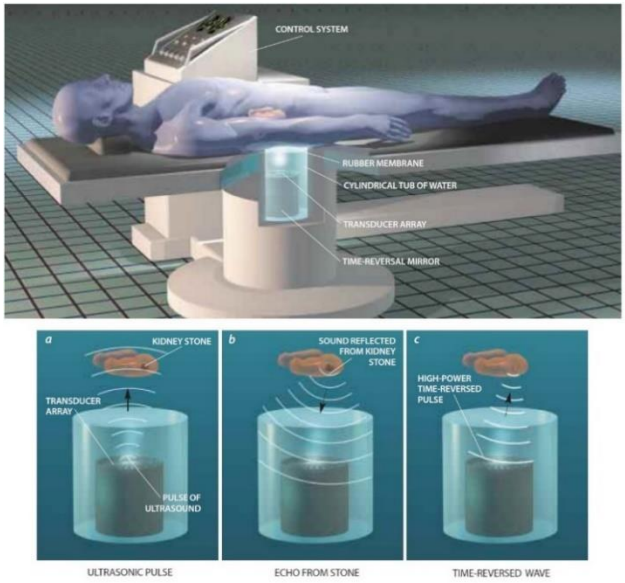

Figure 8. The process of breaking kidney stones using TRM a) An incident ultrasonic pulse wave is propagated to locate the target (kidney stones). b) The reflected ultrasonic wave returns back to the TRM arrays. c) TRM sends the time-reversed wave to concentrate on the kidney stone without any effects on the other organs or tissues [9].

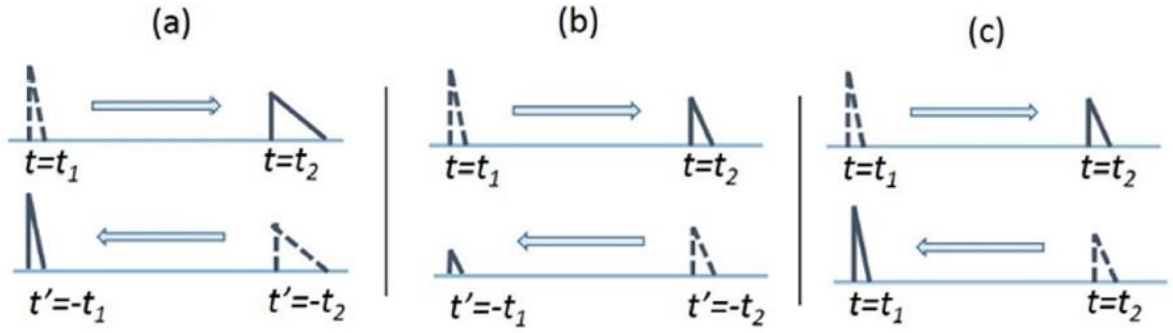

Figure 7. Time Reversal Symmetry (a) In a system with time reversal symmetry u(t,x) and u(t'=- t,x) are both solutions. Note that the direction of time is positive in both cases. (b) Wave propagation in a system without time reversal symmetry has asymmetrical wave propagation when we go forward in time; $-t_2$ to $-t_1$ and t_1 to t_2. (c) Wave propagation in a system without time reversal symmetry; in this case, we go forward and backward in time.

CHAPTER II

BREAKING RECIPROCITY IN ACOUSTICS

Nonreciprocity has numerous applications in electromagnetic wave elements such as isolators and circulators in microwaves or photonic industries [7] (figure 9). When an external magnetic bias **B** is applied, the elements react as nonreciprocal devices. The concept of nonreciprocity can be explained in two elements depicted in figure 9. The isolator depicted in figure 9A is made up of two interconnected parts, through which the signal transmission passes in only one direction (right to left). Three isolators can be symmetrically embedded in a circular pattern to construct a right-handed circulator (figure 9b). The circulator can shift the transmitted signal of one port to every other port in a right-hand fashion.

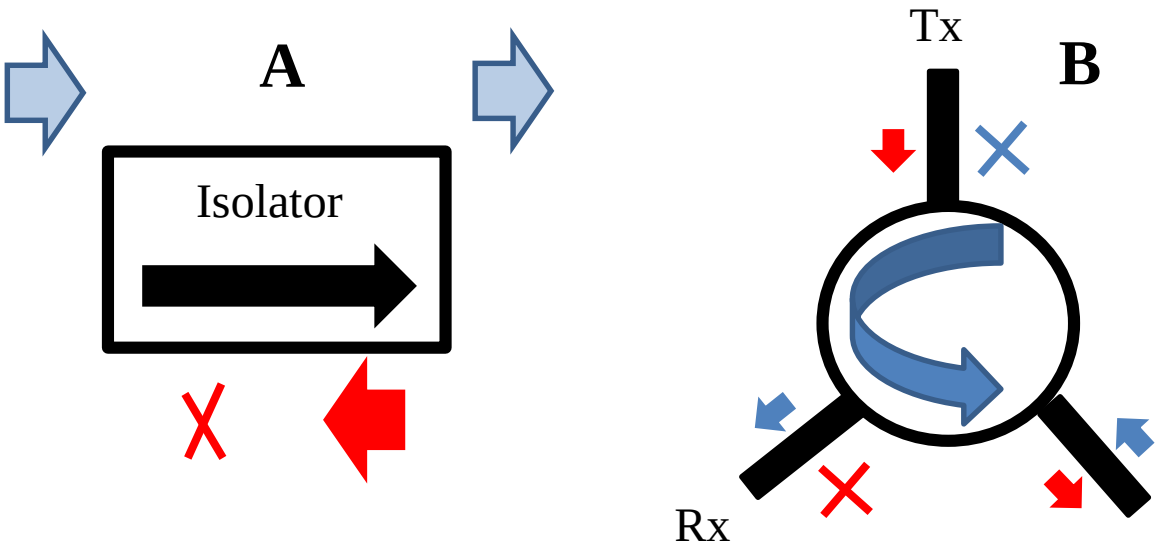

Figure 9 Acoustic Isolator and Circulator. A) an isolator allows the flow rate just in one direction. B) a symmetrical configuration of isolators can be used as a circulator. A circulator can continuously transmit and receive data without any interruption [7].

Full duplex mode of communication is vital in radiocommunication systems. Because it allows having continuous communication with a single antenna on a single frequency channel (figure 10a). It is also possible to have continuous communication with two antennas if the

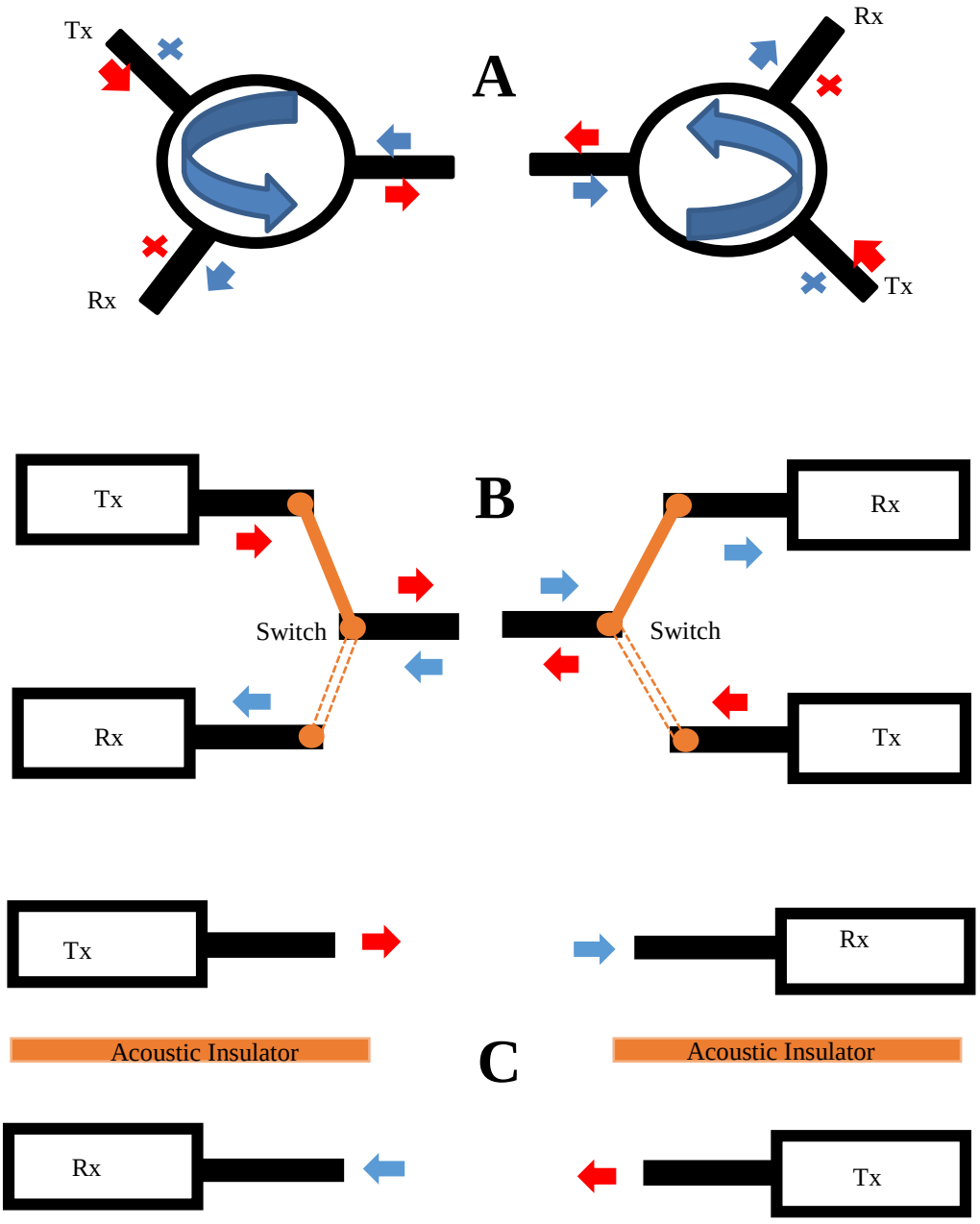

Figure 10 Full and Half Duplex Operation.. A) Sketch of a full duplex operation with one sensor B) Full duplex using two isolated sensors C) a half-duplex operation using two sensors [7]

transducers are completely isolated (figure 10b). Another configuration is the half-duplex operation, which is highly applicable to sonar systems; however, it is impossible to have mutual communication simultaneously (figure 10c). Therefore, it limits the pulse duration, output power, sampling rate, signal-to-noise ratio, and consequently, the communication speed. Although it is possible to use two different frequency channels for transmission and reception, this is not suitable due to the unnecessary use of the working spectrum. For that reason, it would be beneficial to use the proper acoustic components for this purpose, such as acoustic isolators or acoustic circulators. In the next section, we explain an effective way to break reciprocity in acoustic systems.

1. The clues to break reciprocity in acoustics

External magnetic fields have significant roles in both nonreciprocal systems and systems without time reversal symmetry. Nonreciprocal phase shift affected by magnetic field for light is a phenomenon observed in optics [29]. This effect is equivalent to the Aharonov and Bohm effect in which the potential field $\vec{\boldsymbol{A}}$ affects phase φ based on the following equation:

$$\emptyset = \frac{e}{h}\int_{r}^{\acute{r}} \vec{\boldsymbol{A}}.\, d\acute{r} \qquad where\ \vec{\boldsymbol{B}} = \nabla \times \vec{\boldsymbol{A}}, \qquad \text{Eq. (33)}$$

where e is the unit charge, h is the Planck` coefficient, and $\vec{\boldsymbol{B}}$ is the magnetic field. Equation 33 shows the effect of the magnetic field $\vec{\boldsymbol{B}}$ appearing as a cross-product term based on Maxwell`s equations.

Interaction between a magnetic field and a beam of quantum particles (such as electrons) posed by Aharonov and Bohm [30] initiated a significant research campaign due to its paradoxical effect. A magnetic field isolated inside an infinite cylinder with a direction parallel to the axis can scatter quantum particles striking outside of the cylinder without directly “touching” the magnetic

field. This phenomenon happens because the magnetic vector potential in Schrodinger's equation depends on the magnetic flux, which itself depends on the magnetic field passing through the cylinder due to the Stokes relation. Berry et al. [31] studied the Aharonov–Bohm effect both theoretically and experimentally. In order to qualify the interaction between unobservable topology and wavefront experimentally, they use a resembling phenomena of surface wave interaction with irrotational vortex. The resemblance between these two phenomena stops at both being unobservable topology. In the surface wave case, the wave front and the irrotational vortex are directly "accessing" each other by one passing through the other. This type of interaction between surface wave and vortices was further examined by Coste et al. [32] for surface waves in shallow water and by Bernal et al. [33] for vorticity fields with zero net circulation. Roux et al. used acoustic time-reversal mirrors to enhance the Aharonov–Bohm effect [34, 35]. Other research has been performed in the area of vortex interaction with acoustic waves in order to better probe its applications in jet noise analysis and solid-fluid interactions. These include other types of vortices such as turbulent vortex [36] ring, [37] Rankine vortex, [38] and vortex dipole [39].

2. Breaking reciprocity in the linear and nonlinear acoustic systems

According to section 1.2.2, an external magnetic field is more often than not the source of breaking reciprocity in electromagnetic systems. Moreover, because the magnetic field appeared as a cross-product term in the final equation, the same idea could be used to have a cross-product term in the final governing acoustic equations. Coriolis acceleration appears as a cross-product term when an object moves with a frame of reference, which rotates over an internal fixed frame. Therefore, reciprocity may be broken because a medium with a rotating velocity field appears as a cross-product term in the final governing wave equations. This method is analogous to the

methodology used by Roux et al. [34, 35].

Breaking reciprocity can also be achieved in nonlinear systems. There are more ways to achieve the same goal of making an acoustic and/or thermal diode in nonlinear systems [40]. This can be done by using nonlinear granular media, [41] combining sonic crystal and nonlinear medium, [42] nonlinear lattices coupled together by a harmonic spring, [43] through bifurcations, [44] and combining a linear and nonlinear system [45, 46]. Apart from these techniques, there are some methods to make a device with interesting acoustic properties. For instance, Zhu et al. [47] designed a tunnel with meta-surfaces in which a plane wave travels through and exits as a non-plane wave while the plane wave does not go through as much if it enters the tunnel from the other side. As Maznev et al. [48] explained, these are not, in fact, "diodes" nor do they break reciprocity; however, they do certainly have interesting applications.

3. Wave equations in a rotating medium

In this section, we derive the governing wave equation for a typical acoustic circulator shown in figure 11. As is shown in the figure, the medium velocity field has an ascending linear function with respect to the distance from the center. This means the velocity field can simply be described using the following formula:

$$\vec{\boldsymbol{V}} = r\omega\vec{\boldsymbol{\theta}}\,, \qquad \text{Eq. (34)}$$

where ω is the angular velocity of the rotating medium (assumed to be constant), r is the distance measured from the center, and $\vec{\boldsymbol{\theta}}$ is the tangential unit vector. Thus, the velocity field does not have any component in the r direction because only the tangential component is needed for the Coriolis acceleration formula [49]. This tangential component is necessary to deviate the wave propagation in a circulator (figure 11). An additional system requirement is that the solid fins of the circulator

have the same acoustic impedance as the fluid medium (water) to avoid any interference with the acoustic field.

We can find the general formula when the medium has a velocity field $\vec{\boldsymbol{V}}$. Thus, the additional velocity can be added up to the general equations 5 and 6:

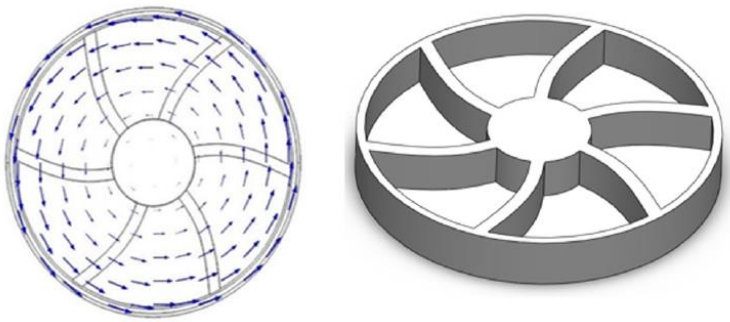

Figure 11 Sketch of an acoustic circulator. The blue arrows represent the velocity field of the medium $\vec{\boldsymbol{V}} = r\omega\vec{\boldsymbol{\theta}}$

$$\rho_t + \nabla.(\rho(\vec{\boldsymbol{u}} + \vec{\boldsymbol{V}})) = 0 \qquad \text{Eq. (35)}$$

$$\rho[(\vec{\boldsymbol{u}} + \vec{\boldsymbol{V}})_t + (\vec{\boldsymbol{u}} + \vec{\boldsymbol{V}}).\nabla(\vec{\boldsymbol{u}} + \vec{\boldsymbol{V}})] + \nabla P = 0 \qquad \text{Eq. (36)}$$

Considering the assumptions needed for linearization (section 1.1.3), the linearized forms of equations 34 and 35 are:

$$\left(\frac{\partial}{\partial t} + \vec{\boldsymbol{V}}.\nabla\right)\delta\rho + \delta\rho(\nabla.\vec{\mathbf{V}}) + \rho_0\nabla.(\vec{\boldsymbol{u}} + \vec{\boldsymbol{V}}) = 0 \qquad \text{Eq. (37)}$$

$$\rho_0(\vec{\boldsymbol{u}} + \vec{\boldsymbol{V}})_t + \rho_0(\vec{\boldsymbol{V}}.\nabla)\vec{\boldsymbol{u}} + \rho_0(\vec{\boldsymbol{V}}.\nabla)\vec{\boldsymbol{V}} + \rho_0(\vec{\boldsymbol{u}}.\nabla)\vec{\boldsymbol{V}} + \nabla p = 0 \qquad \text{Eq. (38)}$$

In order to check the resulting equations, if the velocity field is constant ($\vec{\mathbf{V}} = \vec{\mathbf{V}}_0$), and with consideration of the equation of state, we have:

$$\left(\frac{\partial}{\partial t} + \vec{\mathbf{V}}_0.\nabla\right)p + \rho_0 c_0^2\nabla.(\vec{\boldsymbol{u}}) = 0 \qquad \text{Eq. (39)}$$

$$\rho_0[\vec{\boldsymbol{u}}_t + (\vec{\mathbf{V}}_0.\nabla)\vec{\boldsymbol{u}}] + \nabla p = 0 \qquad \text{Eq. (40)}$$

The equations 39 and 40 are the same as the equations obtained by Pierce [18]. Plugging equation

34 into equations 39 and 40 and converting the polar coordinate to the Cartesian system, we have:

$$\frac{\partial}{\partial t}\begin{bmatrix}u_1\\u_2\\p\end{bmatrix}+\begin{pmatrix}-\omega y & 0 & 1/\rho_0\\0 & -\omega y & 0\\\rho_0 c_0^2 & 0 & -\omega y\end{pmatrix}\frac{\partial}{\partial x}\begin{bmatrix}u_1\\u_2\\p\end{bmatrix}+\begin{pmatrix}\omega x & 0 & 0\\0 & \omega x & 1/\rho_0\\0 & \rho_0 c_0^2 & \omega x\end{pmatrix}\frac{\partial}{\partial y}\begin{bmatrix}u_1\\u_2\\p\end{bmatrix}$$
$$+\begin{pmatrix}0 & -\omega & 0\\\omega & 0 & 0\\0 & 0 & 0\end{pmatrix}\begin{bmatrix}u_1\\u_2\\p\end{bmatrix}+\begin{bmatrix}-\omega^2 x\\-\omega^2 y\\0\end{bmatrix}=0, \qquad \text{Eq. (41)}$$

where ω is the angular velocity of the medium field, u_1 and u_2 are the components of velocity field in x and y direction $\vec{\boldsymbol{u}} = u_1\vec{\boldsymbol{\imath}} + u_2\vec{\boldsymbol{\jmath}}$, respectively. Equation 41 consists of three fundamental linearized planar governing equations when the medium has an angular velocity field in a plane. By rewriting the equation 41, we have:

$$\frac{\partial p}{\partial t}-\omega y\frac{\partial p}{\partial x}+\omega x\frac{\partial p}{\partial y}+\rho C^2\left(\frac{\partial u_1}{\partial x}+\frac{\partial u_2}{\partial y}\right)=0, \qquad \text{Eq. (42)}$$

$$\frac{\partial u_1}{\partial t}+\left(-\omega y\frac{\partial u_1}{\partial x}+\omega x\frac{\partial u_1}{\partial y}\right)-\omega u_2-\omega^2 x+1/\rho_0\left(\frac{\partial p}{\partial x}\right)=0, \qquad \text{Eq. (43)}$$

$$\frac{\partial u_2}{\partial t}+\left(-\omega y\frac{\partial u_2}{\partial x}+\omega x\frac{\partial u_2}{\partial y}\right)+\omega u_1-\omega^2 y+1/\rho_0\left(\frac{\partial p}{\partial y}\right)=0. \qquad \text{Eq. (44)}$$

We are interested in driving all the equations based on velocity (u_1 and u_2) because the boundary conditions can be simplified and represented by just velocity as the variable. Therefore, we need to generate more equations to substitute all terms with p for the equivalent terms consisting of u_1 and u_2. In taking partial derivatives of the three equations with respect to t, x and y, more necessary equations are generated.

$$\frac{\partial}{\partial x}eq.(42)=\frac{\partial^2 p}{\partial x\partial t}-\omega y\frac{\partial^2 p}{\partial x^2}+\omega\frac{\partial p}{\partial y}+\omega x\frac{\partial^2 p}{\partial x\partial y}+\rho_0 c_0^2\left(\frac{\partial^2 u_1}{\partial x^2}+\frac{\partial^2 u_2}{\partial x\partial y}\right)=0, \qquad \text{Eq. (45)}$$

$$\frac{\partial}{\partial y}eq.(42)=\frac{\partial^2 p}{\partial y\partial t}-\omega\frac{\partial p}{\partial x}-\omega y\frac{\partial^2 p}{\partial x\partial y}+\omega x\frac{\partial^2 p}{\partial y^2}+\rho_0 c_0^2\left(\frac{\partial^2 u_1}{\partial x\partial y}+\frac{\partial^2 u_2}{\partial y^2}\right)=0, \qquad \text{Eq. (46)}$$

$$\frac{\partial}{\partial x} eq.(43) = \frac{\partial^2 u_1}{\partial x \partial t} + \left(- \omega y \frac{\partial^2 u_1}{\partial x^2} + \omega \frac{\partial u_1}{\partial y} + \omega x \frac{\partial^2 u_1}{\partial x \partial y} \right) - \omega \frac{\partial u_2}{\partial x} - \omega^2 + \frac{1}{\rho_0} \left(\frac{\partial^2 p}{\partial x^2} \right) = 0, \quad \text{Eq. (47)}$$

$$\frac{\partial}{\partial y} eq.(43) = \frac{\partial^2 u_1}{\partial y \partial t} + \left(-\omega \frac{\partial u_1}{\partial x} - \omega y \frac{\partial^2 u_1}{\partial x \partial y} + \omega x \frac{\partial^2 u_1}{\partial y^2} \right) - \omega \frac{\partial u_2}{\partial y} + \frac{1}{\rho_0} \left(\frac{\partial^2 p}{\partial x \partial y} \right) = 0, \quad \text{Eq. (48)}$$

$$\frac{\partial}{\partial t} eq.(43) = \frac{\partial^2 u_1}{\partial t^2} + \left(- \omega y \frac{\partial^2 u_1}{\partial x \partial t} + \omega x \frac{\partial^2 u_1}{\partial y \partial t} \right) - \omega \frac{\partial u_2}{\partial t} + \frac{1}{\rho_0} \left(\frac{\partial^2 p}{\partial x \partial t} \right) = 0, \quad \text{Eq. (49)}$$

$$\frac{\partial}{\partial x} eq.(44) = \frac{\partial^2 u_2}{\partial x \partial t} + \left(- \omega y \frac{\partial^2 u_2}{\partial x^2} + \omega \frac{\partial u_2}{\partial y} + \omega x \frac{\partial^2 u_2}{\partial x \partial y} \right) + \omega \frac{\partial u_1}{\partial x} + \frac{1}{\rho_0} \left(\frac{\partial^2 p}{\partial x \partial y} \right) = 0, \quad \text{Eq. (50)}$$

$$\frac{\partial}{\partial y} eq.(44) = \frac{\partial^2 u_2}{\partial y \partial t} + \left(-\omega \frac{\partial u_2}{\partial x} - \omega y \frac{\partial^2 u_2}{\partial x \partial y} + \omega x \frac{\partial^2 u_2}{\partial x \partial y} \right) + \omega \frac{\partial u_1}{\partial y} - \omega^2 + \frac{1}{\rho_0} \left(\frac{\partial^2 p}{\partial y^2} \right) = 0, \quad \text{Eq. (51)}$$

$$\frac{\partial}{\partial t} eq.(44) = \frac{\partial^2 u_2}{\partial t^2} + \left(- \omega y \frac{\partial^2 u_2}{\partial x \partial t} + \omega x \frac{\partial^2 u_2}{\partial y \partial t} \right) + \omega \frac{\partial u_1}{\partial t} + \frac{1}{\rho_0} \left(\frac{\partial^2 p}{\partial y \partial t} \right) = 0. \quad \text{Eq. (52)}$$

Finally, after the substitution process, we have two planar fundamental equations just in terms of u_1 and u_2, and their time spatial derivatives

$$-2\omega x \left(\frac{\partial^2 u_1}{\partial y \partial t} \right) + 2\omega y \left(\frac{\partial^2 u_1}{\partial x \partial t} \right) - \omega^2 y^2 \left(\frac{\partial^2 u_1}{\partial x^2} \right) + \omega^2 y \left(\frac{\partial u_1}{\partial y} \right) + 2\omega^2 xy \frac{\partial^2 u_1}{\partial x \partial y} + \omega^2 x \left(\frac{\partial u_1}{\partial x} \right) - \omega^2 x^2 \left(\frac{\partial^2 u_1}{\partial y^2} \right) + c_0^2 \left(\frac{\partial^2 u_1}{\partial x^2} + \frac{\partial^2 u_2}{\partial x \partial y} \right) - \left(\frac{\partial^2 u_1}{\partial t^2} \right) - \omega^2 u_1 = 0, \quad \text{Eq. (53)}$$

$$-2\omega x\left(\frac{\partial^2 u_2}{\partial y \partial t}\right)+2\omega y\left(\frac{\partial^2 u_2}{\partial x \partial t}\right)-\omega^2 y^2\left(\frac{\partial^2 u_2}{\partial x^2}\right)+\omega^2 y\left(\frac{\partial u_2}{\partial y}\right)$$

$$+2\omega^2 xy\frac{\partial^2 u_2}{\partial x \partial y}+\omega^2 x\left(\frac{\partial u_2}{\partial x}\right)-\omega^2 x^2\left(\frac{\partial^2 u_2}{\partial y^2}\right)+c_0^2\left(\frac{\partial^2 u_2}{\partial y^2}+\frac{\partial^2 u_1}{\partial x \partial y}\right) \quad \text{Eq. (54)}$$

$$-\left(\frac{\partial^2 u_2}{\partial t^2}\right)-\omega^2 u_2=0.$$

Equations 53 and 54 are the planar wave equations when the medium has an angular velocity ω with respect to the velocity field components u_1 and u_2. If the medium is at rest (ω=0), the equations are simplified as the form of two dimensional wave equations:

$$c_0^2\left(\frac{\partial^2 u_1}{\partial x^2}+\frac{\partial^2 u_2}{\partial x \partial y}\right)-\left(\frac{\partial^2 u_1}{\partial t^2}\right)=0 \quad \text{Eq. (55)}$$

$$c_0^2\left(\frac{\partial^2 u_2}{\partial y^2}+\frac{\partial^2 u_1}{\partial x \partial y}\right)-\left(\frac{\partial^2 u_2}{\partial t^2}\right)=0 \quad \text{Eq. (56)}$$

where the equations 55 and 56 are the planar expansion of equation 17.

CHAPTER III

NONRECIPROCITY SIMULATION IN COMSOL

Numerical simulations were done using COMSOL Multiphysics software Ver. 5.2. (Burlington MA). The software has a standard mathematical module to numerically simulate an arbitrary second order partial differential equation with constant (or variable) coefficients. The general form of a partial differential equation provided by the software is

$$e_a \frac{\partial^2 \vec{\boldsymbol{u}}}{\partial t^2} + d_a \frac{\partial \vec{\boldsymbol{u}}}{\partial t} + \nabla.(-cc\nabla\vec{\boldsymbol{u}} - \alpha\vec{\boldsymbol{u}} + \gamma) + \beta.\nabla\vec{\boldsymbol{u}} + a\vec{\boldsymbol{u}} + f = 0, \qquad \text{Eq. (57)}$$

where e_a, e_a, cc, α, γ, β, a, and f are standard forms of a general partial differential equation in COMSOL, which should be defined by user. According to the following equations, the coefficients should be set in order to enter the governing equations 53 and 54 in COMSOL:

$$e_a = \begin{bmatrix} -1 & 0 \\ 0 & -1 \end{bmatrix};\ \alpha = [0];\ d_a = [0];\ \beta = 0;\ \gamma = 0$$
$$cc = \begin{bmatrix} -c^2 & 0 \\ 0 & -c^2 \end{bmatrix};\ a = \begin{bmatrix} -\omega^2 & 0 \\ 0 & -\omega^2 \end{bmatrix};\ f = \begin{bmatrix} f_1 \\ f_2 \end{bmatrix}$$
$$f_1 = \left[-2\omega x \frac{\partial^2}{\partial y \partial t} + 2\omega y \frac{\partial^2}{\partial x \partial t} - \omega^2 y^2 \frac{\partial^2}{\partial x^2} + \omega^2 y \frac{\partial}{\partial y} + 2\omega^2 xy \frac{\partial^2}{\partial x \partial y} + \omega^2 x \frac{\partial}{\partial x} - \omega^2 x^2 \frac{\partial^2}{\partial y^2}\right] u_1, \qquad \text{Eq. (58)}$$
$$f_2 = \left[-2\omega x \frac{\partial^2}{\partial y \partial t} + 2\omega y \frac{\partial^2}{\partial x \partial t} - \omega^2 y^2 \frac{\partial^2}{\partial x^2} + \omega^2 y \frac{\partial}{\partial y} + 2\omega^2 xy \frac{\partial^2}{\partial x \partial y} + \omega^2 x \frac{\partial}{\partial x} - \omega^2 x^2 \frac{\partial^2}{\partial y^2}\right] u_2,$$

where ω is the angular velocity, cc is the wave sound in standard condition (c_0 in 25^0 C temperature

and 100 KPa pressure). The parameters defined for simulation are listed in Table 1.

Table 1. The global parameters defined in the COMSOL (constant values). The Parameters required to be determined as the global constant parameters in COMSOL.

Parameter	Expression	value
ω	Angular Velocity	0-1000 [rad/s]
C	Speed Sound	based on the medium (343 [m/s] in air)
Ω	Wave Frequency	4 KHz, 7 KHz, 10 KHz
Tf	Wave Period	1/ Ω [s]

1. Smooth Function

The traveling wave is a sinusoidal wave propagating from one internal side of the circulator to another. The simulation process is applied to analyze the wave propagation in a rotating medium. Because the sine wave is continuous, we need to cut the signal by using a step function. This process creates numerical problems, especially at the beginning and end of the signal, because the cut sinusoidal function derivatives cannot be defined at these points. This results in the numerical program not converging to meaningful values. This problem can be solved by utilizing smooth exponential functions as they are able to make any discontinuous function infinitely differentiable at the cut points. The smooth function can be defined for the initial rise by the following formula:

$$F(t) = \begin{cases} \dfrac{e^{\frac{-t_f}{t}}}{e^{\frac{-t_f}{t}} - e^{\frac{-t_f}{-t_f - t}}} & 0 < t < t_f \\ 0 & else \end{cases}, \qquad \text{Eq. (59)}$$

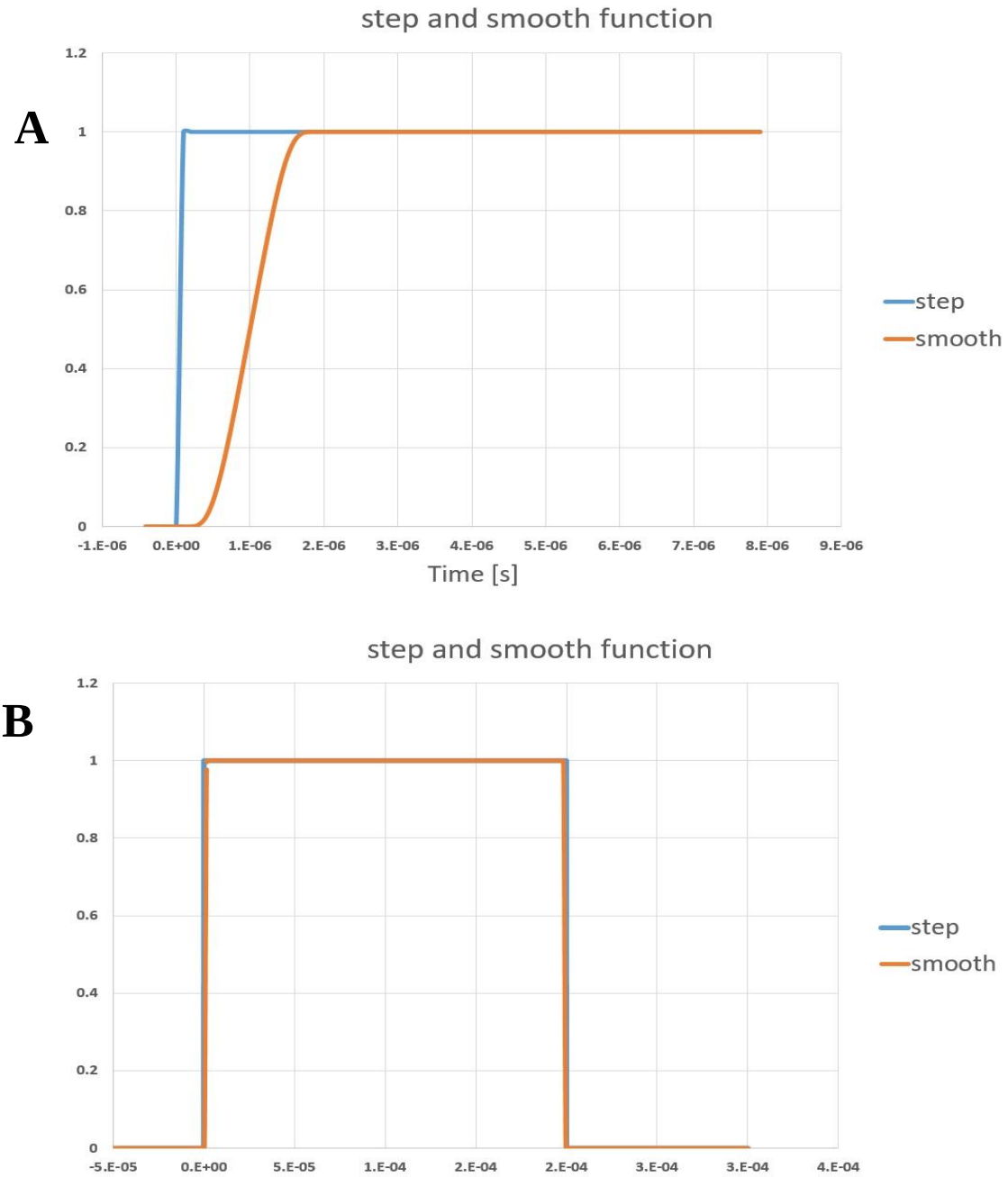

Figure 12 Smooth Function versus Step Function. A) the effect of smooth function at the beginning of signal rise. B) the effect of smooth function on the entire signal period.

where t_f is the one percent of the period time ($0.01/\Omega$). The effect of the function is described by figure 12. The smooth function has a scant effect on the beginning and end points, but the final

function is differentiable in any order.

2. Boundary and initial conditions

A typical circulator is modeled based on figure 12. The internal surfaces of the model are rigid ($\vec{\boldsymbol{u}} = 0$) except for the first quarter of the internal cylinder, which is excited by a single frequency wave for just one period. The time is called time of flight (tf), and it depends on the exciting frequency Ω (tf = 1/ Ω). The equation of the exciting wave is:

$$g(t) = \begin{cases} 0.01\sin(\Omega t)\hat{\boldsymbol{r}} & 0 < t < t_f \\ 0 & else \end{cases}, \qquad \text{Eq. (60)}$$

where $\hat{\boldsymbol{r}} = \cos\theta\ \vec{\boldsymbol{\imath}} + \sin\theta\ \vec{\boldsymbol{\jmath}}$ (unit vector in r direction). Nevertheless, equation 60 is not continuous and differentiable at the boundary points. Utilizing the smooth function defined in section 2.2, one period of the smooth signal propagates through the medium from the internal cylinder to the external.

The time needed for simulation is equal to the time in which the wave passes through the medium (grey area in figure 13) from the small cylinder to the larger. The radii of the small and large cylinder are 0.05 m and 0.4 m, respectively. It is then intuitive that the distance across which the wave passes is 0.35 m. Considering air as the medium, the maximum time for time dependent analysis is 0.35/343= 10.2e-4 s. Therefore, the total time was set around 5.8e-4 s; moreover, the time step was chosen to be 1e-7 s. This time step is equal to the lowest time of flight needed for the smooth function (Ω=10KHz).

3. Time-dependent Results

The outgoing wave propagates in radial direction based on equation 60. This means that the single frequency wave does not have any tangential component (in θ direction); therefore, based on the 1D wave propagation formula (equation 61), the wave should bounce exactly between the two inner sides of the small and large cylinders.

$$\begin{cases} \dfrac{\partial^2 u}{\partial t^2} = c_0^2 \dfrac{\partial^2 u}{\partial r^2} \quad 0 < t < t_f \\ BC \qquad \begin{Bmatrix} u(0,t) = h(t) \\ u(L,t) = 0 \end{Bmatrix} \\ IC \qquad \begin{Bmatrix} u(r,0) = 0 \\ u_t(r,0) = 0 \end{Bmatrix} \end{cases}, \qquad \text{Eq. (61)}$$

where, h(t) is the motivation signal which is a combination of equation 60 and the smooth function.Equation 61 is valid when the medium is initially at rest (ω=0). Therefore, the propagated wave should bounce without any deviation from r direction. Rotation of the medium can deviate the outgoing wave from radial direction, and this deviation has a definable relationship with the angular velocity field.

Definition of a criterion showing to what degree the propagated wave rotates around the internal cylinder is necessary because the propagated wave from the blue line (figure 12) spreads over the medium. Therefore, our solution for calculating the deviation was to take a snapshot of the wave pulse at a specific time, t=580 μs. At this moment, the wave front was roughly 20 cm away from the source and had not reached the outer circle. We located the center of the area of the top 10% of the wave pulse and measured its angle deviation from 45^0. In order to assess our metric, we measured the center of the area of the top 30% of the wave pulse as well. The results are depicted

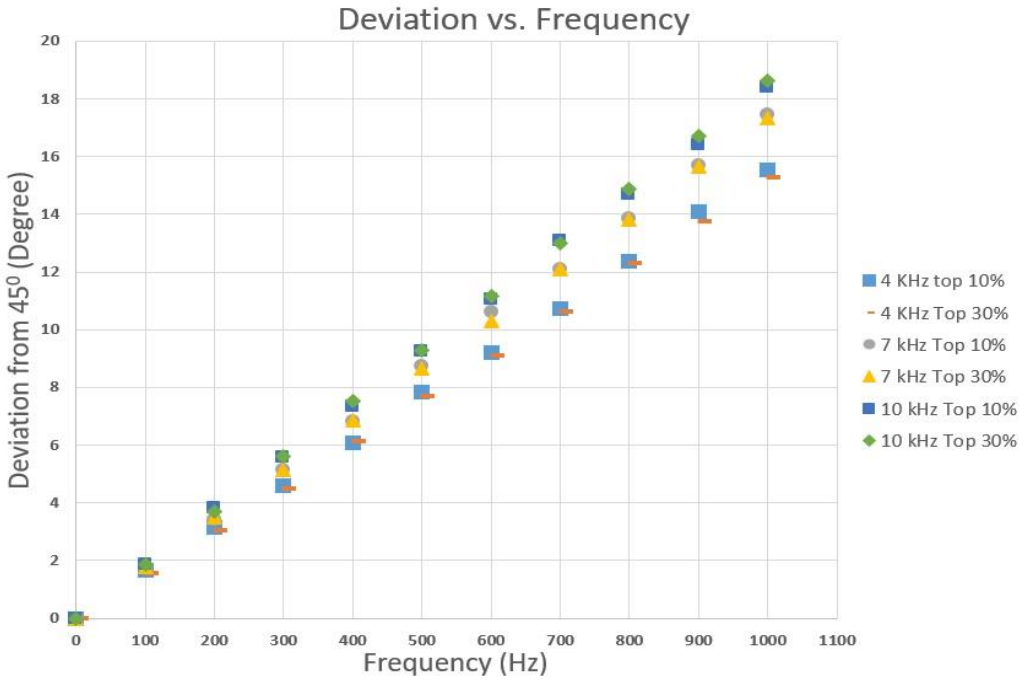

Figure 14 Results of Deviation. Numerical results of deviation from the symmetry axis when the wave pulse is 20 cm away from the source and the excitation frequencies are 4, 7, and 10 kHz. Deviation is measured as the angle of the center of the area of the top 10% and 30% of the wave pulse relative to the symmetry axis

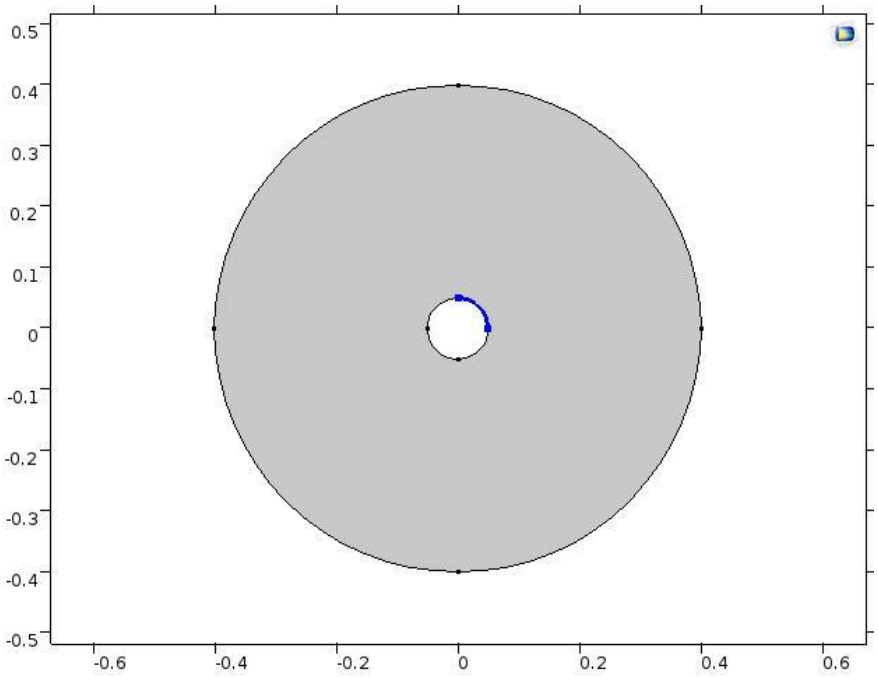

Figure 13 The geometry of the circulator simulated in COMSOL. The blue line indicates the first quarter having initial condition according to equation 60. The rest boundaries are rigid ($\vec{\boldsymbol{u}} = 0$). All dimension are in meter.

in figure 14. As evident in this graph, there is not much difference between the two metrics for the top 10% and 30%. This graph shows that, as expected, the deviation and non-reciprocity increase with rotation speed. The code and the process to get the required data for figure 15 are described in the appendix.

Equations 53 and 54 were numerically simulated using COMSOL. All of the walls are were set to be rigid ($\boldsymbol{u}$ =0) except for a quarter (0-90^o) of the inner circle where the wall served as the excitation source. The wave enters from this one quarter for one period of a sine wave. The first and last 1% part of the one period is smoothed out using an exponential function ($e^{-1/x}$) so that all time derivatives exist to avoid numerical artifacts. The medium is air at room pressure and temperature. The simulation is done for one wave length of a sine wave at three excitation frequencies; 4, 7 and 10 kHz. The air rotation speed varies from 0-1000 rad/s by increments of 100. As it can be seen in figure 15, when ω=0, the wave propagates with no deviation from the axis of symmetry, which lies at 45^o. While, for ω=700, the wave front does deviate from the axis

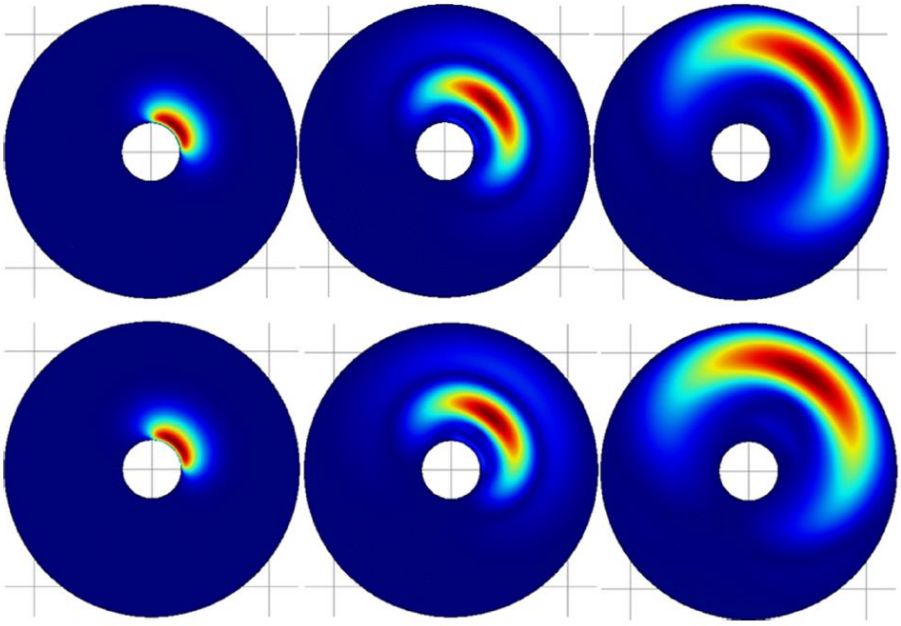

Figure 15 Propagation of one period sine wave. when ω=0 (top) and in a rotating medium with ω=700 rad/s (bottom)

of symmetry.

4. Frequency domain results

The main aim of this project is to show breaking reciprocity in an acoustic circulator using a rotational medium. Although a deviation from the line of symmetry was observed in figure 14, it does not indicate that this deviation was due to the non-reciprocity. Additional analysis is required to prove that non-reciprocity happens due to an angular velocity field; thus, non-reciprocity causes the deviation observed in section 3.1. According to the principle of reciprocity, defining two arbitrary points as the source points is required. The point source locations are shown in figure 16. Although the locations of the points were chosen arbitrarily, they are reasonably far enough from the boundaries. Because the source point is singular, it should be far from the

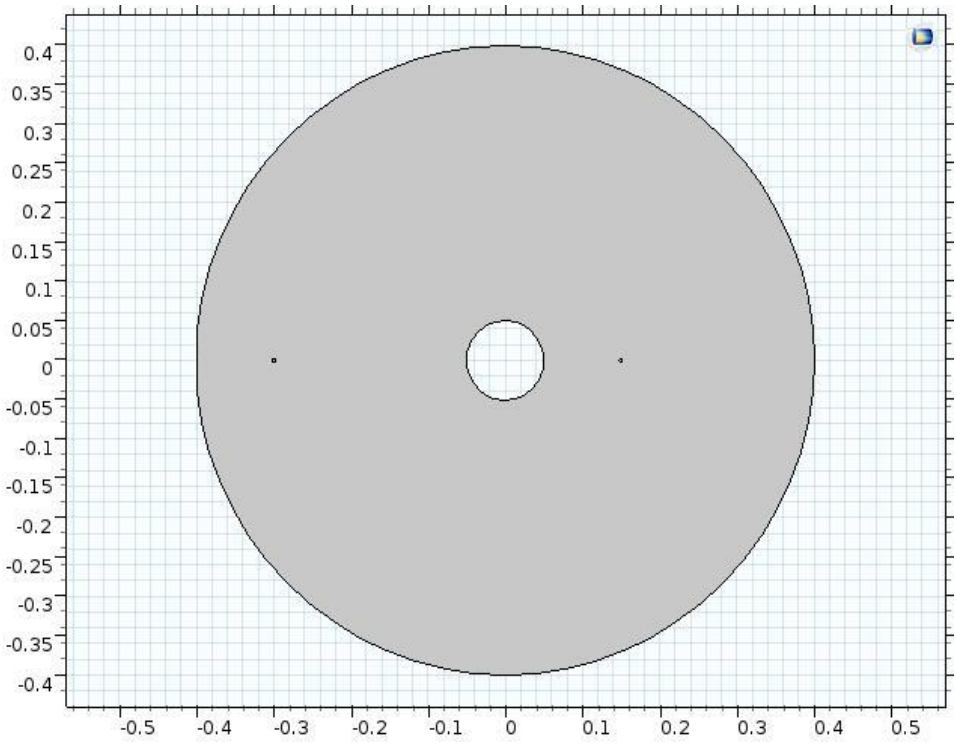

Figure 16 The location of two source points. The captured image from COMSOL showing the location of two source points in the model

boundaries to guarantee that the numerical process converges.

In the case of having a moving medium with the velocity $\vec{\boldsymbol{V}} = r\omega\hat{\boldsymbol{\theta}}$, we cannot define the velocity potential, so we are not able to use the aforementioned proof for reciprocity. Nevertheless, it is not guaranteed that the reciprocity is broken. Here, we show by example that the reciprocity does not generally hold in such a system. According to figure 17, the two points serve as a source and measurement point interchangeably similar to the reciprocity proof we discussed before. Subsequently we numerically solve two different fields, A and B, corresponding to different source points, 1 and 2. Since we use a single frequency wave, we can assume $u_1(x,y,t) = U_1(x,y)e^{i\tilde{\omega}t}$ and $u_2(x,y,t) = U_2(x,y)e^{i\tilde{\omega}t}$; so equations 53 and 54 can be rewritten as:

$$-2i\omega\tilde{\omega}x\left(\frac{\partial U_1}{\partial y}\right) + 2i\omega\tilde{\omega}y\left(\frac{\partial U_1}{\partial x}\right) - \omega^2y^2\left(\frac{\partial^2 U_1}{\partial x^2}\right) + \omega^2 y\left(\frac{\partial U_1}{\partial y}\right) + 2\omega^2 xy\frac{\partial^2 U_1}{\partial x\partial y} + \omega^2 x\left(\frac{\partial U_1}{\partial x}\right) - \omega^2x^2\left(\frac{\partial^2 U_1}{\partial y^2}\right) + c^2\left(\frac{\partial^2 U_1}{\partial x^2} + \frac{\partial^2 U_2}{\partial x\partial y}\right) + \tilde{\omega}^2U_1 - \omega^2U_1 = 0, \quad \text{Eq. (62)}$$

$$-2i\omega\tilde{\omega}x\left(\frac{\partial U_2}{\partial y}\right) + 2i\omega\tilde{\omega}y\left(\frac{\partial U_2}{\partial x}\right) - \omega^2y^2\left(\frac{\partial^2 U_2}{\partial x^2}\right) + \omega^2 y\left(\frac{\partial U_2}{\partial y}\right) + 2\omega^2 xy\frac{\partial^2 U_2}{\partial x\partial y} + \omega^2 x\left(\frac{\partial U_2}{\partial x}\right) - \omega^2x^2\left(\frac{\partial^2 U_2}{\partial y^2}\right) + c^2\left(\frac{\partial^2 U_2}{\partial y^2} + \frac{\partial^2 U_1}{\partial x\partial y}\right) + \tilde{\omega}^2U_2 - \omega^2U_2 = 0. \quad \text{Eq. (63)}$$

Now we solve equations 62 and 63 numerically using the coefficient form PDE package of COMSOL Multiphysics software. In order to numerically add source points to the system, we first add two small circles of radius 2 mm around points 1 and 2. We then use a point source option offered through the software to add delta functions on the right. The value for this source term is varied until we achieve the same average pressure on the small circles for both fields A and B. The

process is as follows; first we make point 1 a point source with some arbitrary value, and then we solve equations 62 and 63. Now that $\vec{\boldsymbol{u}}$ is found on the whole domain, we can find pressure for the entire domain including the small circle. Equation 41 in frequency domain contains *P* and its derivatives with respect to *x* and *y*. But since $\vec{\boldsymbol{u}}$ is already found everywhere, we can use equations 42 and 43 to replace derivative terms in equation 41 and calculate *P* as:

$$P = \frac{i\rho}{\tilde{\omega}}\Big[(i\tilde{\omega}\omega y - \tilde{\omega}\omega x - \omega^2 x)U_1 + (-i\tilde{\omega}\omega x - \tilde{\omega}\omega y - \omega^2 y)U_2 + (c^2 - \omega^2 y^2)\frac{\partial U_1}{\partial x} + (c^2 - \omega^2 x^2)\frac{\partial U_2}{\partial y} + \omega^2 xy\left(\frac{\partial U_1}{\partial y} + \frac{\partial U_2}{\partial x}\right)\Big] \quad \text{Eq. (64)}$$

This pressure is then averaged on the small circle around the source point. Next, we set point 2 as the source point with some value, and we repeat the process and calculate the pressure. Unless we had an educated guess or a stroke of luck, this pressure is not the same as the previous case. We can linearly adjust the point source value to match these two pressures. At the end of this process, we are guaranteed that *P* at source points are the same for both fields A and B, so by

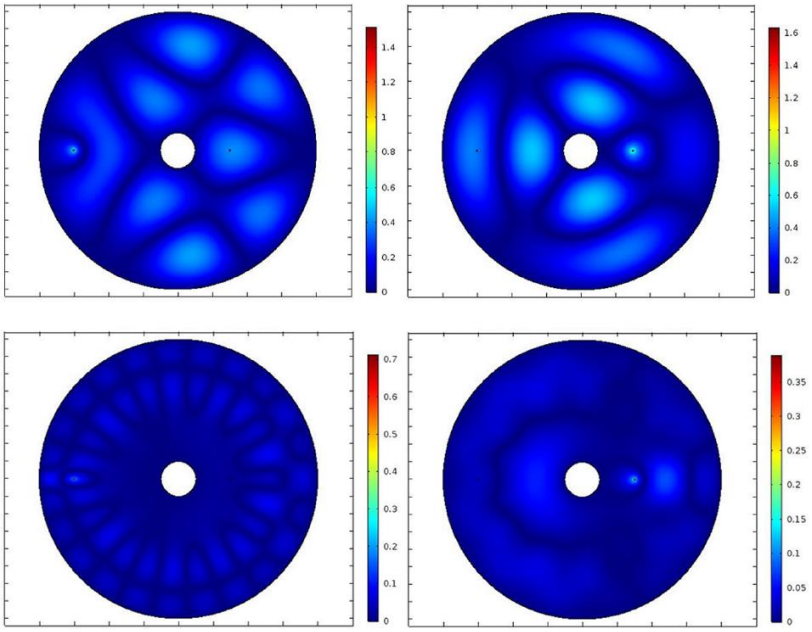

Figure 17 Numerical results for the absolute value of velocity U The no-flow situation is depicted on top (ω=0) and the case of fluid flow of ω=900 rad/s is on the bottom. Point 1 is the source on the right while point 2 is the source point on the left.

measuring the velocity $\vec{\boldsymbol{u}}$ at the other point, we can verify the reciprocity in the system.

In our simulation, we used air at room pressure and temperature for the medium fluid. The excitation frequency is set to 7 kHz. In the case of no flow where $\omega = 0$, we set the pressure at the source point to be 1 Pa (~94 dB). The velocities calculated at measurement points are the same up to the fourth digit; $\boldsymbol{U_{point1}/U_{point2}} = 1.0000$. This, unsurprisingly, verifies that reciprocity exists when there is no flow. However, in the case of fluid flow of $\omega = 900$ rad/s with the same pressure at the source point, we have very different velocities; $\boldsymbol{U_{point1}/U_{point2}} = 1.7567$. This quatitatively proves that the reciprocity is broken in systems in which we have circular flow. Numerical results for both no-flow and circular flow are depicted in figure 18.

In the first part of this dissertation, utilizing a rotating medium in order to break reciprocity in a linear acoustic system was investigated. The definition and the concept of reciprocity, as well as time reversal symmetry, were also discussed in the introduction section. Moreover, we could envision an acoustic circulator in which the fluid rotates like a rigid body. In such a system, rotational velocity enters the differential equation of the system as a cross product term with the sound particle velocity. We investigated and determined that the angular velocity of a medium was the key parameter in wave deviation. A device using this phenomenon can be used as a filter and/or diode, however, to achieve high level of non-reciprocity, the rotation speed has to be meaningfully high.

CHAPTER IV

LIQUID METAL AS AN ACTUATOR

Electromechanical actuators that exploit the Lorentz force law have been used in various applications. The physics involved in these motors allows actuators to be designed having a wide range of sizes and mechanical energy output. Unlike internal combustion engines, these devices produce no pollution: making them suited to applications such as indoor machinery and medical technology. These actuators generally consist of current-carrying wires which move due to the Lorentz force. Depending on the application, the wires are made from differing metals. They are solids and not designed to be stretched or changed in shape. The resulting motion is purely linear or rotational.

For wearable computers, flexibility of the wires and current-carrying elements is crucial. Various materials have been developed to this end. Post et al. [50] developed conductive textiles for use in flexible multilayer circuits. To enhance the electrical conductivity while retaining flexibility, Lacour et al. [51] deposited a thin layer of gold with surface wrinkles on to a polydimethylsiloxane (PDMS) substrate; the resulting strip was an elastic electrical conductor. Gray et al. [52] exploited the fact that metals bend and twist when their cross sections are small enough. They used twisted gold wires on PDMS substrate to produce a stretchable conductor. Siegel et al. [53]used techniques of microfluidics fabrication and injected liquid solder into microfluidic channels. When the solder cools and solidifies, the result is a flexible metallic structure. Dickey et al. [54] investigated various properties of liquid metal eutectic gallium-indium

(EGaIn) injected into a microchannel. Since soft material structures, with liquid metals in their channels, are inherently less prone to mechanical fatigue and fracture, various liquid alloys have been used by other researchers. Gallium is the main element in these alloys because it is one of only five metals that are liquid at room temperature; the others being rubidium, cesium, francium and mercury [55]. The first three are in the alkali metals group and react violently with water, and mercury is highly toxic.

Eutectic gallium-indium (EGaIn) and Galinstan are liquid metal alloys. EGaIn consists of gallium and indium whereas galinstan has a different ratio of gallium to indium, plus tin. As a result of their low toxicity [55, 56], galinstan and EGaIn have been used to fabricate various structures. Flexible interconnections [57-59] have been made using PDMS filled with galinstan. Other devices include inductors [60], microfluidic wireless power systems [61], loudspeakers and microphones [62], contact pressure sensors [63], particle-filled composites, [64] and fluidic antennas [65]. In all of these applications, except for the loudspeaker, the liquid metal works as a sensor or a current-carrying element of the system. In the present work, the liquid metal is used as an actuator, exerting force on the surroundings. This is in essence a new kind of motor in which the 'wires' are flexible, and as such the motions they generate are not restricted to rotational or linear motion. This type of actuator utilizes the Lorentz force in the same way as conventional electromechanical motors, but we may now envision diverse configurations and geometries to generate extraordinarily complex types of motion which are impossible to realize otherwise.

1. Principle of operation

This motor consists of a tube and two permanent magnets. The tube is made of soft elastic material in the shape of a helix and is filled with liquid metal Galinstan (see Fig. 18). This tube is

held between two permanent magnets. The current through the liquid metal is modulated using an amplifier. The generated force is given by the Lorentz force law:

$$d\boldsymbol{F} = id\boldsymbol{l} \times \boldsymbol{B} \qquad \text{Eq. (65)}$$

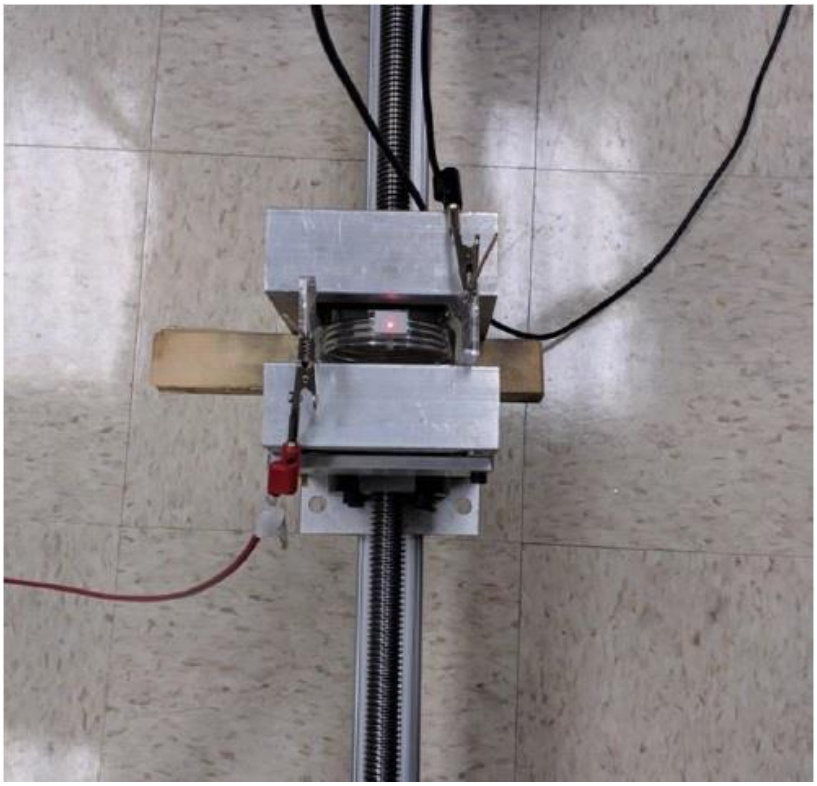

Figure 18 The setup of the helix actuator. Helix made with PTFE vibrating in air while the out-of-plane displacement is measured with a laser Doppler vibrometer.

in which i is the current, B is the magnetic field and dl is the differential length vector parallel to the current. The differential force vectors are in the radial direction, pointing inward or outward according to the direction of the current. As a result, there is no net torque on the structure. By symmetry, the net force is also zero. Since the tube is made with flexible materials. However, these forces induce vibrations in the tube, taking the form of a 'breathing' mode.

In this mechanism, the mass comprises the mass of the tube and the mass of the liquid metal. The stiffness is that of the tube only. During free vibration in air, each helix turn produces

the same amount of vibration force while adding the same amount of mass to the overall structure. Consequently, increasing the number of turns would not affect the displacement nor the acceleration.

2. Experimental procedure

For the tube we used three materials: polyurethane, polyvinyl chloride (PVC) and perfluoroalkoxy alkanes (PFA). All tubes had an external diameter of 1/8 in and an internal diameter of 1/16 in. The diameter of the helix was 2 inches in all cases, and there were four turns (see Fig. 19a.) The helix is fixed at the bottom by a thin structure. The helix turns are also tied together by thin hollow structures, as shown in Fig. 19b.

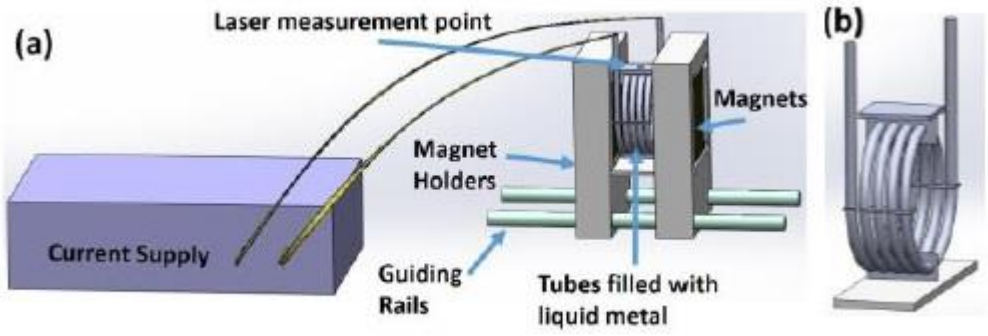

Figure 19 The sketch of actuator and setup (a) Schematic of the liquid metal electromechanical system. (b) Helix coil constrained at the bottom. The turns are tied together in three further locations

The magnets were off-the-shelf NdFeB Grade N52 permanent magnets, purchased from K&J Magnetics. Their dimensions were 3×3×1 in. The magnets were kept separate by an aluminum structure with a steel lead screw. The magnetic field strength was measured as 0.3 T in the middle of the space between the magnets and is unchanged when the tubes filled with liquid metal are in place. The current was provided by a current amplifier and the input frequency range

was 20 Hz to 5 kHz (500 points). As the resistance of the tube filled with Galinstan was 0.1 Ω, we use a 3.07 Ω resistor in series with the motor to reduce the load on the amplifier, and also measure the current. The peak current was set to be 0.1, 0.3, 0.5 and 0.7A, depending on the tube material. The out-of-plane displacement was measured by a Polytec PDV-100 Laser Doppler vibrometer (LDV).

The liquid metal was injected into the tubes by an air pump. After the tubes were filled with liquid metal, copper tubes were pushed through the liquid to make contact with the galinstan. These copper tubes also provide space for the galinstan to move in and out of the tube when the tubes flex. To check the connection and verify the absence of disconnecting bubbles in the tube, the resistance of the tube is measured before and after the experiment.

3. Experimental results

Fig.s 20-22 shows the measured displacement plotted against frequency for the three different tube materials and various input currents. Moreover, the normalized displacement is plotted on a linear scale against frequency for the polyurethane tube. The displacement varies linearly with the input current. The first resonant frequency is the strongest one in all cases. This is expected, as the distributed forces on the tubes are uniform and have radial symmetry. The first resonant frequency and its amplitude depend on the hardness of the tube (see figures 20-22). The elastic modulus of polyurethane, PFA and PVC were calculated from the hardness of the material as quoted by the manufacturer. We used the empirical relation due to Gent [66]:

$$E = \frac{0.0981(56 + 7.62336\boldsymbol{S})}{0.137505(254 - 2.54\boldsymbol{S})} \qquad \text{Eq. (66)}$$

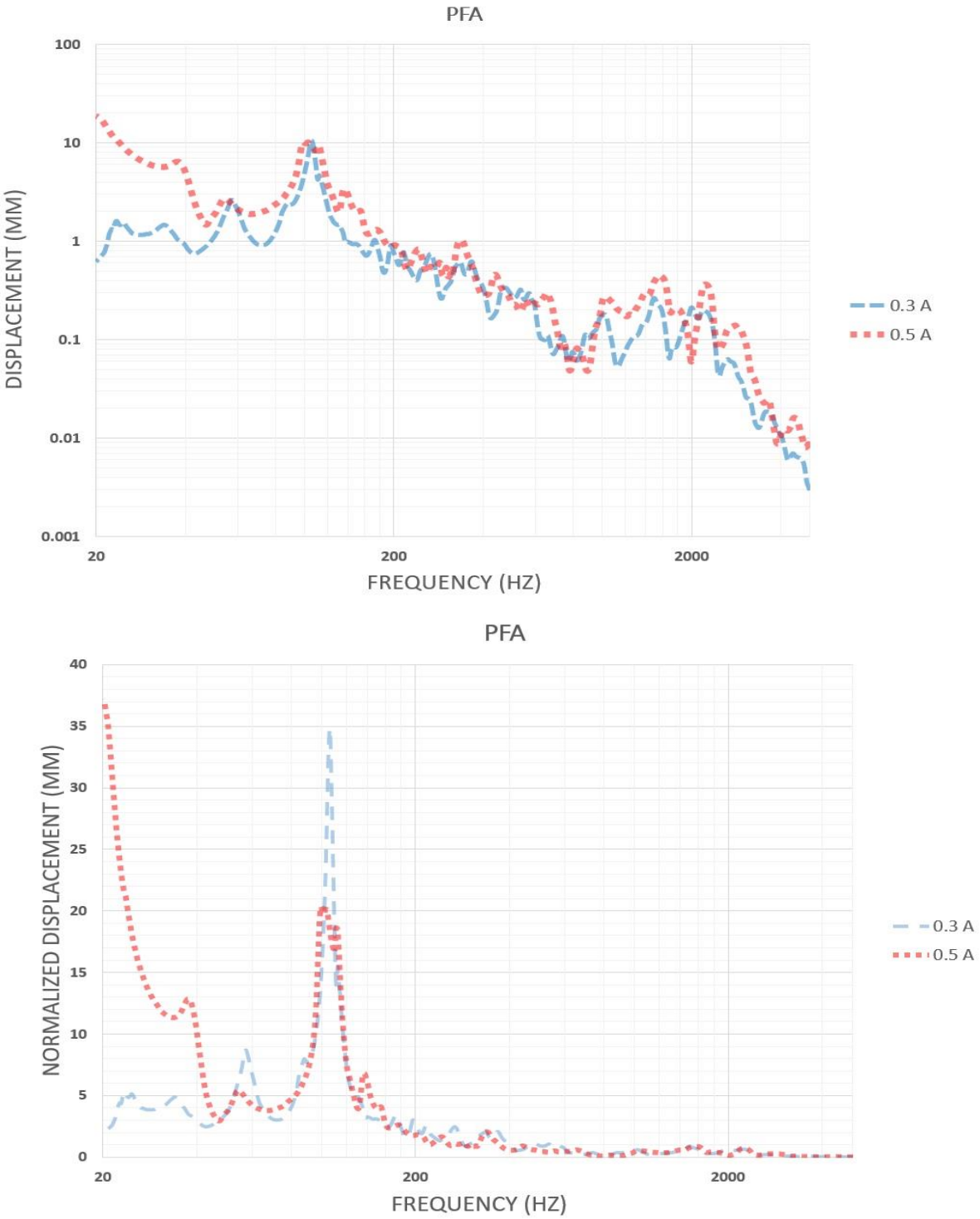

Figure 20 Displacement vs frequency for PFA

where E is the Young's modulus in MPa, and **S** denotes the type A durometer hardness.

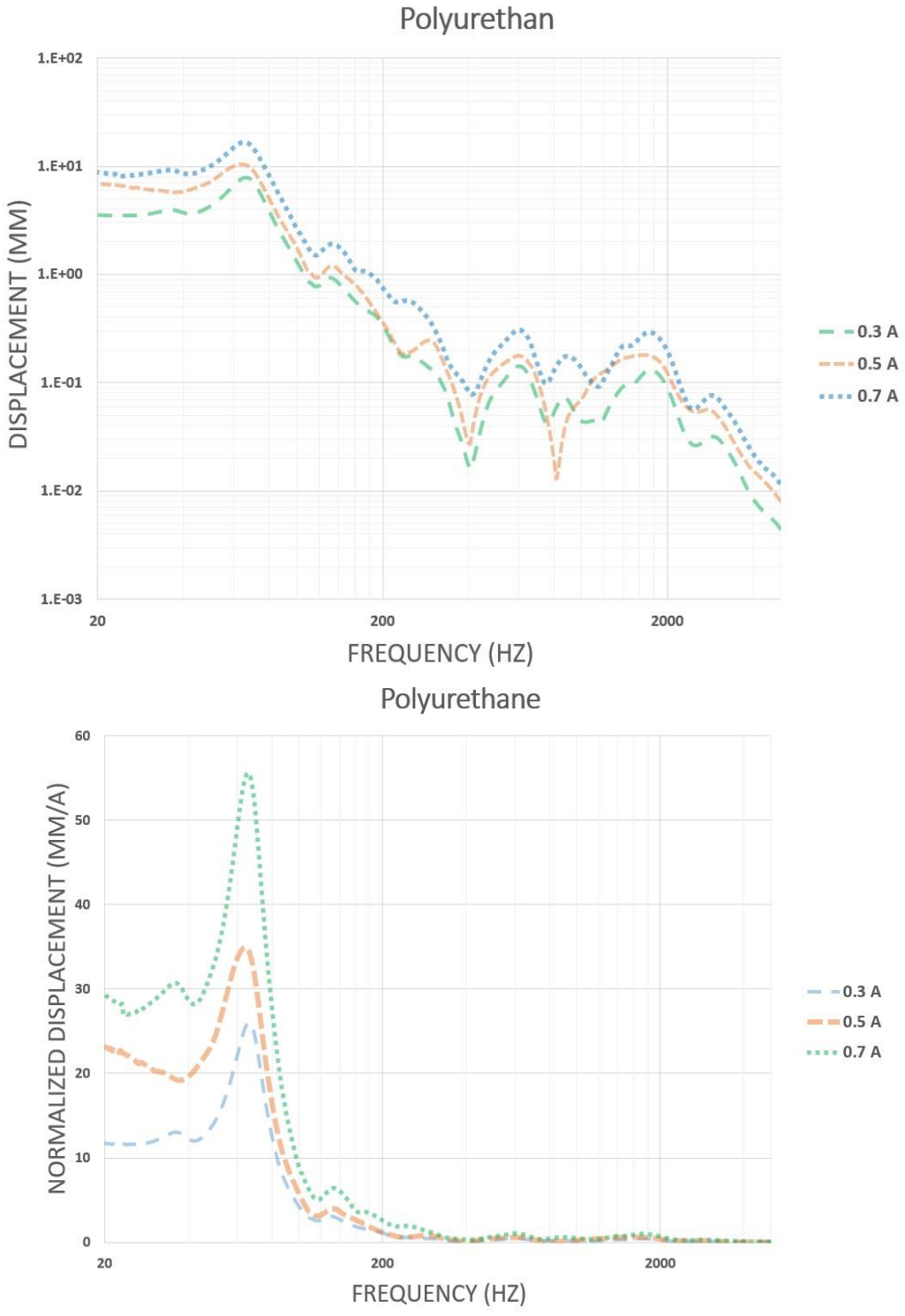

Figure 21 Displacement vs frequency for Polyurethane

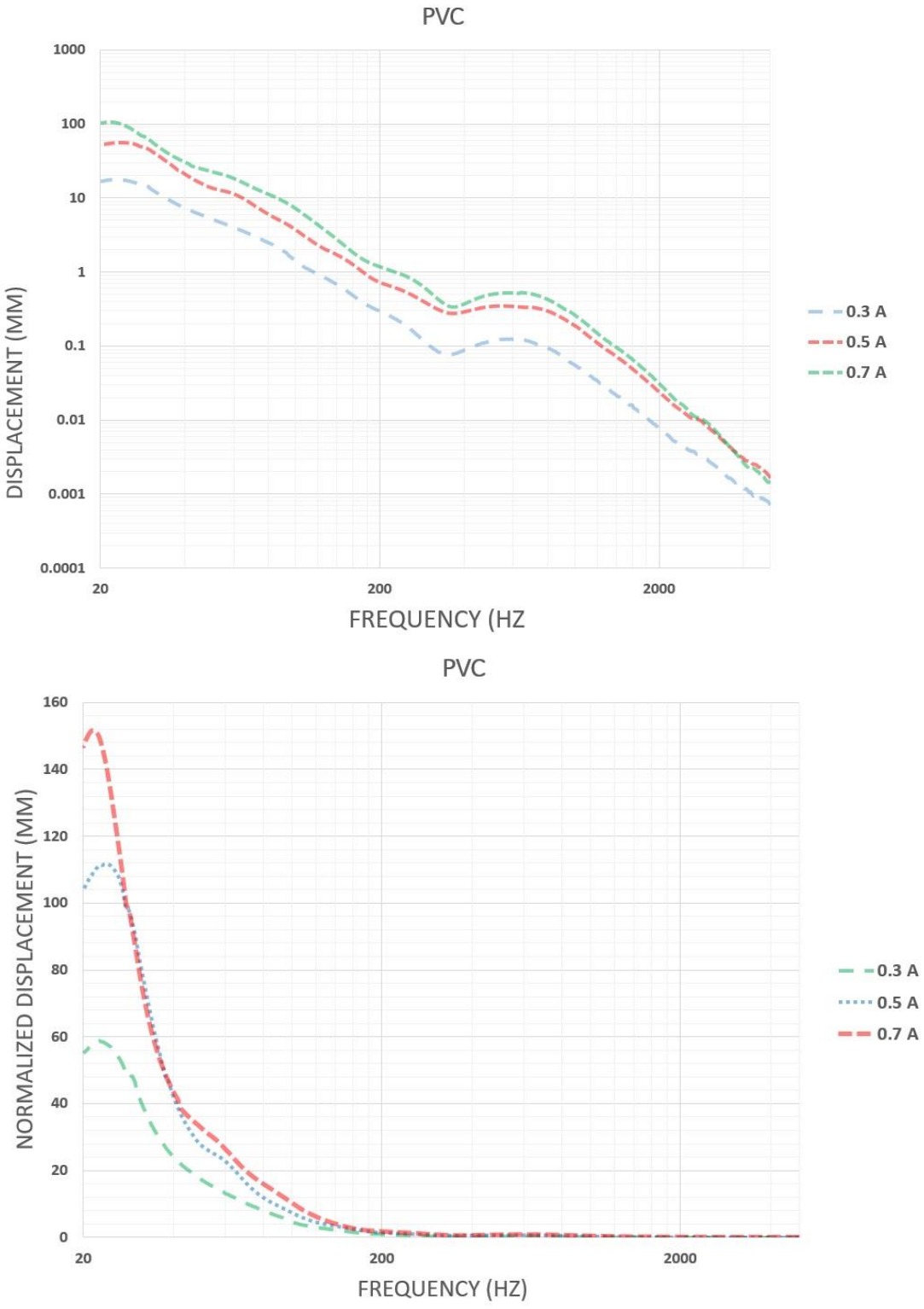

Figure 22 Displacement vs frequency for PVC

Values of the Young's modulus were calculated to be 43.83, 4.43 and 67.17 MPa for polyurethane, PVC and PFA, respectively.

4. Modeling Results

Resonance frequencies are an exceptionally reliable characteristic of a mechanical system. They are essentially eigenvalues for which the mechanical energy Lagrangian takes its extremum values [67]. We therefore use the experimental resonance frequencies as a criterion to validate our model. As mentioned above, as a result of the symmetry in force distribution and the geometry involved, the first resonant frequencies were excited to a greater extent in this experiment.

To model the vibration of this motor, we considered a single loop of the helix. In air, the vibration of a single loop of a helix should not differ from the vibration of multiple turns. The liquid metal moves in the tube as the Lorentz force causes the tube to vibrate. This motion of the liquid metal induces friction with the tube and there are other complex interactions caused by the fluid flow. For simplicity, we neglect such effects due to movement of the liquid metal in the tube.

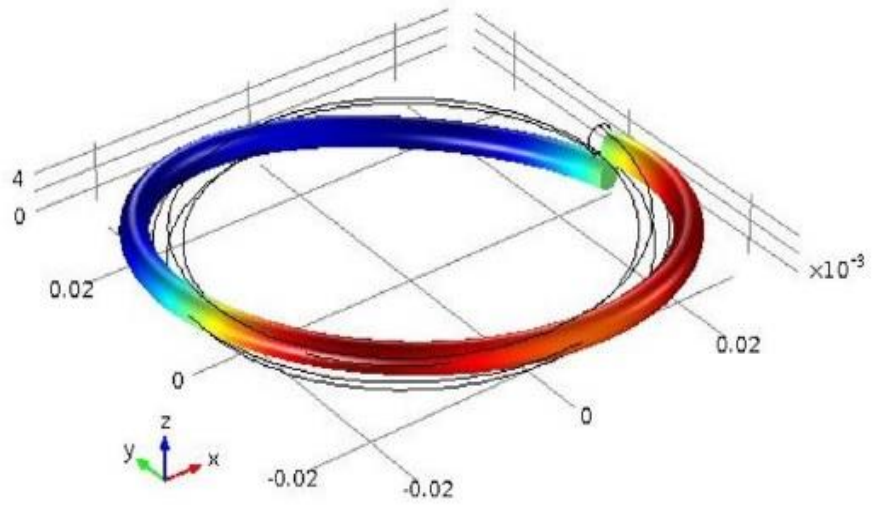

Figure 23 Fundamental frequency of the tube. Heat map of the displacement eigenmode in the y direction associated with the first mode for polyurethane.

In our model, we assume a hollow tube with the elastic constants defined in the previous section. In calculating the mass of the tube, we consider the mass of the liquid metal as if it were distributed uniformly on the tube wall. Based on the volume of the liquid metal in one loop and its density, we calculate the mass of the liquid metal. This mass is then assumed to be distributed on the tube wall. We accordingly define a density for this distributed mass as the mass of the liquid metal divided by the volume of the wall. The density of the hollow tube in our model is then calculated as the density of the tube material plus the calculated density of the distributed material.

Table 2 sets out the experimental resonance frequency and the ones simulated from the model in COMSOL. There is excellent agreement between these frequencies for polyurethane and PVC. For PFA, however, there is approximately 25% error. We attribute this error to the way in which these tubes were connected as a structure, which were not totally isolated. In our experiments, the coupling to the ground was stronger for the PFA because of the tightness of the fit to the pipe holders. We nevertheless see the resonant frequencies increase as the elastic constant increases. The first resonant frequency is a radial breathing mode, as expected. Figure 24 shows the first displacement eigenmode projected in the y direction for polyurethane.

Table 2: First resonant frequency, calculated by model and measured experimentally.

	Polyurethan	PFA	PVC
Experimental	67 Hz	106 Hz	24 Hz
FEM model	69 Hz	75.23 HZ	25.19 Hz

We have investigated new types of actuators in which a breathing mode is activated. Tubes filled with liquid metal Galinstan were used to study this type of motion. We used various tube materials

and measured the output displacement versus frequency in the range 20 Hz to 5 kHz. The actuator has a linear response in relation to the input current. In the model, it was found that the effect of liquid metal motion can be neglected in simple designs; it is possible to make narrow tubes so as to increase the resonant frequencies by reducing the liquid metal mass and increasing the stiffness. Although we used a simple helix configuration for the tubes, and the design is simple, this type of actuator can be deployed in much more complex geometries in order to better study complex motions and motors. Movement of liquid mass can, for instance, be incorporated into the design by adding a reservoir for liquid metal in the tube, or by making channels of complex shape so as to focus energy within some region.

CHAPTER V

PERSITALTIC AND VALVELESS MICROPUMP

Lab-on-a-chip (LOC) systems have been extensively studied since microfluidic systems were introduced. These LOC systems have advantages such as lower material waste, faster analyses, and better processing rates when compared to traditional sampling methods in medical and biological applications [68]. This technology is exceedingly useful in point-of-care testing (POCT) diagnostic systems, which do not require advanced skills for operation [69]. Another approach of LOC systems can be applied in the low aggressive diagnostic methods used to detect cardiovascular diseases [70]. LOC systems need micro-channels that carry biological fluids with volumes varying between 10^{-18} and 10^{-9} liters when the diameter of the channels is in hundreds of micrometers [71]. Other kinds of LOC systems are Organs-on-chips, which have been extensively investigated as a means of characterizing the behavior of cells [72]. Thus, miniaturization and automation in an integrated small chip are the other primary advantages of LOC systems [73]; moreover, high sensitivity [74] with low cost and higher throughput measurement is expected from the LOC systems [75]. Because laminar flow is the usual flow regime of LOC systems [76], the interaction between the fluid and microchannel boundaries is considered negligent and can be overlooked.

The primary components of LOC systems are the microchannels that translate the fluids from the inlet to the outlet. Miniaturization of the microchannels in LOC systems can integrate several laboratory functions into a tiny chip, providing a decent performance in a few square

millimeters area [77]. To do so, micropumps need to be utilized in LOC systems in order to create the essential pressure difference that pushes the biological fluids from the inlet to the outlet. There is considerable diversity in the application of micropumps such as mini/microsatellites or spacecraft [78-80], continuous heat dissipation in space-constrained electronics [81-84], portion exchange methanol fuel cells (PEMFC), or direct methanol fuel cell (DMFC) [85-87], drug delivery and biomedical assays [88-90], microfluidic analysis [91], and cell culturing [92]. This dissertation focuses on introducing a novel pumping method in a generation of peristaltic micropumps constructing LOC fluid flow system. This mechanism can provide microfluidic flows utilizing the Lorentz force law as the main principle applied in the physical actuation.

The actuation part of micropumps generally has been categorized as piezoelectric, electrostatic and electroactive polymer composite, thermal actuation, electromagnetic (EM), magnetohydrodynamic (MHD), electrohydrodynamic (EHD), electroosmotic (EO), bubble-type and evaporation-type, and electrowetting (EW) micropumps [93]. This dissertation mostly concentrates on the mechanical actuation mechanisms applied in the valveless micropump, which will be discussed in section 4.2, and the advantages or disadvantages when compared to the other methods.

1. Piezoelectric Actuators

Piezoelectricity is determined as a linear electromechanical interaction between mechanical and electrical state in an asymmetric crystal [94]. The effect of piezoelectricity is direct when mechanical stress deforms the crystal and causes an electric polarization. The converse effect happens when an external electric force causes, proportionally, mechanical stress in the crystal [94]. One of the most common materials used as a transduction element for piezoelectricity is

quartz; however, the natural singular crystal in nature is limited. Thus, synthetic quartz is a valuable solution for satisfying the huge demand for piezoelectricity advancements [94].

Lead Zirconate Titanium (PZT) is an inorganic compound ceramic material, which has been extensively used in piezoelectric sensors and actuators, even in micro or nanoscale [95]. Moreover, PZT can be used in biomedical sensing centered around silicon-based technology [96]. The PZT sensors have advantages such as small size, excellent signal-to-noise ratios, low hysteresis, tolerable in harsh environmental conditions, and high repeatabilities [96]. Additionally, they can be used to fabricate planar microelectromechanical sensors [97]. Planar sensors and actuators have advantages such as considerable efficiencies and lower input power when compared to other types of sensor patterns [96].

PZT actuating systems have commonly been utilized as actuators for micropumps. PZT micropumps with check valves and flexible diaphragms made of PDMS are the common type of PZT micropumps. Wang et al. [98, 99] modified a flexible micropump including a PDMS layer as a diaphragm, a compressible space before the check valves, and two PZT sheets as the actuators to increase the average flow rate. They could actuate the pump in the resonant frequency (490 Hz) with the maximum efficiency. The simulation of PZT actuators has been performed in various researches. There have been efforts to demonstrate the robustness of the failure detection algorithm [100]. Other wors addressed the best actuation profile with the minimum voltage and the maximum deflection [101]. Buckling and bending modes for higher deflection have been investigated in other works[102]. Triple PZT vibrators for better performance were also studied [103], and the effect of cross sectional shape of microneedles on pain in PZT based micropumps [104] were investigated. Other works include resonant diaphragm gas pump [105] and various

passive check valves for backflow reduction [106].

A flexible pump can be created using Lead Zirconate Titanate (PZT) as an actuator in combination

with a flexible diaphragm. However, a high actuation voltage is needed to activate PZT, and in that small configuration, the PZT has a small stroke [93]. There have been other candidates for the actuation component of a flexible pump, such as electrostatic actuation, electroactive polymers, electromagnetic (EM) actuators, and magnetohydrodynamic micropumps (MHD) [93]. Each actuating system has been developed due to some specific advantage(s) over other mechanisms.

2. Electrostatic and Electroactive Actuators

Electrostatic actuating systems can be utilized in micropumps, high-frequency switches, oscillators, and sensors [107]. The actuation system is relatively simple compared to the PZT shown in figure [108]. This figure displays the simplest actuating process, whereas the top electrode is fixed, and the electrostatic force bends the bottom electrode. The calculation of the force, F, and the resulted pressure, P, in the chamber can be calculated by the following formula [109]:

$$\frac{Eh^3}{12(1-\nu^2)}\nabla^4\omega - h\sigma_r\left(\frac{\partial^2\omega}{\partial x^2} + 2\frac{\partial^2\omega}{\partial x\partial y} + \frac{\partial^2\omega}{\partial y^2}\right) + h\rho_m\frac{\partial^2\omega}{\partial t^2} = F\,, \qquad \text{Eq. (67)}$$

where E, h, ν, w, ρ_m, σ_r, and F are the Young modulus, thickness, Poisson ratio, displacement, density, residual stress of the diaphragm, and the resultant force per unit area acting on the diaphragm, respectively.

The magnitude and the direction of the force depend on the magnitude and the direction of the source of electrical current. The mechanism can be scaled down to nanoscale, which are classified as Nano-electrostatic drive (NED) actuators. The modality of the actuation relies on the elements periodically vibrating and providing a lateral force to bend the cantilever [107] (figure

24).

In electrostatic actuators, miniaturization is one of the most challenging issues. In order to make a fully integrated microsystem, the actuating parts must be placed inside a microchip [110]. Hsieh et al. [111] fabricated a circulatory micropump with 25 cm microcolumns and a working pressure of roughly 5.5 kPa. Although electrostatic actuators have a short delay in response and a considerably large volume change during the actuating process, there is still a need to moderate/reduce the operating voltage [112].

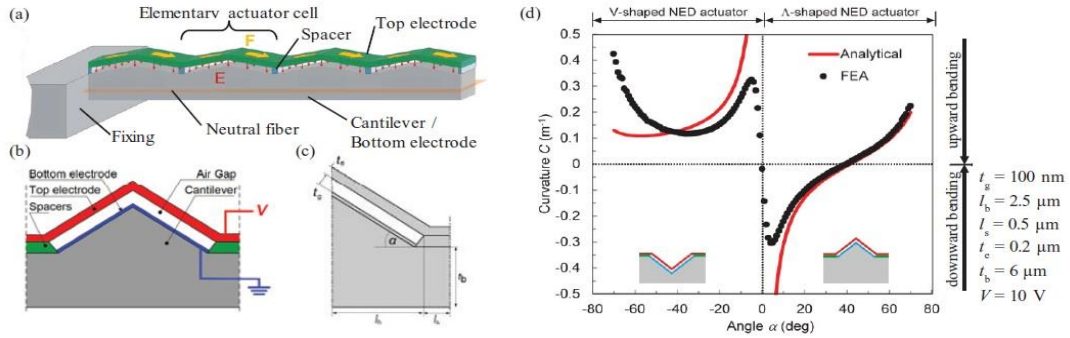

Figure 24 Schematic representation of NED actuators (a) schematic drawing of the whole bending and Λ-shaped actuator with electrostatic field E and transferred forces F highlighted, (b) schematic image of a single elementary actuator cell, (c) illustration of a half elementary actuator cell and the fundamental geometric parameters, (d) the controlled change in V- and Λ-shaped NED actuator curvature C as a function of the topography angle α. [12]

Dielectric elastomer actuator (DEA) is another approach utilizing electrostatic force when two elastomer membranes are charged by a relatively high alternating voltage (such as a sinusoidal wave) [113]. DEA can be categorized as an electroactive polymer, which has been studied in micropumps due to a large deformation with a small magnitude of voltage excitation.

Ionic polymer-metal composite (IPMC) and ionic conductive film (ICPF) are considered two common composite membranes in electroactive polymer applications. Figure [25] shows the working principle of an IPMC actuator, which bends bi-directionally by an alternating current. The

reason for deflection is an ionic movement caused by an external voltage, makes it different with

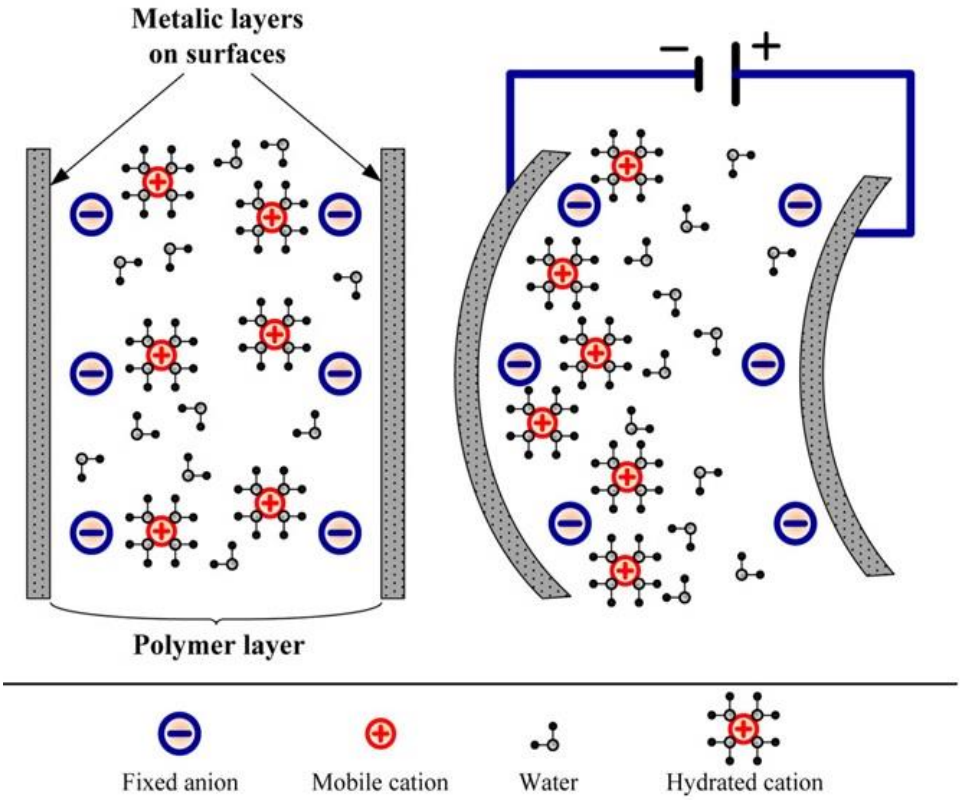

Figure 25 The concept of an IPMC during a working period [2]

other electrical actuation methods [2]. With IPMC having a reasonable performance underwater, it can be used in bio-inspired underwater robots [114]. Because of this ability, investigations have been performed to simulate and optimize the deflection and nonlinearity of the actuator [115]. Esmaeli et al. [116] tried to develop and optimize a new method for IPMC-based humidity sensors in wet environments. Better adhesion of the electrode layers to the polymers was the primary goal of their project. Ionic electroactive polymers (IEAPAs) have the ability to be fabricated and used in an LOC system. Meis et al. [117] introduced a proof-of-concept device that produced a transverse direction across the microchannel in an aqueous solution.

The challenge of the project was the protection of the electrodes in solution. The IEAPAs

have various advantages over the other microfabrication processes of electroactive polymers, such as simple processes, quick responses of electrodes, high flexibilities of the membranes, and low operating voltages [117].

Pumps with electroactive polymers, such as ionic polymer-metal composite (IPMC), have the advantage of low-level voltage requirements when compared to other actuating methods. These pumps can achieve large deformation when activated. Although they work best in dry conditions, they can still work in humid environments [116]. That having been said, the humidity in the environment affects the performance of IPMC in a nonlinear fashion, making them difficult to model. The fabrication process is also relatively complicated, and yet it is required to bond the layers of IPMC perfectly [116]. The other disadvantage of IPMC actuators is that it is difficult to geometrically form IPMC in a specific mechanical element such as a diaphragm. Additionally, IPMC performance is adversely affected by ionic concentration diffusion and electrolysis [2].

3. Electromagnetic Actuation

Lorentz Force law: Review

The magnetic flux density at an arbitrary point P from an element of length $\overrightarrow{dl}$, which is a part of wire carrying a steady current I, can be illustrated by the following formula:

$$\overrightarrow{d\boldsymbol{B}} = k\frac{I\overrightarrow{d\boldsymbol{l}} \times \overrightarrow{\boldsymbol{u}_R}}{\left|\overrightarrow{\boldsymbol{R}}\right|^2}, \qquad \text{Eq. (68)}$$

where $\overrightarrow{d\boldsymbol{B}}$ is the differential magnetic flux density in tesla (T), $\overrightarrow{d\boldsymbol{l}}$ is the differential length in the direction of current I, *k* is the constant of proportionality, and $\overrightarrow{\boldsymbol{u}_R}$ is the unit vector $\overrightarrow{\boldsymbol{u}_R} = \frac{\vec{\boldsymbol{R}}}{|\vec{\boldsymbol{R}}|}$; moreover, *k* can be defined as:

$$k = \frac{\mu_0}{4\pi}\ ,$$ Eq. (69)

where μ_0 is the free space permeability. Therefore, we can rewrite the formula representing the magnetic flux as:

$$\overrightarrow{d\boldsymbol{B}} = \frac{\mu_0 I \overrightarrow{d\boldsymbol{l}} \times \vec{\boldsymbol{R}}}{4\pi \left|\vec{\boldsymbol{R}}\right|^3}$$ Eq. (70)

After integration:

$$\vec{\boldsymbol{B}} = \frac{\mu_0}{4\pi} \oint_c \frac{I \overrightarrow{d\boldsymbol{l}} \times \vec{\boldsymbol{R}}}{\left|\vec{\boldsymbol{R}}\right|^3}$$ Eq. (71)

Thus $\vec{\boldsymbol{B}}$ is defined as magnetic flux density at point P due to a wire carrying steady current I. Moreover, the direction of $\vec{\boldsymbol{B}}$ is perpendicular to the plane containing $\overrightarrow{d\boldsymbol{l}}$ and $\vec{\boldsymbol{R}}$.

Suppose we have two interacting, current-carrying elements $I_1\overrightarrow{d\boldsymbol{l_1}}$ and $I_2\overrightarrow{d\boldsymbol{l_2}}$, the differential magnetic force exerted by element 1 upon element 2 is:

$$d\overrightarrow{\boldsymbol{F_2}} = \frac{\mu_0 I_2 d\overrightarrow{\boldsymbol{l_2}}}{4\pi} \times \left[\frac{I_1 d\overrightarrow{\boldsymbol{l_1}} \times \overrightarrow{\boldsymbol{R_{21}}}}{\left|\overrightarrow{\boldsymbol{R_{21}}}\right|^3}\right]$$ Eq. (72)

Considering the equation 5, we have:

$$d\overrightarrow{\boldsymbol{F_2}} = I_2 d\overrightarrow{\boldsymbol{l_2}} \times \overrightarrow{\boldsymbol{B_1}}$$ Eq. (73)

And after integration:

$$\overrightarrow{\boldsymbol{F_2}} = \oint_{c_2} I_2 d\overrightarrow{\boldsymbol{l_2}} \times \overrightarrow{\boldsymbol{B_1}}\ ,$$ Eq. (74)

where $\overrightarrow{\boldsymbol{B_1}}$ is the magnetic flux density produced by the current-carrying conductor 1 at the location of the current-carrying element $I_2 d\overrightarrow{\boldsymbol{l_2}}$ of the conductor 2, which is given by the following formula:

$$\overrightarrow{\boldsymbol{B_1}} = \frac{\mu_0}{4\pi} \oint_c \frac{I_1 \overrightarrow{d\boldsymbol{l_1}} \times \overrightarrow{\boldsymbol{R_{21}}}}{\left|\overrightarrow{\boldsymbol{R_{21}}}\right|^3} \quad \text{Eq. (75)}$$

This formula can be applied generally for any current-carrying conductor, which is placed in an external magnetic field $\vec{\boldsymbol{B}}$. Therefore, the magnetic force can be represented in general form:

$$d\overrightarrow{\boldsymbol{F}} = I\, d\vec{\boldsymbol{l}} \times \overrightarrow{\boldsymbol{B}} \quad \text{Eq. (76)}$$

And after integration:

$$\overrightarrow{\boldsymbol{F}} = \oint_c I\, d\vec{\boldsymbol{l}} \times \overrightarrow{\boldsymbol{B}} \quad \text{Eq. (77)}$$

This is called the Lorentz force law (or Ampere`s law), which for magneto hydrodynamic (MHD) actuators, can be represented in terms of current density *J*:

$$\overrightarrow{\boldsymbol{F}} = \oint_c J_v \times \overrightarrow{\boldsymbol{B}}\, dv \quad \text{Eq. (78)}$$

Because the current *I* is constant along the conductor and wire, the final form of the formula is:

$$\left|d\overrightarrow{\boldsymbol{F}}\right| = Idl\left|\overrightarrow{\boldsymbol{B}}\right| \sin(\emptyset)\,, \quad \text{Eq. (79)}$$

where Φ is the angle between the direction of wire (or conductor) carrying the current and the direction of the magnetic field, *B*. If the conductor or the wire is entirely located on a plane, which has the angle Φ with the magnetic field *B*, the angle is constant; thus, we have the final formula after integration:

$$\left|\overrightarrow{\boldsymbol{F}}\right| = IL\left|\overrightarrow{\boldsymbol{B}}\right| \sin(\emptyset), \quad \text{Eq. (80)}$$

where *L* is the total length of the wire or conductor. If the current is alternating and represented by a sinusoidal function, $\boldsymbol{I} = |\boldsymbol{I}|e^{j\omega t}$, where *j* is the imaginary unit ($j = \sqrt{-1}$). The reason behind choosing the complex form is that the mathematical operations are simpler, and the real part of the function is the final answer. Therefore, the direction of the magnetic force *F* is dependent on time,

and the frequency of the current is the frequency of the force.

A conductor or a wire carrying an electrical current induces a magnetic field around the wire based on the Lenz law. The polarity of this magnetic field can make an interaction with the polarity of other permanent magnets or solenoids; thus, it causes an attractive or repulsive force providing a reciprocating movement of a plunger or oscillation of a flexible diaphragm in micropumps (figure 26) [8].

A micropump with a 3-axis slider carrying an electromagnetic plunger can asymmetrically

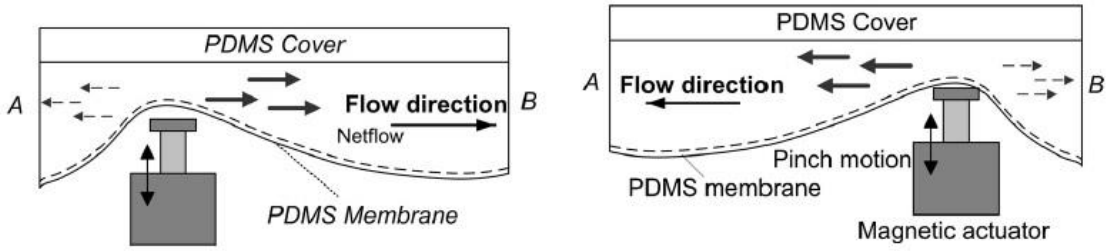

Figure 26 Reciprocating plunger [5].

deflect a PDMS membrane [8, 118, 119]. The maximum pressure around the pinched area was simulated around 0.2 Pa, and the maximum volumetric flow rate was +1.52 mL/min in the forward and -1.48 mL/min in the backward direction over the driving frequency range of 5-55 Hz. Another modular micropump with an electromagnetic plunger pinching a thin PDMS membrane was presented by Pei Song et al. [5] (figure 27). A downward push of the plunger creates a net pressure directing the fluid inside the chamber into the outlet port. The supplying mode of the pump happens when the plunger goes up, and the membrane returns to rest; therefore, the cycle of the rest and compression modes provide the required net pressure.

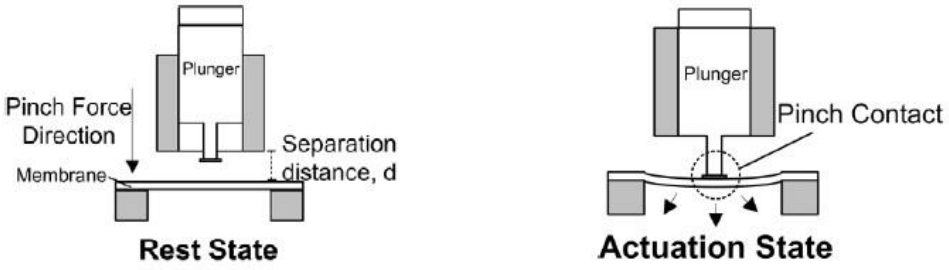

Figure 27 Utilizing a plunger pushing a flexible membrane [5].

The motion of two permanent magnets (NdFeB) inside an annular tube housing is another mechanism for actuating system [6, 120, 121] (figure 28), which acting such as a piston pushing forward the fluid inside the tube to the outlet valve. The mechanism needs a travelling alternating current, which causes the magnetic polarities around the coil. Those magnetic polarities cause the movement of the permanent magnet inside the tube. This micropump does not need check valves nor nozzle/diffuser arrangement in the inlets and outlets.

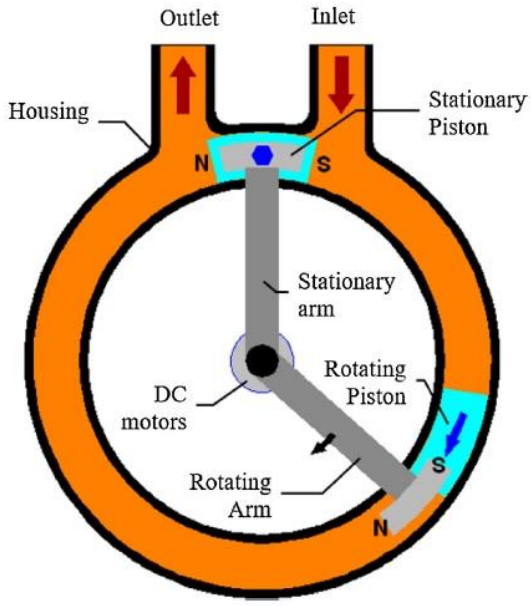

Figure 28 . The idea of a rotating membrane [6].

Another mechanism for electromagnetic actuators is a vibrating diaphragm actuated by an electromagnetic force generated due to the Lorentz force law. Muzalifa et al. [122] tried to actuate a membrane by including NdFeB magnetic particles with a magnetic field created by an electromagnetic coil. The actuator was embedded in a valveless micropump, where the flow rate was 2.3-6.6 × 10^{-6} L/min and supported by roughly 230-500 mA of input current. This design provides an out-of-plane Lorentz force and an in-plane magneto-static force [123]. Utilizing permanent pieces of magnets inside a PDMS membrane can create perfect vibrations as a result of a fixed coil carrying an alternating current [124, 125].

Chang et al. [126] utilized a new design including some permanent pieces of magnets embedded inside a flexible PDMS membrane, while a micro coil in another side was able to vibrate the PDMS membrane. Chen et al. [127] and Feng et al. [128] have a similar actuating system with a valveless design enabling a large stroke volume of transferred fluid. An analysis by [129] shows that there is a proportional relationship between the deflection of the membrane and the current of the micro coil. Wang et al. [129] reported that they could find the maximum deflection of the membrane (45 μm) when the current was 0.35 A.

The papers that extensively focused on the optimization of the actuator`s efficiency represented their results by FEM simulations, experimental validations, or vector potential current method [130]. Feustel et al. [131] represented the basic equations for the numerical simulation of an electromagnetic force created by a planar coil affected by a permanent magnetic field based on the Lorentz force law. Chun et al. [132] simulated the movement of a planar coil in an electromagnetic field creating a vertical force moving the membrane. They could represent the vertical force as a function of parameters such as the volume of the magnetic block, the distance between the planar coil and the magnetic block, and the cross section of the coil. Lee et al. [133] could fabricate a small actuator with overall dimension of 26 mm × 19 mm × 4.5 mm and volume

flow rate of 7.5 mL/min at an actuating frequency of 200 Hz. Beyzavi et al. [134] numerically modeled a PDMS diaphragm similarly actuated by an electromagnetic field and validated the results via experimental samples. Moreover, they analyzed the effect of parameters such as: gap size between wires of micro coils, number of wire turns, and the magnitude of electrical current on the final electromagnetic force. They concluded that decreasing the wire gap had the greatest effect on the final force.

In conclusion, Electromagnetic (EM) actuation is one of the most prevalent methods which mostly provides a reciprocating movement of diaphragm or membrane [133, 135] or a solenoid plunger [118, 136]. Quick responses, large displacements, and low actuation voltages are just some of the advantages of EM systems [137]. Since in these pumps, the membranes or diaphragms are mostly made of polydimethylsiloxane (PDMS), they can be flexible and demonstrate great toughness. The PDMS membranes and diaphragms can also be formed as a transparent thin membrane (<20 μm) [137, 138]. However, a highly complicated process is needed to prepare each PDMS layer and perfectly bond them to each other in order to have a fully uniform and continuous final product [93].

4. Magneto-hydrodynamic (MHD) Micropumps

Magnetohydrodynamic (MHD) micropumps have been developed recently, do not have mechanically moving parts, and do not need high actuating voltages. Moreover, they can provide a continuous and considerable net flow [139-141]. The main mechanism of the actuating part is the Lorentz force law; a non-magnetic electrically conducting fluid is carrying current in the presence of a permanent magnetic field [139, 142]. Due to their working principles, MHD pumps are mostly suitable to pump hot, ionized gases (plasmas), liquid metals, and electrolytes [142].

Nevertheless, Karmozdi et al [140, 143] fabricated MHD micropumps by making a liquid metal droplet move in a reciprocating fashion, acting as a reciprocating piston to pump fluids. This design can be used in microscale, however, since the pumped fluid is in contact with liquid metal, it is not the best choice for biomedical applications. Using liquid metal droplets as an actuator has also been utilized to pump NaOH electrolytes [144, 145].

The effect of the laminar fluid flow on heat convection has been extensively studied in recent papers. The movement of electrically conductive particles by the force induced by a magnetic field can pump a fluid flow in a tube and transfer the heat from an inlet to an outlet. Malvandi and Ganji [146] tried to have a convective heat transfer system with a laminar fluid flow of a mixed Al_2O_3-water nanofluid. The model was a homogeneous mixture of nanoparticles floating in a water flow. Shekholeslami and Elahi [147] had another simulation of a convective nanofluid to show the change of Rayleigh number in consistence with the Nusselt number. Other similar papers have investigated micropolar fluids [148], quasi-two-dimensional magneto-hydrodynamic flows [149], and the non-Newtonian flows [150].

There are other mechanisms used for movement of liquid metal in pumps. These mechanisms include: surface tension [151], electrochemical [152], and electroosmotic [153]. The drawback of these pumps is that the liquid metal has direct contact with the working fluid. As such, they are not peristaltic micropumps to be used in biomedical applications. A brief summarization of the main advantages and disadvantages can be found in Table 3.

The goal of this research is to design a simple, yet effective mechanism in macroscale that can be scaled down to microscale. The novelty of this dissertation is the creation of a flexible, valveless pump with a plethora of desired design criteria such as an easy fabrication process, low operational voltage, peristaltic design, miniaturization feasibility, and biological safety. The designed actuator utilizes Lorentz force law to create the needed pressure difference.

Table 3. The advantages and disdavantages of the actoutors. The summary of actuators including the performances, advantages, disadvantages, and applications.

Actuation Method	Advantages	Diadvantages
Lead Zirconate Titanate (PZT)	Most Common Method, Actuating a Flexible Diaphragm,	High Actuating Voltage, Limited Stroke [90]
Electrostatic Actuators	Short Delay in Response, High Volume rate [118]	High Challenge in Miniaturization [124]
Electroactive Polymers (such as ionic polymer-metal composite IPMC)	Low Level Voltage, Large Deformation [93]	Adversely Effect of Humidity, Nonlinear Behavior, Complicated Fabrication Process, Difficulty in Geometrical Formation [93, 110]
Electromagnetic Actuation (EM)	Providing a Reciprocating Movement of a Flexible Membrane or Solenoid Plunger, Quick Response, Large Displacement, Low Level Voltage [2, 112, 116]	Highly Complicated Process in the Fabrication and bonding process of polydimethylsiloxane (PDMS) membranes [90]
Magnetohydrodynamic (MHD) Actuators	Non-moving parts, Low Level Actuating Voltage, providing a continuous and considerable net flow [118, 133, 135, 136], Simple Actuating Mechanism (Lorentz Force Law)	Not Applicable for Any Fluids (Just hot ionized gases (plasmas), liquid metals and electrolytes), Not Applicable for Biological Fluids [136]
Liquid metal droplets	Miniaturization, Good Performance in Microscales, [93, 122, 138-140], Simple Actuating Mechanism (Lorentz Force Law)	Not Peristaltic, Not Applicable for Biological Fluids, Highly Precise Fabrication Process Method, Low Efficiency

5.. Valveless Micropumps

Predominantly, check valves are the solution in pump structures. They can easily switch in order to avoid any back-flow in the pumps. Thus, the mechanical efficiency of check-valve pumps is effectively at the maximum theoretical value. However, the performance of check valves is critical because a perfect synchronized control system is needed to control the micro valves. Moreover, the mechanical microvalves may damage or smash the biological cells during the switch process, or they may be clogged when the cells accumulate around the inlet or outlet. In addition, the fabrication of micro-check valves is not easy even with a 3D printer method. Because these valves should always completely switch from the open to the closed position, they should have the capacity to withstand considerable fatigue stresses in one cycle operation. Finally, fixing or replacing damaged valves is not easy in micro scale, and the performance of the pump effectively depends entirely upon the functional ability of micro valves. Therefore, valveless micropumps are preferred in biological application. However, it is important to note that the net pressure and mechanical efficiency of the pump is considerably less than its check valve counterparts.

Calculation of the efficiency and the net pressure of the valveless micropumps is described by Olsen et al. [3]. They formulated the theory based on the nozzle/diffuser shape, geometry, and the effect of Reynolds number in the final net flow, volume ratio, and the efficiency of the micropumps. A single chamber model is shown in figure 29. Equations 81 calculate the pressure drop across the nozzle or diffuser.

$$\Delta P_d = \frac{\rho {v_d}^2}{2} \zeta_d \qquad \text{Eq. (81a)}$$

$$\Delta P_n = \frac{\rho {v_n}^2}{2} \zeta_n \qquad \text{Eq. (81b)}$$

where ρ is the density, v_n and v_d are the velocities of flow in the narrowest part of nozzle and

diffuser, respectively. Similarly, ζ_n and ζ_d are the pressure loss coefficients in nozzle and diffuser.

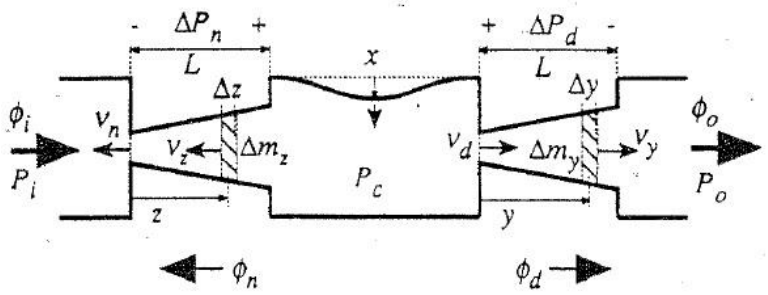

Figure 29 The model of single chamber diffuser/nozzle pump. The model of a nonreciprocal arrangement of a nozzle/diffuser set [3]

The diaphragm oscillates such as a sinusoidal function; therefore, the function is

$$V_c = V_o sin\omega t \qquad \text{Eq. (82)}$$

$$V_c = K_v x_o \qquad \text{Eq. (83)}$$

We can calculate the volume flow of the nozzle and diffuser (Φ_n and Φ_d) by Eq. 84 [154]:

$$\emptyset_d = A_d v_d \;\; \& \;\; \emptyset_n = A_n v_n \,, \qquad \text{Eq. (84)}$$

where A_n and A_d are the cross-sectional areas of the narrowest parts of nozzle and diffuser. So, the volume flow formulas can be modified:

$$\emptyset_d = A_d \left(\frac{2}{\rho}\right)^{1/2} \left(\frac{\Delta P_d}{\zeta_d}\right)^{1/2} \qquad \text{Eq. (85a)}$$

$$\emptyset_n = A_n \left(\frac{2}{\rho}\right)^{1/2} \left(\frac{\Delta P_n}{\zeta_n}\right)^{1/2} \qquad \text{Eq. (85b)}$$

$$\emptyset_d = \frac{C}{{\zeta_d}^{1/2}} \quad \text{Eq. (86a)}$$

$$\emptyset_n = \frac{C}{{\zeta_n}^{1/2}} \quad \text{Eq. (86b)}$$

$$C = A\left(\frac{2P_c}{\rho}\right)^{1/2} \quad \text{Eq. (87)}$$

where P_c is the chamber pressure. So the net volume Φ is [3]:

$$\emptyset = \phi_o - \phi_i = \frac{dV_c}{dt} = V_o cos\omega t \quad \text{Eq. (88)}$$

After integration we will have:

$$\emptyset = \frac{V_0\omega}{\pi}\left(\frac{\eta^{1/2}-1}{\eta^{1/2}+1}\right) = \frac{K_v x_o \omega}{\pi}\left(\frac{\eta^{1/2}-1}{\eta^{1/2}+1}\right) \quad \text{Eq. (89)}$$

where $\eta = \zeta_n / \zeta_d$ is the loss of pressure ratio coefficient of both the nozzle and diffuser. The nominator of Eq. 88 indicates that η should be more than 1 (η>1) if we have positive net volume rate from the inlet to the outlet. Moreover, the maximum efficiency of the net volume rate occurs when η is maximum. Therefore, the maximum flow rate in nozzles and diffusers is:

$$\emptyset_{d\,max} = \eta^{1/2}\emptyset_{n\,max} = V_0\omega\left(\frac{\eta^{1/2}}{\eta^{1/2}+1}\right) = \pi\left(\frac{\eta^{1/2}}{\eta^{1/2}-1}\right)\phi \quad \text{Eq. (90)}$$

We can calculate the approximate expression for maximum pressure across a diffuser/nozzle element during a pump cycle:

$$\Delta P_{d/n\,max} = \frac{\rho\zeta_n\omega^2{V_0}^2}{2{A_d}^2(\eta^{1/2}+1)} = \frac{\rho\zeta_n\pi^2}{2{A_d}^2(\eta^{1/2}-1)}\Phi^2 \quad \text{Eq. (91)}$$

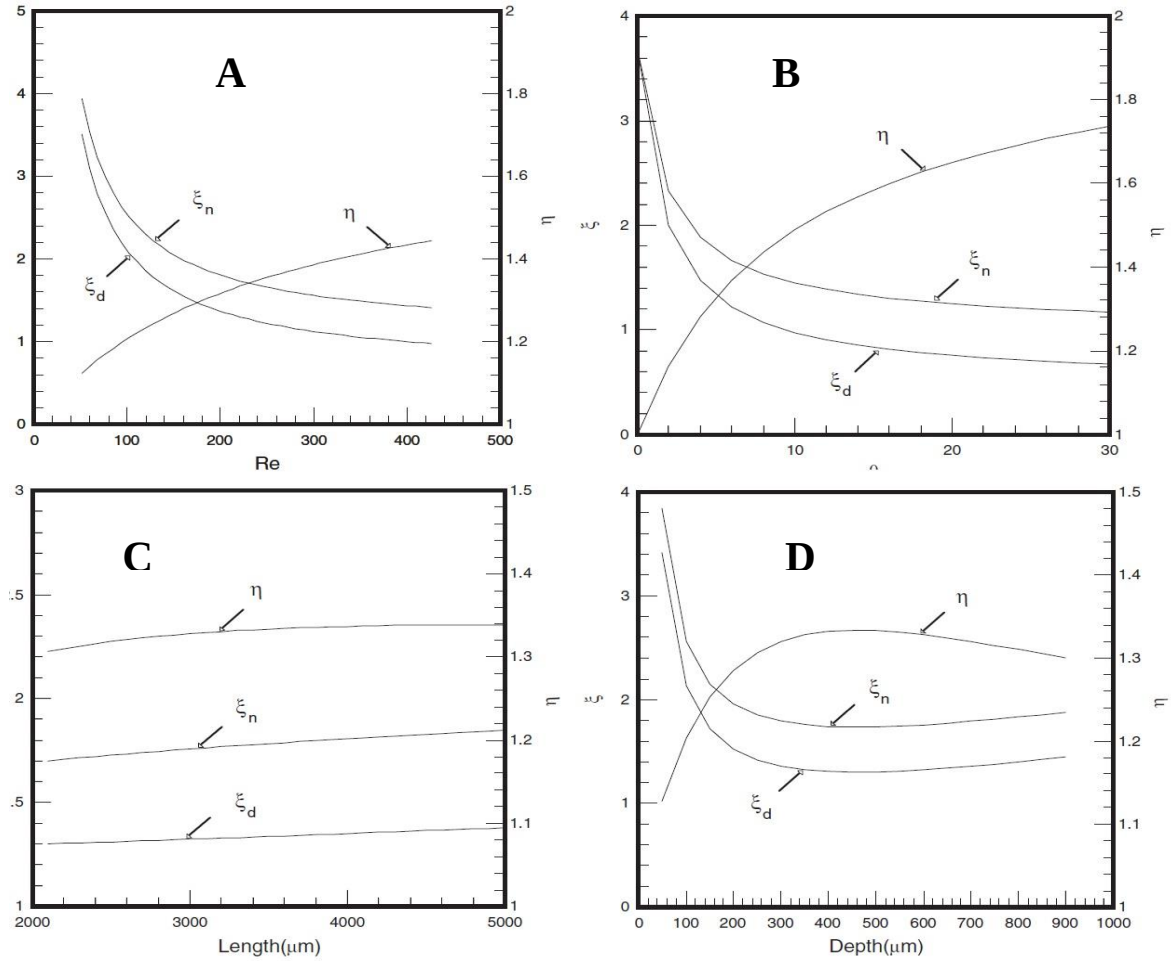

Figure 30 The figures illustrating the pressure loss coefficient. A) Pressure loss coefficient versus Reynolds. B) Pressure loss versus opening angle C) Pressure loss coefficient versus nozzle/diffuser length D) Pressure loss coefficient versus nozzle/diff depth [11]

Thus, we can conclude that when $\eta>1$, a diffuser/nozzle element can act as asymmetric element which allows a net flow from inlet to outlet. Nevertheless, calculation of the maximum η is required. Yang et al. [11, 155] determined how much the geometry and Reynolds number affect η. The results are shown in the figure 30 [11].

In conclusion, when Reynolds number is maximum with the highest opening angles η, the maximum efficiency of the micropump is expected. Nonetheless, the opening angle is limited due

to flow separation occurring on the inner walls. Lee and Yang et al [156-158] used the same arrangement of the nozzle/diffuser pump.

6. Double Chamber Micropump

A one-chamber valveless micropump can be optimized if more chambers are added up to enhance the overall efficiency. There have been new investigations utilizing micro-particle velocimetry (PIV) to monitor the performance of liquid/blood-sucking insects such as mosquitos and butterflies [4, 10, 156, 159, 160]. It has been shown by the PIV that mosquitos have a double chamber blood sucking system, including a cibarial pump (CP) and pharyngeal pump (PP). (Figure

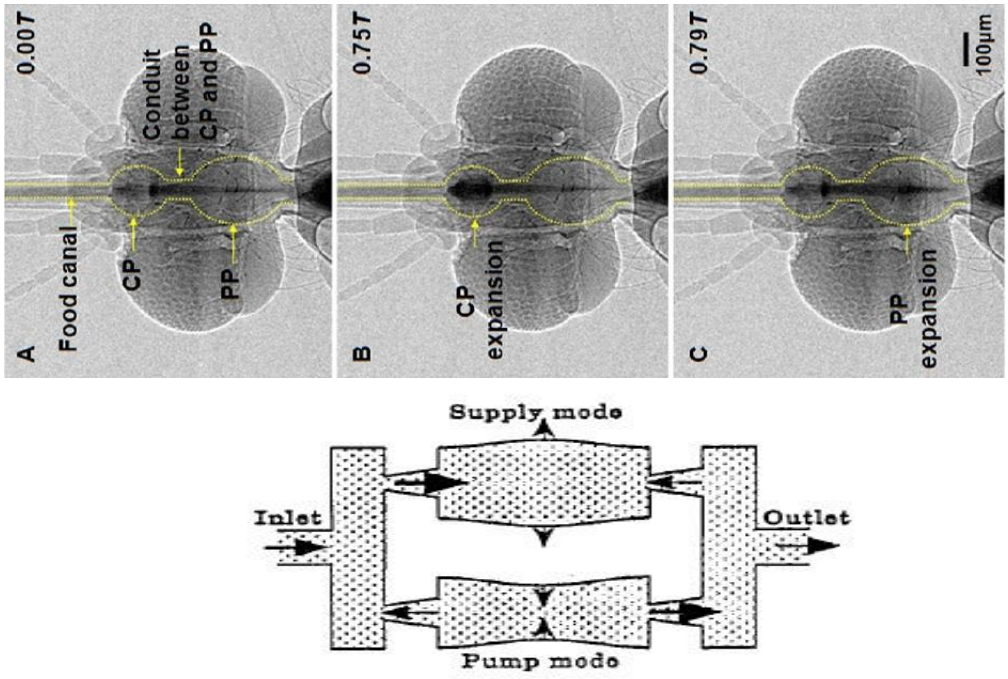

Figure 31 Bloodsucking system of mosquitos. Top: The process of sucking blood in female mosquitos, which proving a continuous flow rate compared to a single chamber system. where T is time period of one cycle pumping where 0.00T denotes the start point and 1.00T is the complete of one period [10]. Bottom: A schematic of a double chamber dipolar out of phase pump [3].

31)

Kikuchi et al [159] introduced a mathematical model in order to simulate the double

chamber mechanism (Figure32). Lee et al [156] concluded that the maximum performance of the double chamber system happens when the phase difference between the CP and PP is 180^0 (dipole out of phase system). Moreover, the performance of a serially connected valveless micropump is the summation of the performance of each single chamber working alone [3, 161-164]. Therefore, a double chamber micropump is considered for this project in order to be consistent with the bio-inspired applications. However, a FEM simulation is required in order to determine the overall dimension of the pump having the most optimum efficiency.

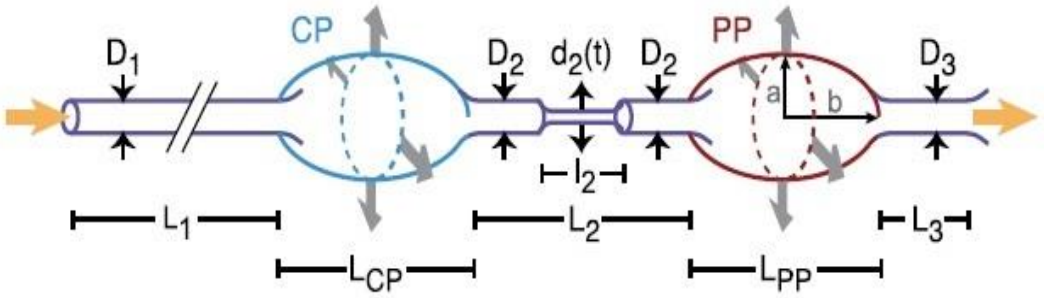

Figure 32 Model of double chamber system. Schematic of the model for the simulation of double chamber mosquitos blood-sucking organ [4].

CHAPTER VI

MICROPUMP WITH LIQUID METAL

This dissertation creates unique value through its novel idea of utilizing a valveless micropump with a liquid metal actuator. The idea of nonreciprocity involves a valveless micropump working with an asymmetrical nozzle and diffuser in both the inlet and outlet. Although there have been a multitude of research efforts concentrating on the performance and efficiency of the nozzle and diffuser arrangement, the optimum micropump geometry has yet to be determined. The compatibility of the micropump with an acceptable efficiency is important; however, the main concern is that the final design is consistent with an LOC system. On the other hand, introducing a new design or a novel system should meet the requirements of the working conditions and the mechanical efficiencies expected from a typical micropump in a lab or medical environment.

Therefore, a simulation showing the general performance of a valveless micropump is performed in this project. The main goal of this simulation is to determine the size of a micropump that will result in an appropriate head pressure. Additionally, the analysis of the mechanical performance of the micropump in a range of working frequencies with different boundary conditions can also be represented by this simulation. At the end, an experimental test is required in order to validate the simulation results. The following sections of this dissertation are designed to depict how a nonreciprocal arrangement of a nozzle/diffuser set can provide a net pressure in a fluid flow.

1. Definition of the problem

The problem revolves around the fact that a valveless micropump creates a net pressure between the inlet and outlet. The micropump can be modeled as a 2-dimensional component transferring fluid (water as an incompressible fluid) from inlet to outlet. The governing equations for this problem are the continuity equation (equation 92) and Navier stokes equation (equation 93). The general form of these equations for an incompressible Newtonian (linear) fluid are:

$$\nabla.\left(\vec{\boldsymbol{V}}\right) = 0 \qquad \text{Eq. (92)}$$

$$\rho\frac{D\vec{\boldsymbol{V}}}{\partial t} = -\nabla \mathrm{p} + \rho\vec{\boldsymbol{g}} + \mu\nabla^2\left(\vec{\boldsymbol{V}}\right) \qquad \text{Eq. (93)}$$

where $\vec{\boldsymbol{V}}$ is the velocity vector, ρ is density, $\vec{\boldsymbol{g}}$ is the bulk force (such as gravity), p is pressure, μ is dynamic viscosity, and $\frac{D}{\partial t}$ is the material derivative ($\frac{D\vec{\boldsymbol{V}}}{\partial t} = \frac{\partial\vec{\boldsymbol{V}}}{\partial t} + \vec{\boldsymbol{V}}.\nabla(\vec{\boldsymbol{V}})$.

These equations can be modified for a planner 2-dimensional problem ($\vec{\boldsymbol{g}} = 0$). Moreover, suppose that the components of the velocity field in a 2-dimensional field are shown as

$$\vec{\boldsymbol{V}} = u_1\vec{\boldsymbol{\imath}} + u_2\vec{\boldsymbol{\jmath}} \qquad \text{Eq. (94)}$$

Where $\vec{\boldsymbol{\imath}}$ and $\vec{\boldsymbol{\jmath}}$ are the unit vectors in the x and y directions, respectively. Therefore, we can have the governing equations in cartesian coordinate:

$$\frac{\partial u_1}{\partial x} + \frac{\partial u_2}{\partial y} = 0 \qquad \text{Eq. (95a)}$$

$$\rho\left(\frac{\partial u_1}{\partial t} + u_1\frac{\partial u_1}{\partial x} + u_2\frac{\partial u_1}{\partial y}\right) = -\frac{\partial p}{\partial x} + \mu\left(\frac{\partial^2 u_1}{\partial x^2} + \frac{\partial^2 u_1}{\partial y^2}\right) \qquad \text{Eq. (95b)}$$

$$\rho\left(\frac{\partial u_2}{\partial t}+u_1\frac{\partial u_2}{\partial x}+u_2\frac{\partial u_2}{\partial y}\right)=-\frac{\partial p}{\partial y}+\mu\left(\frac{\partial^2 u_2}{\partial x^2}+\frac{\partial^2 u_2}{\partial y^2}\right) \quad \text{Eq. (95c)}$$

In polar coordinate, the velocity vector is

$$\vec{\boldsymbol{V}}=u_r\vec{\boldsymbol{e}}_{\boldsymbol{r}}+u_\theta\vec{\boldsymbol{e}}_{\boldsymbol{\theta}}, \quad \text{Eq. (96)}$$

where $\vec{\boldsymbol{e}}_{\boldsymbol{r}}$ and $\vec{\boldsymbol{e}}_{\boldsymbol{\theta}}$ are the unit vectors in the r and θ directions, respectively. Thus, the governing equations have the following form in polar coordinate:

$$\frac{1}{r}\frac{\partial(ru_r)}{\partial r}+\frac{1}{r}\frac{\partial u_\theta}{\partial\theta}=0 \quad \text{Eq. (97a)}$$

$$\rho\left(\frac{\partial u_r}{\partial t}+u_r\frac{\partial u_r}{\partial r}+\frac{u_\theta}{r}\frac{\partial u_r}{\partial\theta}-\frac{{u_\theta}^2}{r}\right)$$
$$=-\frac{\partial p}{\partial r}+\mu\left(\frac{1}{r}\frac{\partial}{\partial r}\left(r\frac{\partial u_r}{\partial r}\right)-\frac{u_r}{r^2}+\frac{1}{r^2}\frac{\partial^2 u_r}{\partial\theta^2}-\frac{2}{r^2}\frac{\partial u_\theta}{\partial\theta}\right) \quad \text{Eq. (97b)}$$

$$\rho\left(\frac{\partial u_\theta}{\partial t}+u_r\frac{\partial u_\theta}{\partial r}+\frac{u_\theta}{r}\frac{\partial u_\theta}{\partial\theta}-\frac{u_r u_\theta}{r}\right)$$
$$=-\frac{1}{r}\frac{\partial p}{\partial\theta}+\mu\left(\frac{1}{r}\frac{\partial}{\partial r}\left(r\frac{\partial u_\theta}{\partial r}\right)-\frac{u_\theta}{r^2}+\frac{1}{r^2}\frac{\partial^2 u_\theta}{\partial\theta^2}+\frac{2}{r^2}\frac{\partial u_r}{\partial\theta}\right) \quad \text{Eq. (97c)}$$

2. Boundary Conditions

The primary aim of the simulation is to determine the boundary conditions. An obstacle in that determination is that the components of velocity (u_1 and u_2) and pressure, p, are the variables appearing in the equations; nevertheless, they are not independent from each other. Therefore, we need to define the boundary conditions where the relationship between the pressure and velocity is analytically known. Thus, we can introduce the following model which identifies the

relationship between the pressure and velocity. There are two boundaries that are required to be defined in order to be in consistence with the physics of the micropump.

wall

The first boundary condition is wall. Equation 98 shows the gradient of the pressure and velocities in an ideal wall.

$$\frac{\partial p}{\partial n} = 0 \quad \& \quad u_1 = u_2 = 0\,, \qquad \text{Eq. (98)}$$

where n is in the normal direction to the wall. Based on equation 96, we have a Dirichlet boundary condition for velocity ($u_1 = u_2 = 0$), and Neumann boundary condition for pressure ($\frac{\partial p}{\partial n} = 0$).

source

In the real micropump, the actuator pushes or sucks the water by a flexible membrane in the z direction. Because we need to have a 2-dimensional mathematical model, the best way to model the actuator is to use a source with an axisymmetric boundary condition. Equation 6 can be used in polar coordinate when the $u_\theta = 0$. Moreover, because of symmetricity, the velocity should be unchanged in the circumference of the source ($\frac{\partial}{\partial \theta} = 0$). Therefore, the equations 97 can be rewritten as:

$$\frac{1}{r}\frac{\partial (r u_r)}{\partial r} = 0 \qquad \text{Eq. (99a)}$$

$$\rho\left(\frac{\partial u_r}{\partial t} + u_r \frac{\partial u_r}{\partial r}\right) = -\frac{\partial p}{\partial r} + \mu\left(\frac{1}{r}\frac{\partial}{\partial r}\left(r\frac{\partial u_r}{\partial r}\right) - \frac{u_r}{r^2}\right) \qquad \text{Eq. (99b)}$$

$$-\frac{1}{r}\frac{\partial p}{\partial \theta} = 0 \qquad \text{Eq. (99c)}$$

Equation 99a concludes that $u_r = \frac{Const.}{r}$. Moreover, equation 99c shows that the pressure is symmetric around the source ($p = f(r)$). If we put $u_r = \frac{Const.}{r}$ in the equation 99b, we can find the pressure function. The actuator of the pump can then be modeled as a sinusoidal function of time due to the reciprocating movement of the silicone rubber membrane. We can suggest the following formula for the velocity around the source:

$$\vec{\boldsymbol{V}} = u_r \vec{\boldsymbol{e}}_{\boldsymbol{r}} = \frac{K}{r} e^{j\omega t} \vec{\boldsymbol{e}}_{\boldsymbol{r}} \,, \qquad \text{Eq. (100)}$$

where K is a constant number and j is imaginary. We can rewrite the equation 8b:

$$j\omega u_r = \frac{d}{dr}\left(-\frac{1}{2}({u_r}^2) - \frac{1}{2}\rho p + \frac{\mu}{\rho}\left(\frac{u_r}{r} + \frac{du_r}{dr}\right)\right) \qquad \text{Eq. (101)}$$

If we have an integral around the circumference of the source, then we have:

$$j\omega \oint_c u_r . dr \; = \frac{d}{dr}\left(-\frac{1}{2}({u_r}^2) - \frac{1}{2}\rho p + \frac{\mu}{\rho}\left(\frac{u_r}{r} + \frac{du_r}{dr}\right)\right) \qquad \text{Eq. (102)}$$

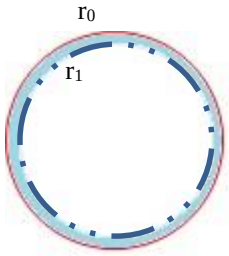

Figure 33 Geometry model of the source. The red line is the circumference of the source. r0 is the radius of the source circle, and r1 is the radius of the inner circle when r0= r1+ε (which ε is an exceedingly small number).

We can define a very thin band around the source and use the stokes theorem for the left

side of equation 102. Because the source is axisymmetric, we can conclude that vorticity is zero in the blue area in figure 2, and because the u_r is analytical in this area we can use the stokes theorem.

$$j\omega \oint_{\boldsymbol{\Omega}} \vec{\boldsymbol{V}}.d\vec{\boldsymbol{r}} = \iint (\boldsymbol{\nabla} \times \vec{\boldsymbol{V}}).\vec{\boldsymbol{n}}dA = 0, \qquad \text{Eq. (103)}$$

where $\boldsymbol{\Omega}$ is the boundary of the blue area shown in figure 33. The right side of equation 103 is zero and if we put the equation 100 in the equation 102 we have:

$$p = -\frac{\rho}{2}\frac{K^2}{r^2}e^{2j\omega t} \qquad \text{Eq. (104)}$$

3. Vorticity and Stream function model

Because the gradient of pressure appears in the governing formulas, we can use the two variables, vorticity and stream function, from the governing equations in a 2-dimensional incompressible fluid flow. Because both vorticity and stream function are completely defined based on velocity, finding the pressure in consistence with the velocity is not necessary. If we define the vorticity and stream function based on the equations 105:

$$\xi = \frac{1}{2}\left(\frac{\partial u_2}{\partial x} - \frac{\partial u_1}{\partial y}\right), \qquad \text{Eq. (105a)}$$

$$\frac{\partial \psi}{\partial y} = -u_x \quad \& \quad \frac{\partial \psi}{\partial x} = u_y\ , \qquad \text{Eq. (105b)}$$

where ψ is the stream function, and ξ is vorticity. If we have $\frac{\partial}{\partial x}(Eq.95c) - \frac{\partial}{\partial y}(Eq.95b)$ including the Eq. 95a, the final equations will be:

$$\frac{\mu}{\rho}(\nabla^2\xi) + \frac{\partial\psi}{\partial x}\frac{\partial\xi}{\partial y} - \frac{\partial\psi}{\partial y}\frac{\partial\psi}{\partial x} - \frac{\partial\xi}{\partial t} = 0 \qquad \text{Eq. (106a)}$$

$$-\frac{1}{2}\left(\frac{\partial^2\psi}{\partial x^2} + \frac{\partial^2\psi}{\partial y^2}\right) = \xi \qquad \text{Eq. (104b)}$$

Boundary conditions

Wall

In an ideal wall, both the gradient of pressure and the velocity are zero. So we have:

$$\frac{\partial\psi}{\partial x} = \frac{\partial\psi}{\partial y} = \frac{\partial\psi}{\partial n} = 0 \quad \& \quad \xi = 0 \qquad \text{Eq. (107)}$$

Thus, there is a Dirichlet boundary condition for ξ, and Neumann boundary condition for ψ.

Source

If the source is circular with an axisymmetric flow, the vorticity is zero and the stream function can easily be found from velocity without needing to know the pressure.

$$\frac{\partial\psi}{\partial y} = -u_x \quad \& \quad \frac{\partial\psi}{\partial x} = u_y \quad \& \quad \xi = 0 \qquad \text{Eq. (108)}$$

4. Simulation in COMSOL

COMSOL Multiphysics is a powerful computational software for the project's analytical needs . The software has an option for laminar fluid flow which works well for the simulation

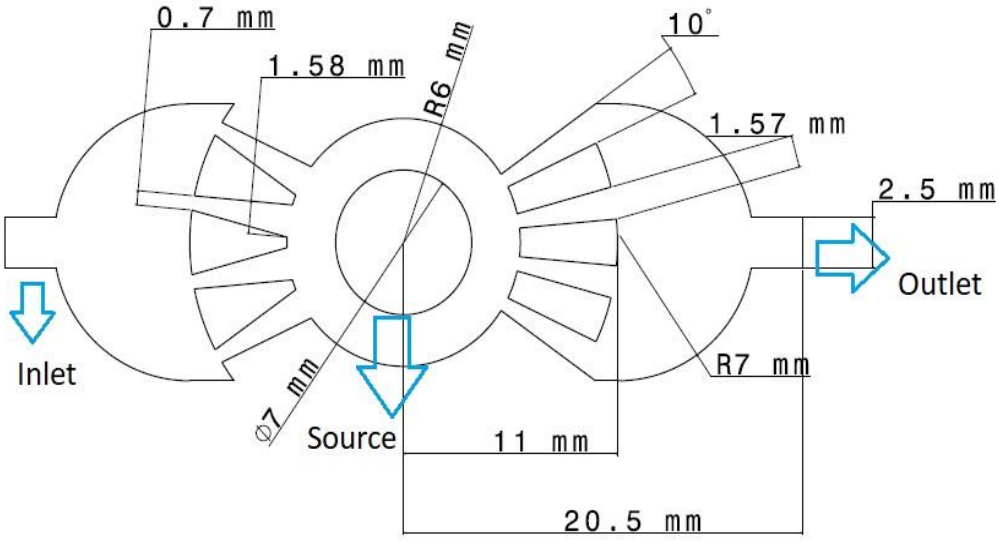

Figure 34 The model of the pump. The imported 2-dimensional model of the real pump in COMSOL

required in this project. Figure 34 represents a 2-dimensional illustration of a micropump model. The source part provides an axisymmetric sinusoidal force along the z direction, whereas the inlet and the outlet ports of the micropump are modeled as two outputs with constant pressures. This is the model of one chamber, whereas the real pump is a double chamber. The governing equations are the Navier Stokes as well as the continuity equations described in the previous section. In this model, we can assume that there is one input which is the circular axisymmetric source providing a constant radius velocity, and two outputs which are the inlet and the outlet of the real pump.

The first obstacle to overcome is that the Reynolds number should always be less than 2300. Thus, we need to find a range of magnitudes of input velocity in consistence with the range of the Reynolds number. If we write down the conservation of mass formula for the input and the outputs, we have:

$$\dot{m}_{pump} = \dot{m}_{inlet} + \dot{m}_{outlet} \,, \qquad \text{Eq. (109)}$$

where the $\dot{m}_{pump}$ is the mass ratio of the circular pressure area, $\dot{m}_{inlet}$ and $\dot{m}_{outlet}$ are the mass ratios of the inlet and the outlet in the real pump, respectively. Because the water is an incompressible fluid circulating in the real pump, and the cross-sectional areas in the inlet and outlet are same. Thus, we will have:

$$\rho\left|\overrightarrow{\boldsymbol{V}_{pump}}\right|A_{pump} = \rho\left|\overrightarrow{\boldsymbol{V}_{inlet}}\right|A_{inlet} + \rho\left|\overrightarrow{\boldsymbol{V}_{outlet}}\right|A_{outlet} \quad \text{Eq. (110a)}$$

$$\left|\overrightarrow{\boldsymbol{V}_0}\right|A_{pump} = 2\left|\overrightarrow{\boldsymbol{V}_{out}}\right|A_{out}\,, \quad \text{Eq. (110b)}$$

where $\left|\overrightarrow{\boldsymbol{V}_0}\right|$ is the initial velocity. Because of symmetricity, we can consider that the magnitude of the velocities in the inlet and outlet are same. We can write the same formula for the relationship between the velocities in the nozzles and the velocity in the output.

$$\rho\left|\overrightarrow{\boldsymbol{V}_{outlet}}\right|A_{outlet} = \rho\left|\overrightarrow{\boldsymbol{V}_{nozzles}}\right|A_{nozzles} \quad \text{Eq. (111a)}$$

$$\left|\overrightarrow{\boldsymbol{V}_{outlet}}\right|A_{outlet} = 4\left|\overrightarrow{\boldsymbol{V}_{nozzle}}\right|A_{nozzle} \quad \text{Eq. (111b)}$$

Equations 111 show that if there are 4 nozzles (instead of one nozzle), it guarantees that the Reynolds number does not exceed the laminar limit; moreover, less energy loss as well as a higher volume ratio are the other advantages. The thickness of the model is considered 1 mm, where the channel of the fluid flow is rectangular. The hydraulic diameter for a rectangular duct with the thickness, t, and the width, a, in order to calculate the Reynolds number is:

$$D_H = \frac{2at}{a+t} \quad \text{Eq. (112a)}$$

$$Re = \frac{\rho V D_H}{\mu}\,, \quad \text{Eq. (112b)}$$

where μ is the dynamic viscosity, V is the velocity average in the cross-section area, and D_H is the hydraulic diameter. Table 4 is the summary of all Reynolds numbers in the critical sectional areas. Therefore, the range between 0.02 and 0.2 m/s for the initial velocity can guarantee that the

Reynolds number is less than 2300 and that the fluid flow is always laminar.

Table 4. The Reynolds number for all the critical cross-sectional areas

$\lvert\overrightarrow{V_0}\rvert$ [m/s]	$\lvert\overrightarrow{V_{inlet}}\rvert$ [m/s]	$\lvert\overrightarrow{V_{nozzles}}\rvert$ [m/s]		Dh [mm]			Re		
		Narrow side	Wide side	Narrow side	Wide side	inlet/outlet	Narrow side	Wide side	inlet/outlet
0.02	0.09	0.08	0.04	0.82	1.22	1.43	72.64	48.05	141.12
0.08	0.35	0.31	0.14	0.82	1.22	1.43	290.55	192.19	564.49
0.14	0.62	0.55	0.25	0.82	1.22	1.43	508.46	336.34	987.87
0.20	0.88	0.79	0.35	0.82	1.22	1.43	726.37	480.48	1411.24

5. Boundary Condition in COMSOL

The source of the pump in the model creates an axisymmetric velocity which alternates sinusoidally by time. The suggested formula is:

$$\vec{\boldsymbol{V}}_{(\vec{\boldsymbol{X}},t)} = \vec{\boldsymbol{V}}_{(\vec{\boldsymbol{X}})} e^{j\omega t} \qquad \text{Eq. (113)}$$

where ω is the frequency of the actuator and $\vec{\boldsymbol{V}}_{(\vec{\boldsymbol{X}})}$ is the steady state velocity vector which is completely separated from the time function.

$$\vec{\boldsymbol{V}}_{(\vec{\boldsymbol{X}})} = u_1\vec{\boldsymbol{\imath}} + u_2\vec{\boldsymbol{\jmath}}\,, \qquad \text{Eq. (114)}$$

where i and j are the unite vector along the x and y direction, respectively.

Figure 35 displays a simple micropump with one nozzle/diffuser set. This model has a horizontal symmetric line from the inlet to the outlet. If we rewrite the Navier Stokes along this line, we know that the velocity does not have a vertical component through the line due to symmetricity (u_2=0). Therefore, the equations 95 are:

$$\frac{\partial u_1}{\partial x} = 0 \qquad \text{Eq. (115a)}$$

$$\rho\left(u_1 \frac{\partial u_1}{\partial x}\right) = -\frac{\partial p}{\partial x} + \mu\left(\frac{\partial^2 u_1}{\partial x^2}\right) \qquad \text{Eq. (115b)}$$

$$\frac{\partial p}{\partial y} = 0 \qquad \text{Eq. (113c)}$$

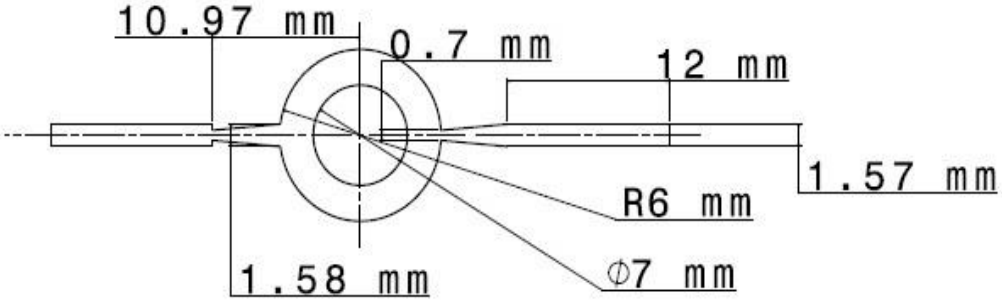

Figure 35 Geometry of the model. The test model with 1 nozzle/diffuser set

The equation 115a concludes that $\frac{\partial^2 u_1}{\partial x^2} = 0$. And the equation 115c shows that the pressure is not the function of y component along the symmetric line. If we rewrite the equation 115b we will have:

$$\rho\left(u_1 \frac{\partial u_1}{\partial x}\right) + \frac{\partial p}{\partial x} = 0 \qquad \text{Eq. (116a)}$$

$$\frac{d}{dx}\left(\frac{{u_1}^2}{2g} + \frac{p}{\rho g}\right) = 0 \quad \Rightarrow \quad \frac{{u_1}^2}{2g} + \frac{p}{\rho g} = Const. \qquad \text{Eq. (116b)}$$

The equation 116b is the Bernoulli equation which is only true along the symmetric line. Nevertheless, the constant number in the right hand of the line (outlet) is different from the left side (inlet) due to the source area in the middle of the line. However, we can write the formula for the inlet side (B to A) and the outlet side (B' to C) (figure 36).

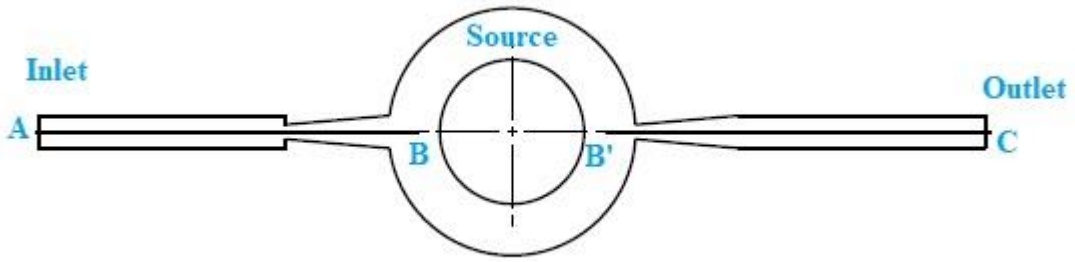

Figure 36 The four points on the center line. The two lines (AB & B'C) along the center line

$$\frac{{U_B}^2-{U_A}^2}{2g}+\frac{p_B-p_A}{\rho g}=0 \quad \& \quad \frac{{U_C}^2-{U_{B'}}^2}{2g}+\frac{p_C-p_{B'}}{\rho g}=0\,, \qquad \text{Eq. (117)}$$

where the U_A and U_C are the velocities of inlet and outlet on the symmetric line, respectively. Because B and B' are markedly close to the source (0.5 mm distance), the Bernoulli equation is valid; thus, the effect of the source happens in the constant numbers of each line (equation 117). Because the source is located in the middle of the centerline, the constant number in the left side (K_1) is different from the right one (K_2).

$$\frac{{U_A}^2}{2g}+\frac{p_A}{\rho g}=\frac{{U_B}^2}{2g}+\frac{p_B}{\rho g}=K_1 \;\&\; \frac{{U_{\acute{B}}}^2}{2g}+\frac{p_{\acute{B}}}{\rho g}=\frac{{U_C}^2}{2g}+\frac{p_C}{\rho g}=K_1 \qquad \text{Eq. (118)}$$

The equations 118 show that there is not any reciprocity even in the points B and B' which are remarkably close to the source. Nonetheless, we need to know the head of the pump in order to apply it in the boundary conditions.

$$\frac{{U_A}^2}{2g} + \frac{p_A}{\rho g} = \frac{{U_C}^2}{2g} + \frac{p_C}{\rho g} + \Delta h \,, \qquad \text{Eq. (119)}$$

where the Δh in the right side of equation 119 is the pump head that we need to calculate. However, knowing the pressures in the inlet or outlet is required for the boundary conditions. Thus, guessing the head of the pump can be performed via a trial-and-error process. Firstly, we can assume that the head of the pump appears in the term of an extra pressure in outlet (Equation 120).

$$\frac{{U_A}^2}{2g} + \frac{p_A}{\rho g} = \frac{{U_C}^2}{2g} + \frac{\acute{p}_C}{\rho g} \qquad where\ \frac{\acute{p}_C}{\rho g} = \frac{p_C}{\rho g} + \Delta h \qquad \text{Eq. (120)}$$

The equation 120 can be rewritten as:

$$\frac{{U_B}^2 - {U_{\acute{B}}}^2}{2g} + \frac{p_B - p_{\acute{B}}}{\rho g} = K_1 - K_2 = \delta \,, \qquad \text{Eq. (121)}$$

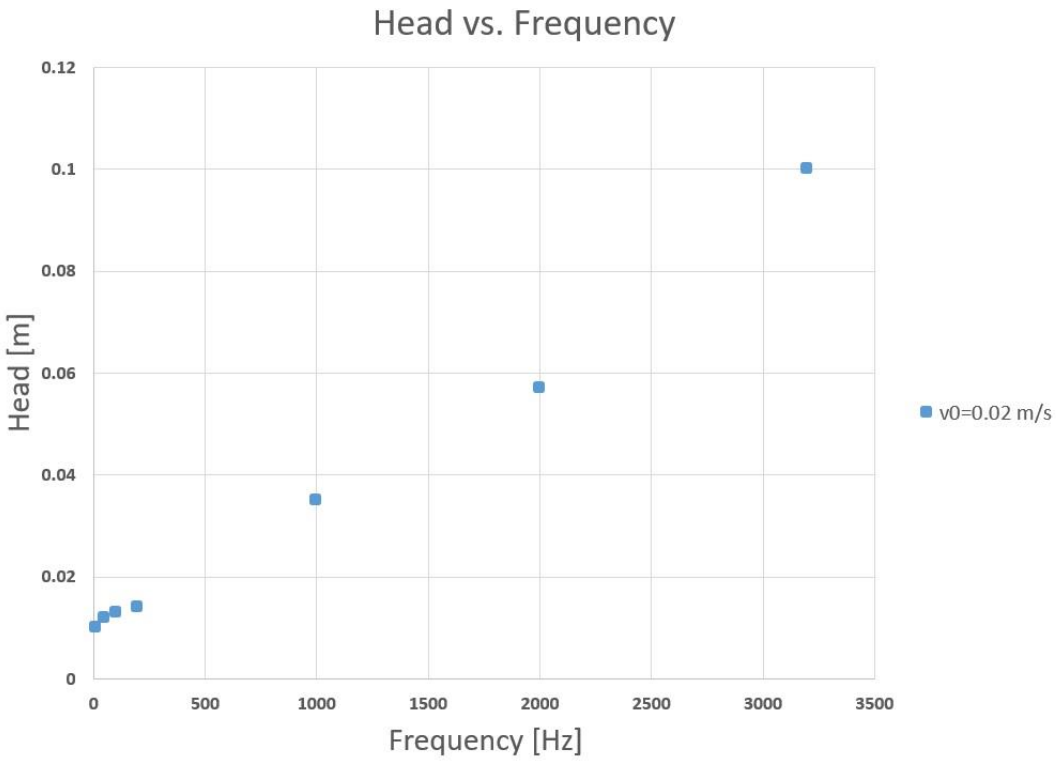

Figure 37 One-nozzle/diffuser simulation results. Head of pump vs. frequency for the test model when the initial velocity is 0.02 m/s

where δ is the difference of the energy between the right side and the left side of the source. Because we have an axisymmetric source, the δ should be zero if and only if the pressures in the boundaries (equation 29) are chosen correctly. Therefore, we need to guess the Δh and consider it as the extra pressure in the outlet ($\acute{p}_C$). Computing the model by COMSOL, the resulting pressures and velocities at the points B and B' can be exported to an Excel file in order to calculate δ. The process repeats until the final calculated δ is (or considerably close to) zero. Figure 37 shows the results when the range of actuating frequency is between 10 to 3200 Hz, and the constant initial velocity is 0.02 m/s. The head of the pump should increase with frequencies [165].

The rise of pressure head happens when the frequency is between 100 and approximately 2000 Hz; thus, the optimum actuating frequency should be in this range. We can perform the same process for the real pump when it has 4 nozzles and 4 diffusers (figure 38). Therefore, we can

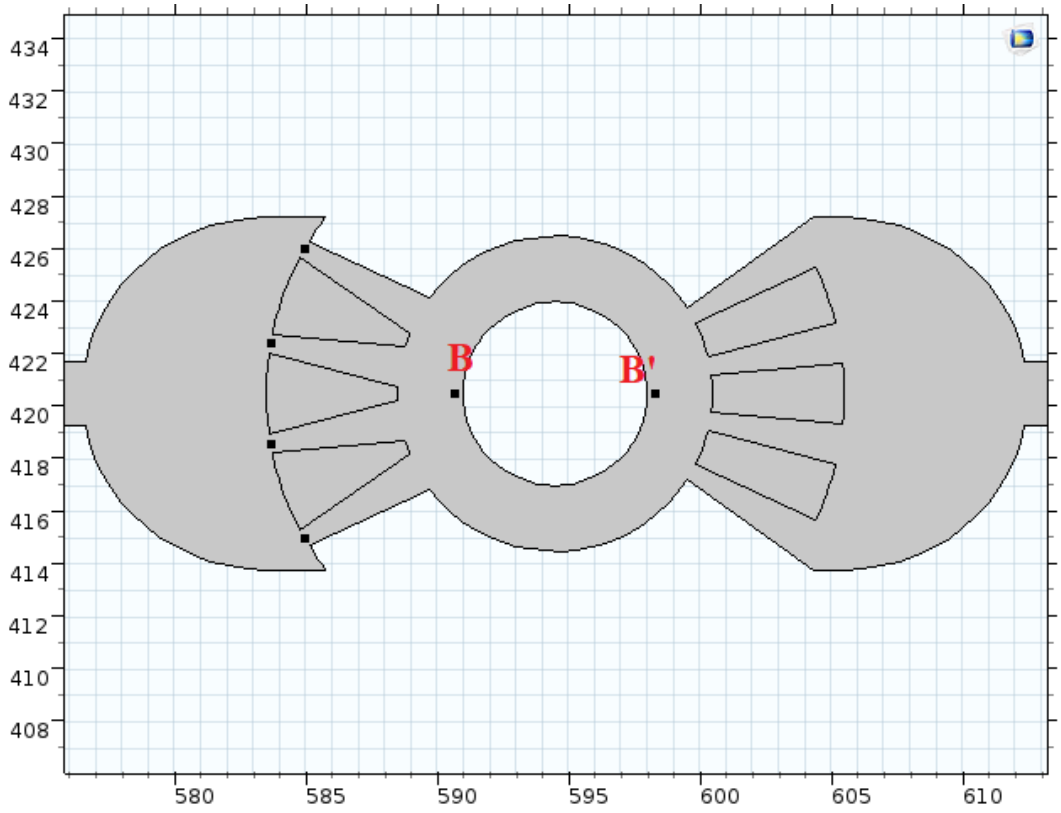

Figure 38 The model of the micropump in COMSOL. The points B and B' are located on the center line where they are 0.5 mm far from the source

similarly consider the B and B' near to source and change the pressure of the outlet in the boundary condition until the level of energy in both points B and B' becomes the same.

Figure 39 displays the results as a function of initial velocity and actuating frequencies. The results shows that there is a dramatic rise when the frequency is between 500 and 1500 Hz. On the other hand, the upward ratio of the figure decreases for the frequencies greater than 1500 Hz; therefore, the frequency has an optimum effect between 500-1500 Hz. The initial velocity generally increases the pump head because the more initial velocity means the more input energy to the system. The COMSOL model was scaled by a factor of 0.5 compared to the real size of the pump to decrease the computational expense/time. Additionally, a greater mesh concentration was applied to both the nozzle and diffuser parts.

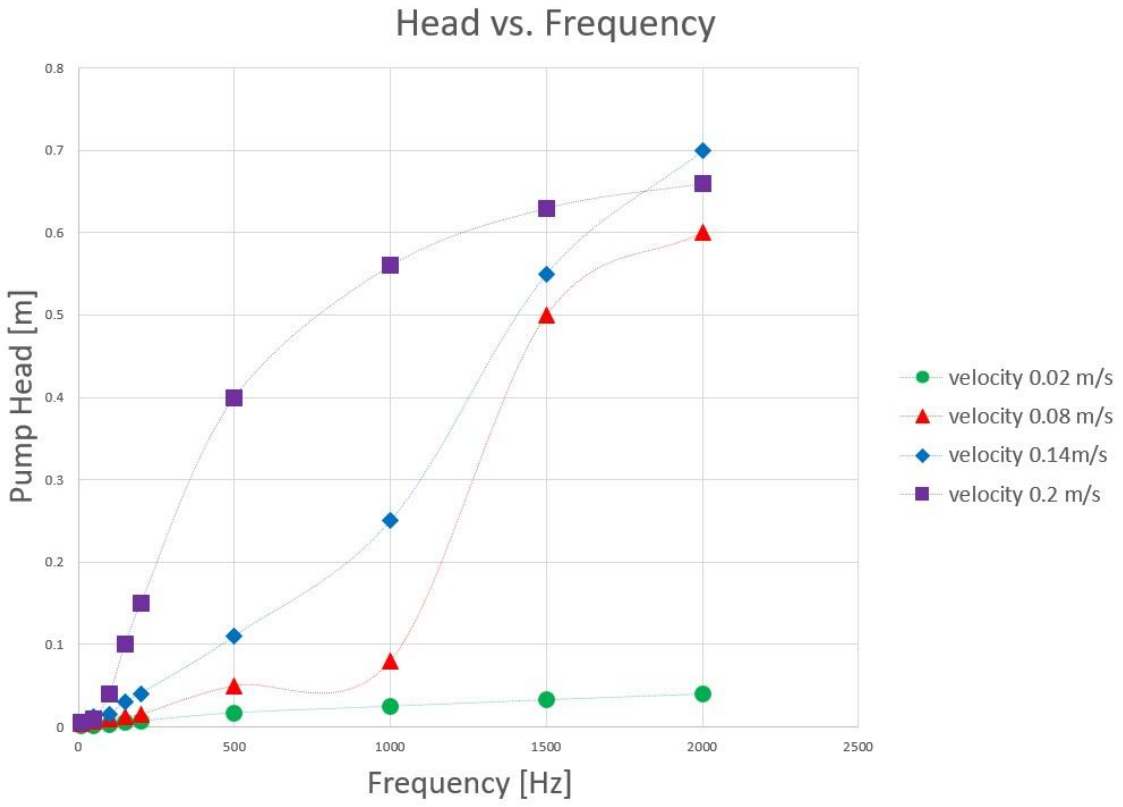

Figure 39 The results for different velocities and frequencies. The pump head vs. frequency in different initial velocity (0.02, 0.08, 0.14, 0.2 [m/s]. The optimum range is between 500-1500 Hz.

6. The experimental test

The goal was to design a simple, yet effective mechanism in macroscale that can be scaled down to microscale. In this work, we fabricated a novel, flexible, valveless pump that satisfied criteria ranging from having a simple fabrication process, to requiring low operational voltages, to being a peristaltic design, to being feasibly miniaturized, and being safe to use in biological applications. The actuator of this novel pump utilizes Lorentz force law to create the needed pressure difference in order to convey the fluid from inlet to the outlet port. In the following sections, we explain the fabrication process, experimental setup, and results.

The innermost part of the deigned pump is a bi-layer, flexible diaphragm made of silicone rubber. This diaphragm has a helical, narrow microchannel filled with liquid metal. This layer is sandwiched between two thicker layers that have a nozzle/diffuser. The diaphragm and the two layers of nozzle/diffuser are placed between two exterior covers made of glass and constrained by guiding pins. Two 3D printed PLA covers hold all the parts and have a connection to the inlet/outlet pipes. The inlet and outlet sections have access to the lateral part of the cylinder as shown in figure 41. In operation, the pump is held between two permanent magnets with a distance of about 24 mm. Since there are two magnets facing each other in opposing poles, the magnetic field is constant, uniform, and parallel to the axis of the cylinder (Z axis). The basis of operation is similar to our previous work where we used Lorentz force law to make a motor with radial motion [166]. Since the exciting current is sinusoidal (with frequency of ω), and is orthogonal to the magnetic field, the differential force is radial, and the magnitude of the differential force can be calculated by:

$$d\boldsymbol{F} = id\boldsymbol{l} \times \boldsymbol{B} \;\Rightarrow\; |\mathrm{d}\mathbf{F}| = i|\mathrm{d}\mathbf{L}||\mathbf{B}|\mathrm{Sin}(\omega t)\,, \qquad \text{Eq. (122)}$$

where $|\mathrm{d}\mathbf{F}|$ is the magnitude of differential radial force pointing inward or outward according to the direction of the current (Figure 42).

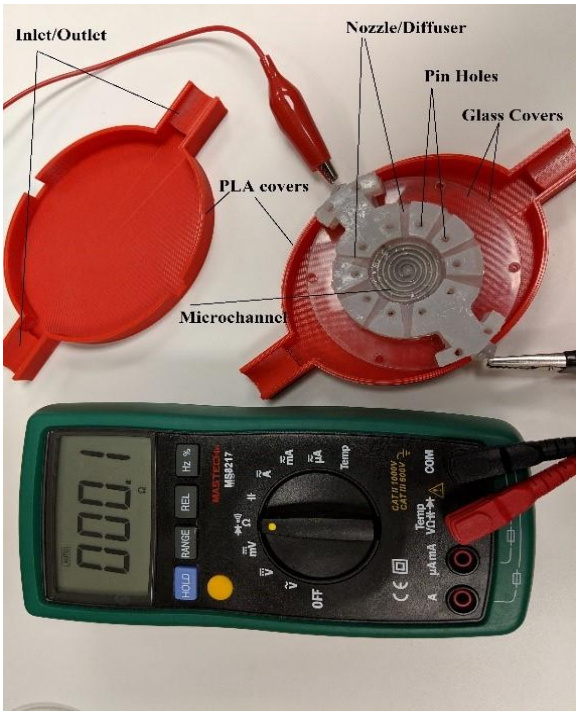

Figure 40 All sections of the pump. There is 0.1 Ω electrical resistance across the microchannel filled with Galinstan

As shown in figure 42a, there are two layers: one of which has a tensile (inward) force causing in-plane compression whereas the other layer experiences contraction due to outward radial force. As a result, an out of plane bending moment can manipulate the diaphragm into a downward or upward crown shape (figure 42b). Changing the direction of the current in a sinusoidal fashion, the diaphragm makes a reciprocating oscillation. This motion can be used in a biologically inspired double chamber pump [160, 167-170]. As a comparison, two PZT dipolar actuators should be used in order to vibrate two distinct diaphragms. The advantage of this

mechanism, however, is that we can make it in a flexible material. Also, it is possible to generate complex motion by changing the helix pattern, making the pattern not circular or with variable channel width.

7. Fabrication and Experimental Setup

Platinum-based Silicone rubber is used to construct the main parts of the pump including the diaphragm and nozzle/diffuser sections. Platinum-based silicone rubber had certain advantages for this work. It has an acceptable toughness, is highly stretchable, has a reasonably short curing process, and is a proper material for medical and food/drug production [171]. As suggested by Park et al [63], we used a heat lamp to expedite the curing process at 600 C. The cure process was completed in an hour. Each of the diaphragm layers were casted using 3D-printed molds. The

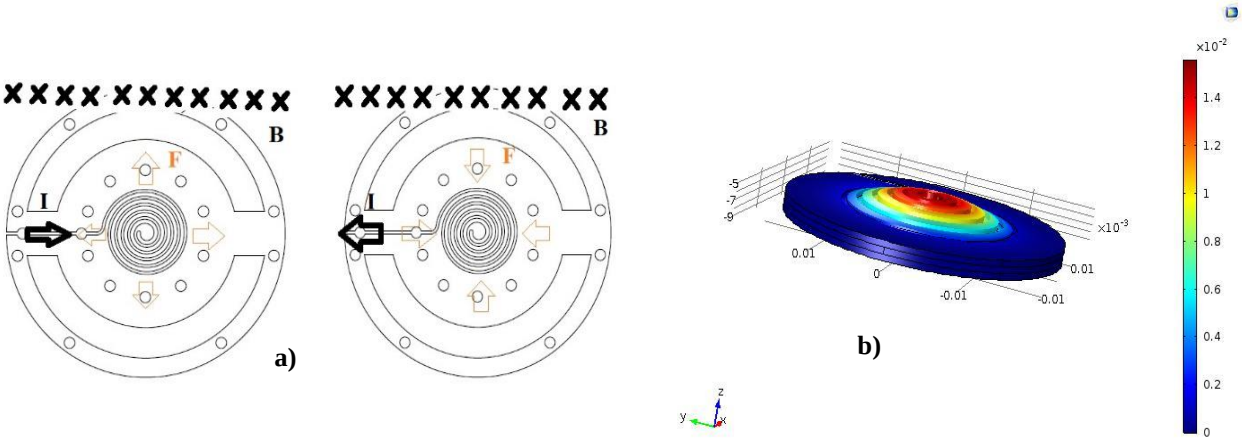

Figure 41 Simulation of the diaphragm deflection. a): inward and outward motion of the top and bottom layer of the diaphragm. Direction of the radial forces, depicted by orange arrows, depends on the current direction. b): The upward crown shape of diaphragm re

bonding process between layers was done by partial curing of each layer at 600 C for 2 minutes and then a complete curing of the diaphragm and nozzle/diffuser parts. The injection of the liquid metal Galinstan was performed using a syringe. The syringe filled with liquid metal was connected

to one side of the microchannel, and a vacuum system was connected to the other side of the channel. The vacuum pressure was provided by an off-the-shelf BAC-ENG vacuum system. The resistance of the microchannel was measured to be 0.1 Ω as shown in figure 41. Since in these prototypes, the connections between electrodes and the liquid metal might be affected by the vibration, we checked the connections by regularly measuring the resistance both before and after each experiment. The overall thickness of the diaphragm was 5 mm. The two nozzle/diffuser layers and two exterior glass covers added 10 and 6 mm to the thickness of the structure, respectively. These layers of diaphragms and inlet/outlet are encased in an exterior cover made of PLA which was constructed by a 3D printer.

The pump was placed between two permanent magnets which are separated by an adjustable mechanical device. The magnets were off-the-shelf 3×3×1 in. NdFeB Grade N52 permanent magnets provided by K&J. They were held in place by an aluminum structure and set to face each other in opposite poles. The magnetic field was almost uniform and was measured to be 0.3 T. The electrical circuits had a 6 Ω protective resistor in series with the pump in order to reduce the high load on the amplifier and make possible the measurement of current during the experiment. The actual setup is shown in figure 43.

8. Results and Discussions

The current frequency was varied from 1 Hz to 500 Hz, and it was observed that the pump resonant frequency was around 10 Hz. At this frequency, and with 3 Amps input current, the pressure difference between the inlet and outlet of the pump was measured to be around 1 cm of water (98.1 Pa). The maximum flow rate for the pipe (internal ID = 1 cm), based on the Bernoulli`s principle, can be calculated by:

$$Q_{max} = \pi R^2 \sqrt{\frac{2\Delta P}{\rho}}, \qquad \text{Eq. (123)}$$

where ΔP is pressure difference in Pa, ρ is the density (997 Kg/m3 for water) and R is the radius of the pipe (0.005 m). Thus, the maximum theoretical net flow rate is 34.8 mL/s. An attempt was made to determine the ultimate limit of loading by increasing the current to the highest level before pump failure. The ultimate tolerable current was roughly 4 A, and even then, only 40 seconds passed before failure. Since the resistance in the liquid metal is 0.1 Ω, even at high current, there is not much power consumed by the pump.

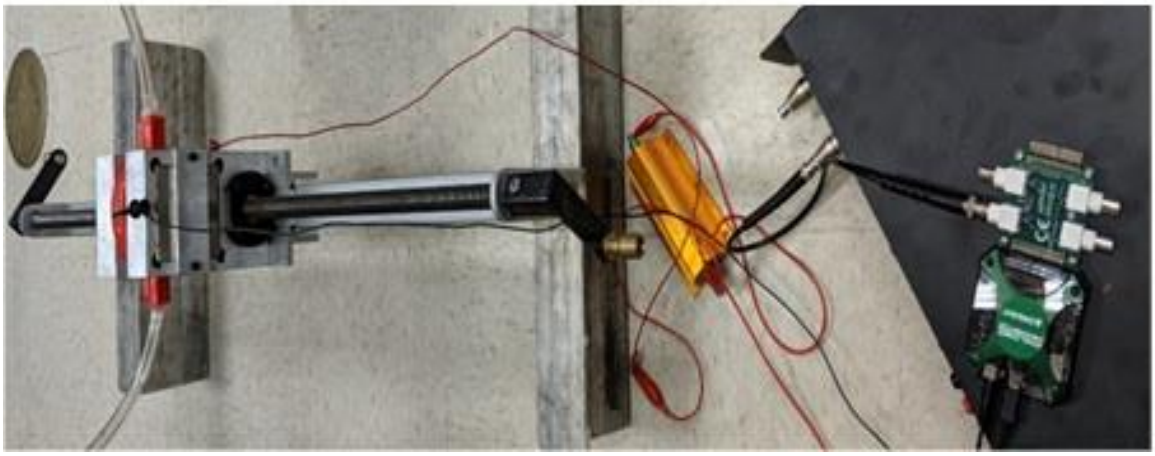

Figure 42 The top view of the experimental setup

In this project, a valveless, flexible pump was considered. The actuator modality involved a diaphragm with a microchannel filled with liquid metal Galinstan. The helical patterns of the microchannel could provide an out-of-plane bending resulting from inward/outward in-plane radial Lorentz force. In the prototype pump, the head was measured to be roughly 1 cm of water (98.1 Pa); therefore, the maximum theoretical volume ratio based on Bernoulli`s equation was about 34.8 mL/s.

This project demonstrates the feasibility of using a microchannel filled with liquid metal in a double chamber actuator design. This pump design is scalable and can be made for micro scale

applications. The actuator part including microchannel and diaphragm, excluding the nozzle/diffuser components, were made by flexible material. As such, this design can be made by silicone rubber in a uniform and integrated structure to make a pump which is flexible and stretchable. Utilizing other polymeric substrates with different microchannel dimensions may result in different performances which can be investigated in future works.

REFERENCES

LIST OF REFERENCES

[1] D. T. Blackstock, "Fundamentals of physical acoustics," ed: Acoustical Society of America, 2001.

[2] D. N. C. Nam and K. K. Ahn, "Design of an IPMC diaphragm for micropump application," *Sensors and Actuators A: Physical,* vol. 187, pp. 174-182, 2012.

[3] A. Olsson, G. Stemme, and E. Stemme, "A valve-less planar fluid pump with two pump chambers," *Sensors and Actuators A: Physical,* vol. 47, pp. 549-556, 1995.

[4] Y. R. Ha, J. H. Kim, J. Ryu, and S. J. Lee, "Superb feeding behavior of Aedes albopictus transmitting Zika virus," *Plos one,* vol. 12, p. e0184871, 2017.

[5] P. S. Chee, R. Arsat, T. Adam, U. Hashim, R. A. Rahim, and P. L. Leow, "Modular architecture of a non-contact pinch actuation micropump," *Sensors,* vol. 12, pp. 12572-12587, 2012.

[6] M. Kilani, H. Khasawneh, A. Badran, and A. Awidi, "Further development on a gentle electromagnetic pump for fluids with stress-sensitive microparticles," *Sensors and Actuators A: Physical,* vol. 247, pp. 440-447, 2016.

[7] R. Fleury, D. Sounas, M. R. Haberman, and A. Alù, "Nonreciprocal acoustics," *Acoustics Today,* vol. 11, pp. 14-21, 2015.

[8] P. S. Chee, R. A. Rahim, R. Arsat, U. Hashim, and P. L. Leow, "Bidirectional flow micropump based on dynamic rectification," *Sensors and Actuators A: Physical,* vol. 204, pp. 107-113, 2013.

[9] M. Fink, "Time-reversed acoustics," *Scientific American,* vol. 281, pp. 91-97, 1999.

[10] B. H. Kim, H. K. Kim, and S. J. Lee, "Experimental analysis of the blood-sucking mechanism of female mosquitoes," *Journal of Experimental Biology,* vol. 214, pp. 1163-1169, 2011.

[11] K.-S. Yang, Y. Chen, B.-Y. Shew, and C.-C. Wang, "Investigation of the flow characteristics within a micronozzle/diffuser," *Journal of Micromechanics and Microengineering,* vol. 14, p. 26, 2003.

[12] H. Conrad, B. Kaiser, M. Gaudet, S. Langa, M. Stolz, S. Uhlig, *et al.*, "A novel electrostatic actuator class," *Procedia Engineering,* vol. 168, pp. 1533-1536, 2016.

[13] W. A. Strauss, *Partial differential equations: An introduction*: John Wiley & Sons, 2007.

[14] H. v. Helmholtz, "Theorie der Luftschwingungen in Röhren mit offenen Enden," *Journal für die reine und angewandte Mathematik,* vol. 57, pp. 1-72, 1860.

[15] J. Strutt, "Some general theorems relating to vibrations," *Proceedings of the London Mathematical Society,* vol. 1, pp. 357-368, 1871.

[16] L. Lyamshev, "A question in connection with the principle of reciprocity in acoustics," in *Soviet Physics Doklady,* 1959, p. 406.

[17] L. D. Landau and E. M. Lifshitz, *Fluid mechanics* vol. 6: Elsevier, 1987.

[18] A. D. Pierce, *Acoustics: an introduction to its physical principles and applications*: Acoustical Society of America Melville, NY, 1991.

[19] O. A. Godin, "Reciprocity and energy theorems for waves in a compressible inhomogeneous moving fluid," *Wave Motion,* vol. 25, pp. 143-167, Mar 1997.

[20] O. A. Godin, "Reciprocity and energy conservation within the parabolic approximation," *Wave Motion,* vol. 29, pp. 175-194, Feb 1999.

[21] R. Fleury, D. L. Sounas, and A. Alù, "Subwavelength ultrasonic circulator based on spatiotemporal modulation," *Physical Review B,* vol. 91, p. 174306, 05/28/ 2015.

[22] R. Fleury, D. L. Sounas, C. F. Sieck, M. R. Haberman, and A. Alù, "Sound isolation and giant linear nonreciprocity in a compact acoustic circulator," *Science,* vol. 343, pp. 516-519, 2014.

[23] R. Fleury, A. B. Khanikaev, and A. Alù, "Floquet topological insulators for sound," vol. 7, p. 11744, 06/17/online 2016.

[24] A. B. Khanikaev, R. Fleury, S. H. Mousavi, and A. Alù, "Topologically robust sound propagation in an angular-momentum-biased graphene-like resonator lattice," *Nature communications,* vol. 6, 2015.

[25] L. E. Kinsler, A. R. Frey, A. B. Coppens, and J. V. Sanders, "Fundamentals of acoustics," *Fundamentals of Acoustics, 4th Edition, by Lawrence E. Kinsler, Austin R. Frey, Alan B. Coppens, James V. Sanders, pp. 560.*

ISBN 0-471-84789-5. Wiley-VCH, December 1999., p. 560, 1999.
[26] M. Fink, D. Cassereau, A. Derode, C. Prada, P. Roux, M. Tanter, *et al.*, "Time-reversed acoustics," *Reports on Progress in Physics,* vol. 63, pp. 1933-1995, Dec 2000.
[27] F. Arntzenius and H. Greaves, "Time Reversal in Classical Electromagnetism," *British Journal for the Philosophy of Science,* vol. 60, pp. 557-584, Sep 2009.
[28] M. Fink, "TIME-REVERSAL OF ULTRASONIC FIELDS .1. BASIC PRINCIPLES," *Ieee Transactions on Ultrasonics Ferroelectrics and Frequency Control,* vol. 39, pp. 555-566, Sep 1992.
[29] L. D. Tzuang, K. Fang, P. Nussenzveig, S. Fan, and M. Lipson, "Non-reciprocal phase shift induced by an effective magnetic flux for light," *Nature photonics,* vol. 8, p. 701, 2014.
[30] Y. Aharonov and D. Bohm, "Significance of Electromagnetic Potentials in the Quantum Theory," *Physical Review,* vol. 115, pp. 485-491, 08/01/ 1959.
[31] M. Berry, R. Chambers, M. Large, C. Upstill, and J. Walmsley, "Wavefront dislocations in the Aharonov-Bohm effect and its water wave analogue," *European Journal of Physics,* vol. 1, p. 154, 1980.
[32] C. Coste, F. Lund, and M. Umeki, "Scattering of dislocated wave fronts by vertical vorticity and the Aharonov-Bohm effect. I. Shallow water," *Physical Review E,* vol. 60, pp. 4908-4916, 10/01/ 1999.
[33] R. Bernal, C. Coste, F. Lund, and F. Melo, "Normal-Mode-Vortex Interactions," *Physical Review Letters,* vol. 89, p. 034501, 06/25/ 2002.
[34] P. Roux, J. de Rosny, M. Tanter, and M. Fink, "The Aharonov-Bohm effect revisited by an acoustic time-reversal mirror," *Physical review letters,* vol. 79, p. 3170, 1997.
[35] P. Roux and M. Fink, "Experimental evidence in acoustics of the violation of time-reversal invariance induced by vorticity," *EPL (Europhysics Letters),* vol. 32, p. 25, 1995.
[36] R. Labbé and J. F. Pinton, "Propagation of Sound through a Turbulent Vortex," *Physical Review Letters,* vol. 81, pp. 1413-1416, 08/17/ 1998.
[37] M. S. Howe, "On the scattering of sound by a vortex ring," *Journal of Sound and Vibration,* vol. 87, pp. 567-571, 1983/04/22 1983.
[38] I. Belyaev and V. Kop'ev, "On the statement of the problem of sound scattering by a cylindrical vortex," *Acoustical Physics,* vol. 54, pp. 603-614, 2008.
[39] K. Naugolnykh, "Sound scattering by a vortex dipole," *The Journal of the Acoustical Society of America,* vol. 133, pp. 1882-1884, 2013.
[40] B. Liang, X. Guo, J. Tu, D. Zhang, and J. Cheng, "An acoustic rectifier," *Nature materials,* vol. 9, pp. 989-992, 2010.
[41] V. F. Nesterenko, C. Daraio, E. B. Herbold, and S. Jin, "Anomalous wave reflection at the interface of two strongly nonlinear granular media," *Physical Review Letters,* vol. 95, p. 4, Oct 2005.
[42] B. Liang, B. Yuan, and J.-c. Cheng, "Acoustic diode: Rectification of acoustic energy flux in one-dimensional systems," *Physical review letters,* vol. 103, p. 104301, 2009.
[43] B. Li, L. Wang, and G. Casati, "Thermal Diode: Rectification of Heat Flux," *Physical Review Letters,* vol. 93, p. 184301, 10/27/ 2004.
[44] N. Boechler, G. Theocharis, and C. Daraio, "Bifurcation-based acoustic switching and rectification," *Nature Materials,* vol. 10, pp. 665-668, Sep 2011.
[45] Z.-m. Gu, J. Hu, B. Liang, X.-y. Zou, and J.-c. Cheng, "Broadband non-reciprocal transmission of sound with invariant frequency," vol. 6, p. 19824, 01/25/online 2016.
[46] J. Zhang, B. Peng, S. K. Ozdemir, Y. X. Liu, H. Jing, X. Y. Lu, *et al.*, "Giant nonlinearity via breaking parity-time symmetry: A route to low-threshold phonon diodes," *Physical Review B,* vol. 92, p. 13, Sep 2015.
[47] Y.-F. Zhu, X.-Y. Zou, B. Liang, and J.-C. Cheng, "Acoustic one-way open tunnel by using metasurface," *Applied Physics Letters,* vol. 107, p. 113501, 2015.
[48] A. Maznev, A. Every, and O. Wright, "Reciprocity in reflection and transmission: What is a 'phonon diode'?," *Wave Motion,* vol. 50, pp. 776-784, 2013.
[49] F. Farzbod and M. J. Leamy, "Breaking time reversal symmetry with coriolis mean flow systems," *The Journal of the Acoustical Society of America,* vol. 140, pp. 3048-3048, 2016.
[50] E. R. Post, M. Orth, P. R. Russo, and N. Gershenfeld, "E-broidery: Design and fabrication of textile-based computing," *IBM Systems journal,* vol. 39, pp. 840-860, 2000.
[51] S. P. Lacour, S. Wagner, Z. Huang, and Z. Suo, "Stretchable gold conductors on elastomeric substrates," *Applied physics letters,* vol. 82, pp. 2404-2406, 2003.
[52] D. S. Gray, J. Tien, and C. S. Chen, "High-conductivity elastomeric electronics," *Advanced Materials,* vol. 16, pp. 393-397, 2004.
[53] A. C. Siegel, D. A. Bruzewicz, D. B. Weibel, and G. M. Whitesides, "Microsolidics: fabrication of three-

dimensional metallic microstructures in poly (dimethylsiloxane)," *Advanced Materials,* vol. 19, pp. 727-733, 2007.
[54] M. D. Dickey, R. C. Chiechi, R. J. Larsen, E. A. Weiss, D. A. Weitz, and G. M. Whitesides, "Eutectic gallium-indium (EGaIn): a liquid metal alloy for the formation of stable structures in microchannels at room temperature," *Advanced functional materials,* vol. 18, pp. 1097-1104, 2008.
[55] W. M. Haynes, *CRC handbook of chemistry and physics*: CRC press, 2014.
[56] M. Knoblauch, J. M. Hibberd, J. C. Gray, and A. J. van Bel, "A galinstan expansion femtosyringe for microinjection of eukaryotic organelles and prokaryotes," *Nature biotechnology,* vol. 17, pp. 906-909, 1999.
[57] S. Y. Hong, J. Yoon, S. W. Jin, Y. Lim, S.-J. Lee, G. Zi, *et al.*, "High-density, stretchable, all-solid-state microsupercapacitor arrays," *ACS nano,* vol. 8, pp. 8844-8855, 2014.
[58] Y. Lim, J. Yoon, J. Yun, D. Kim, S. Y. Hong, S.-J. Lee, *et al.*, "Biaxially stretchable, integrated array of high performance microsupercapacitors," *ACS nano,* vol. 8, pp. 11639-11650, 2014.
[59] J. Yoon, S. Y. Hong, Y. Lim, S. J. Lee, G. Zi, and J. S. Ha, "Design and fabrication of novel stretchable device arrays on a deformable polymer substrate with embedded liquid-metal interconnections," *Advanced Materials,* vol. 26, pp. 6580-6586, 2014.
[60] N. Lazarus, C. Meyer, S. Bedair, H. Nochetto, and I. Kierzewski, "Multilayer liquid metal stretchable inductors," *Smart materials and structures,* vol. 23, p. 085036, 2014.
[61] N. Lazarus, C. Meyer, and W. Turner, "A microfluidic wireless power system," *Rsc Advances,* vol. 5, pp. 78695-78700, 2015.
[62] S. W. Jin, J. Park, S. Y. Hong, H. Park, Y. R. Jeong, J. Park, *et al.*, "Stretchable loudspeaker using liquid metal microchannel," *Scientific reports,* vol. 5, pp. 1-13, 2015.
[63] Y.-L. Park, B.-R. Chen, and R. J. Wood, "Design and fabrication of soft artificial skin using embedded microchannels and liquid conductors," *IEEE Sensors Journal,* vol. 12, pp. 2711-2718, 2012.
[64] N. Kazem, T. Hellebrekers, and C. Majidi, "Soft multifunctional composites and emulsions with liquid metals," *Advanced Materials,* vol. 29, p. 1605985, 2017.
[65] J. H. So, J. Thelen, A. Qusba, G. J. Hayes, G. Lazzi, and M. D. Dickey, "Reversibly deformable and mechanically tunable fluidic antennas," *Advanced Functional Materials,* vol. 19, pp. 3632-3637, 2009.
[66] A. N. Gent, "On the relation between indentation hardness and Young's modulus," *Rubber Chemistry and Technology,* vol. 31, pp. 896-906, 1958.
[67] F. Farzbod, "Resonant ultrasound spectroscopy for a sample with cantilever boundary condition using Rayleigh-Ritz method," *Journal of applied physics,* vol. 114, p. 024902, 2013.
[68] C.-X. Zhao, "Multiphase flow microfluidics for the production of single or multiple emulsions for drug delivery," *Advanced drug delivery reviews,* vol. 65, pp. 1420-1446, 2013.
[69] W. Jung, J. Han, J.-W. Choi, and C. H. Ahn, "Point-of-care testing (POCT) diagnostic systems using microfluidic lab-on-a-chip technologies," *Microelectronic Engineering,* vol. 132, pp. 46-57, 2015.
[70] J. Hu, X. Cui, Y. Gong, X. Xu, B. Gao, T. Wen, *et al.*, "Portable microfluidic and smartphone-based devices for monitoring of cardiovascular diseases at the point of care," *Biotechnology advances,* vol. 34, pp. 305-320, 2016.
[71] G. M. Whitesides, "The origins and the future of microfluidics," *nature,* vol. 442, pp. 368-373, 2006.
[72] S. N. Bhatia and D. E. Ingber, "Microfluidic organs-on-chips," *Nature biotechnology,* vol. 32, pp. 760-772, 2014.
[73] B. S. Lee, Y. U. Lee, H.-S. Kim, T.-H. Kim, J. Park, J.-G. Lee, *et al.*, "Fully integrated lab-on-a-disc for simultaneous analysis of biochemistry and immunoassay from whole blood," *Lab on a Chip,* vol. 11, pp. 70-78, 2011.
[74] M. S. Luchansky, A. L. Washburn, M. S. McClellan, and R. C. Bailey, "Sensitive on-chip detection of a protein biomarker in human serum and plasma over an extended dynamic range using silicon photonic microring resonators and sub-micron beads," *Lab on a Chip,* vol. 11, pp. 2042-2044, 2011.
[75] R. Fan, O. Vermesh, A. Srivastava, B. K. Yen, L. Qin, H. Ahmad, *et al.*, "Integrated barcode chips for rapid, multiplexed analysis of proteins in microliter quantities of blood," *Nature biotechnology,* vol. 26, pp. 1373-1378, 2008.
[76] E. K. Sackmann, A. L. Fulton, and D. J. Beebe, "The present and future role of microfluidics in biomedical research," *Nature,* vol. 507, pp. 181-189, 2014.
[77] B. C. Dhar and N. Y. Lee, "Lab-on-a-chip technology for environmental monitoring of microorganisms," *Biochip Journal,* vol. 12, pp. 173-183, 2018.
[78] F. Dugue, F. Roux, B. Bonafos, J.-Y. Billard, D. Fruman, and I. Gibek, "Development of a micropump for hydrazine propulsion systems," in *37th Joint Propulsion Conference and Exhibit*, 2001, p. 3831.

[79] R. Krpoun and H. Shea, "Integrated out-of-plane nanoelectrospray thruster arrays for spacecraft propulsion," *Journal of Micromechanics and Microengineering,* vol. 19, p. 045019, 2009.
[80] J. Xiong, Z. Zhou, X. Ye, X. Wang, Y. Feng, and Y. Li, "A colloid micro-thruster system," *Microelectronic Engineering,* vol. 61, pp. 1031-1037, 2002.
[81] J. Darabi and K. Ekula, "Development of a chip-integrated micro cooling device," *Microelectronics Journal,* vol. 34, pp. 1067-1074, 2003.
[82] S. V. Garimella, V. Singhal, and D. Liu, "On-chip thermal management with microchannel heat sinks and integrated micropumps," *Proceedings of the IEEE,* vol. 94, pp. 1534-1548, 2006.
[83] V. Singhal, S. V. Garimella, and A. Raman, "Microscale pumping technologies for microchannel cooling systems," *Appl. Mech. Rev.,* vol. 57, pp. 191-221, 2004.
[84] M. K. Sung and I. Mudawar, "Single-phase and two-phase hybrid cooling schemes for high-heat-flux thermal management of defense electronics," *Journal of Electronic Packaging,* vol. 131, 2009.
[85] R. Luharuka, C.-F. Wu, and P. J. Hesketh, "Design, fabrication, and testing of a near constant pressure fuel delivery system for miniature fuel cells," *Sensors and Actuators A: Physical,* vol. 112, pp. 187-195, 2004.
[86] X. Yang, Z. Zhou, H. Cho, and X. Luo, "Study on a PZT-actuated diaphragm pump for air supply for micro fuel cells," *Sensors and Actuators A: Physical,* vol. 130, pp. 531-536, 2006.
[87] T. Zhang and Q.-M. Wang, "Valveless piezoelectric micropump for fuel delivery in direct methanol fuel cell (DMFC) devices," *Journal of power sources,* vol. 140, pp. 72-80, 2005.
[88] F. Amirouche, Y. Zhou, and T. Johnson, "Current micropump technologies and their biomedical applications," *Microsystem technologies,* vol. 15, pp. 647-666, 2009.
[89] S. Herrlich, S. Spieth, S. Messner, and R. Zengerle, "Osmotic micropumps for drug delivery," *Advanced drug delivery reviews,* vol. 64, pp. 1617-1627, 2012.
[90] A. Nisar, N. Afzulpurkar, B. Mahaisavariya, and A. Tuantranont, "MEMS-based micropumps in drug delivery and biomedical applications," *Sensors and Actuators B: Chemical,* vol. 130, pp. 917-942, 2008.
[91] C. Zhang, D. Xing, and Y. Li, "Micropumps, microvalves, and micromixers within PCR microfluidic chips: advances and trends," *Biotechnology advances,* vol. 25, pp. 483-514, 2007.
[92] C. K. Byun, K. Abi-Samra, Y. K. Cho, and S. Takayama, "Pumps for microfluidic cell culture," *Electrophoresis,* vol. 35, pp. 245-257, 2014.
[93] Y.-N. Wang and L.-M. Fu, "Micropumps and biomedical applications–A review," *Microelectronic Engineering,* vol. 195, pp. 121-138, 2018.
[94] G. Gautschi, "Piezoelectric sensors," in *Piezoelectric Sensorics*, ed: Springer, 2002, pp. 73-91.
[95] S. Xu, B. J. Hansen, and Z. L. Wang, "Piezoelectric-nanowire-enabled power source for driving wireless microelectronics," *Nature communications,* vol. 1, pp. 1-5, 2010.
[96] Y. Xu, X. Hu, S. Kundu, A. Nag, N. Afsarimanesh, S. Sapra, *et al.*, "Silicon-based sensors for biomedical applications: a review," *Sensors,* vol. 19, p. 2908, 2019.
[97] S. Laschi and M. Mascini, "Planar electrochemical sensors for biomedical applications," *Medical engineering & physics,* vol. 28, pp. 934-943, 2006.
[98] X. Y. Wang, Y. T. Ma, G. Y. Yan, and Z. H. Feng, "A compact and high flow-rate piezoelectric micropump with a folded vibrator," *Smart materials and structures,* vol. 23, p. 115005, 2014.
[99] X. Y. Wang, Y. T. Ma, G. Y. Yan, D. Huang, and Z. H. Feng, "High flow-rate piezoelectric micropump with two fixed ends polydimethylsiloxane valves and compressible spaces," *Sensors and Actuators A: Physical,* vol. 218, pp. 94-104, 2014.
[100] S. Fournier and E. Chappel, "Dynamic simulations of a piezoelectric driven MEMS micropump," *Procedia Engineering,* vol. 168, pp. 860-863, 2016.
[101] S. Fournier and E. Chappel, "Modeling of a piezoelectric MEMS micropump dedicated to insulin delivery and experimental validation using integrated pressure sensors: Application to partial occlusion management," *Journal of Sensors,* vol. 2017, 2017.
[102] A. Shabanian, F. Goldschmidtboeing, S. Vilches, H.-H. Phan, A. B. Kashekodi, P. Rajaeipour, *et al.*, "A novel piezo actuated high stroke membrane for micropumps," *Microelectronic Engineering,* vol. 158, pp. 26-29, 2016.
[103] J. S. Dong, W. H. Chen, P. Zeng, R. G. Liu, C. Shen, W. S. Liu, *et al.*, "Design and experimental research on piezoelectric pump with triple vibrators," *Microsystem Technologies,* vol. 23, pp. 3019-3026, 2017.
[104] R. K. Haldkar, V. K. Gupta, and T. Sheorey, "Modeling and flow analysis of piezoelectric based micropump with various shapes of microneedle," *Journal of Mechanical Science and Technology,* vol. 31, pp. 2933-2941, 2017.
[105] J. Wang, Y. Liu, Y. Shen, S. Chen, and Z. Yang, "A resonant piezoelectric diaphragm pump transferring gas

with compact structure," *Micromachines,* vol. 7, p. 219, 2016.
[106] R. Zhang, F. You, Z. Lv, Z. He, H. Wang, and L. Huang, "Development and characterization a single-active-chamber piezoelectric membrane pump with multiple passive check valves," *Sensors,* vol. 16, p. 2108, 2016.
[107] H. Conrad, H. Schenk, B. Kaiser, S. Langa, M. Gaudet, K. Schimmanz, *et al.*, "A small-gap electrostatic micro-actuator for large deflections," *Nature communications,* vol. 6, pp. 1-7, 2015.
[108] O. Francais and I. Dufour, "Dynamic simulation of an electrostatic micropump with pull-in and hysteresis phenomena," *Sensors and Actuators A: Physical,* vol. 70, pp. 56-60, 1998.
[109] A. Machauf, Y. Nemirovsky, and U. Dinnar, "A membrane micropump electrostatically actuated across the working fluid," *Journal of Micromechanics and Microengineering,* vol. 15, p. 2309, 2005.
[110] H. Kim, A. A. Astle, K. Najafi, L. P. Bernal, and P. D. Washabaugh, "An integrated electrostatic peristaltic 18-stage gas micropump with active microvalves," *Journal of Microelectromechanical Systems,* vol. 24, pp. 192-206, 2015.
[111] H.-C. Hsieh and H. Kim, "A miniature closed-loop gas chromatography system," *Lab on a Chip,* vol. 16, pp. 1002-1012, 2016.
[112] I. Lee, P. Hong, C. Cho, B. Lee, K. Chun, and B. Kim, "Four-electrode micropump with peristaltic motion," *Sensors and Actuators A: Physical,* vol. 245, pp. 19-25, 2016.
[113] F. A. M. Ghazali, C. K. Mah, A. AbuZaiter, P. S. Chee, and M. S. M. Ali, "Soft dielectric elastomer actuator micropump," *Sensors and Actuators A: Physical,* vol. 263, pp. 276-284, 2017.
[114] Z. Chen, T. I. Um, and H. Bart-Smith, "A novel fabrication of ionic polymer–metal composite membrane actuator capable of 3-dimensional kinematic motions," *Sensors and Actuators A: Physical,* vol. 168, pp. 131-139, 2011.
[115] J. Khawwaf, J. Zheng, R. Lu, A. Al-Ghanimi, B. I. Kazem, and Z. Man, "Robust tracking control of an IPMC actuator using nonsingular terminal sliding mode," *Smart Materials and Structures,* vol. 26, p. 095042, 2017.
[116] E. Esmaeli, M. Ganjian, H. Rastegar, M. Kolahdouz, Z. Kolahdouz, and G. Q. Zhang, "Humidity sensor based on the ionic polymer metal composite," *Sensors and Actuators B: Chemical,* vol. 247, pp. 498-504, 2017.
[117] C. Meis, R. Montazami, and N. Hashemi, "Ionic electroactive polymer actuators as active microfluidic mixers," *Analytical Methods,* vol. 7, pp. 10217-10223, 2015.
[118] M. Ashouri, M. B. Shafii, and A. Moosavi, "Theoretical and experimental studies of a magnetically actuated valveless micropump," *Journal of Micromechanics and Microengineering,* vol. 27, p. 015016, 2016.
[119] T.-S. Leu and P.-C. Jiang, "Fe-PDMS fabricated microchannels for peristaltic pump applications," in *2010 IEEE 5th International Conference on Nano/Micro Engineered and Molecular Systems*, 2010, pp. 646-649.
[120] A. Al-Halhouli, M. Kilani, and S. Büttgenbach, "Development of a novel electromagnetic pump for biomedical applications," *Sensors and Actuators A: Physical,* vol. 162, pp. 172-176, 2010.
[121] V. Chaudhary, Z. Wang, A. Ray, I. Sridhar, and R. Ramanujan, "Self pumping magnetic cooling," *Journal of Physics D: Applied Physics,* vol. 50, p. 03LT03, 2016.
[122] M. M. Said, J. Yunas, B. Bais, A. A. Hamzah, and B. Y. Majlis, "Hybrid polymer composite membrane for an electromagnetic (EM) valveless micropump," *Journal of Micromechanics and Microengineering,* vol. 27, p. 075027, 2017.
[123] Y.-M. Choi, J. J. Gorman, N. G. Dagalakis, S. H. Yang, Y. Kim, and J. M. Yoo, "A high-bandwidth electromagnetic MEMS motion stage for scanning applications," *Journal of Micromechanics and Microengineering,* vol. 22, p. 105012, 2012.
[124] H.-T. Chang, C.-Y. Lee, and C.-Y. Wen, "Design and modeling of electromagnetic actuator in mems-based valveless impedance pump," *Microsystem Technologies,* vol. 13, pp. 1615-1622, 2007.
[125] Y. Su and W. Chen, "Investigation on electromagnetic microactuator and its application in micro-electro-mechanical system (MEMS)," in *2007 International Conference on Mechatronics and Automation*, 2007, pp. 3250-3254.
[126] H.-T. Chang, C.-Y. Wen, and C.-Y. Lee, "Design, analysis and optimization of an electromagnetic actuator for a micro impedance pump," *Journal of Micromechanics and Microengineering,* vol. 19, p. 085026, 2009.
[127] Y. Su, W. Chen, F. Cui, and W. Zhang, "Analysis and fabrication process of an electro-magnetically actuated valveless micropump with two parallel flexible diaphragms," *Proceedings of the Institution of Mechanical Engineers, Part C: Journal of Mechanical Engineering Science,* vol. 219, pp. 1007-1014, 2005.
[128] Y.-f. Su, W.-y. Chen, F. Cui, and W.-p. Zhang, "Design and fabrication process of electromagnetically actuated valveless micropump with two parallel flexible diaphragms," *Journal of Shanghai University (English Edition),* vol. 11, pp. 79-83, 2007.
[129] Y. Su, H. Wang, and W. Chen, "Microactuator based on electroplated permanent magnets and flexible

polydimethyl siloxane diaphragm," *Proceedings of the Institution of Mechanical Engineers, Part C: Journal of Mechanical Engineering Science,* vol. 222, pp. 517-524, 2008.
[130] M. Lee and T. H. Lee, "Vector potential current method for design sensitivity analysis of static electromagnetic-structure coupled problem," *IEEE transactions on magnetics,* vol. 47, pp. 1298-1301, 2011.
[131] A. Feustel, O. Krusemark, and J. Müller, "Numerical simulation and optimization of planar electromagnetic actuators," *Sensors and Actuators A: Physical,* vol. 70, pp. 276-282, 1998.
[132] C.-H. Ko, J. Yang, J.-C. Chiou, S.-C. Chen, and T. Kao, "Magnetic analysis of a micromachined magnetic actuator using the finite element method," in *Design, Characterization, and Packaging for MEMS and Microelectronics*, 1999, pp. 127-136.
[133] C.-Y. Lee, H.-T. Chang, and C.-Y. Wen, "A MEMS-based valveless impedance pump utilizing electromagnetic actuation," *Journal of Micromechanics and Microengineering,* vol. 18, p. 035044, 2008.
[134] A. Beyzavi and N.-T. Nguyen, "Modeling and optimization of planar microcoils," *Journal of Micromechanics and Microengineering,* vol. 18, p. 095018, 2008.
[135] H.-T. Chang, C.-Y. Lee, C.-Y. Wen, and B.-S. Hong, "Theoretical analysis and optimization of electromagnetic actuation in a valveless microimpedance pump," *Microelectronics journal,* vol. 38, pp. 791-799, 2007.
[136] H.-C. Chiu, C.-H. Yeh, H.-W. Yeh, and J.-H. Jang, "Development and Performance of an Electro-Magnetic Driven Miniature Piston Pump," *Journal of Marine Science and Technology,* vol. 23, pp. 508-515, 2015.
[137] J. Ni, B. Wang, S. Chang, and Q. Lin, "An integrated planar magnetic micropump," *Microelectronic engineering,* vol. 117, pp. 35-40, 2014.
[138] W. Hilber, S. Clara, and B. Jakoby, "Microfluidic pumping utilizing a PDMS membrane with an integrated nonuniform open-porous foam," *IEEE Sensors Journal,* vol. 15, pp. 5109-5114, 2015.
[139] C. Gao and Y. Jian, "Analytical solution of magnetohydrodynamic flow of Jeffrey fluid through a circular microchannel," *Journal of Molecular Liquids,* vol. 211, pp. 803-811, 2015.
[140] M. Karmozdi, A. Salari, and M. B. Shafii, "Experimental study of a novel Magneto Mercury Reciprocating (MMR) micropump, fabrication and operation," *Sensors and Actuators A: Physical,* vol. 194, pp. 277-284, 2013.
[141] M. Rivero and S. Cuevas, "Analysis of the slip condition in magnetohydrodynamic (MHD) micropumps," *Sensors and actuators B: Chemical,* vol. 166, pp. 884-892, 2012.
[142] M. I. Hasan, A. J. F. Ali, and R. S. Tufah, "Numerical study of the effect of channel geometry on the performance of Magnetohydrodynamic micro pump," *Engineering science and technology, an international journal,* vol. 20, pp. 982-989, 2017.
[143] M. Karmozdi, M. B. Shafii, and H. Afshin, "The effect of droplet size, channel length and the amount of electromagnetic actuation force on reciprocating movement of mercury droplets in the magneto mercury reciprocating (MMR) micropumps," *Sensors and Actuators A: Physical,* vol. 283, pp. 204-210, 2018.
[144] S.-Y. Tang, K. Khoshmanesh, V. Sivan, P. Petersen, A. P. O'Mullane, D. Abbott, *et al.*, "Liquid metal enabled pump," *Proceedings of the National Academy of Sciences,* vol. 111, pp. 3304-3309, 2014.
[145] J. Y. Zhu, S.-Y. Tang, K. Khoshmanesh, and K. Ghorbani, "An integrated liquid cooling system based on galinstan liquid metal droplets," *ACS applied materials & interfaces,* vol. 8, pp. 2173-2180, 2016.
[146] A. Malvandi and D. Ganji, "Magnetohydrodynamic mixed convective flow of Al2O3–water nanofluid inside a vertical microtube," *Journal of Magnetism and Magnetic Materials,* vol. 369, pp. 132-141, 2014.
[147] M. Sheikholeslami and R. Ellahi, "Three dimensional mesoscopic simulation of magnetic field effect on natural convection of nanofluid," *International Journal of Heat and Mass Transfer,* vol. 89, pp. 799-808, 2015.
[148] M. Turkyilmazoglu, "Mixed convection flow of magnetohydrodynamic micropolar fluid due to a porous heated/cooled deformable plate: exact solutions," *International Journal of Heat and Mass Transfer,* vol. 106, pp. 127-134, 2017.
[149] O. G. Cassells, W. K. Hussam, and G. J. Sheard, "Heat transfer enhancement using rectangular vortex promoters in confined quasi-two-dimensional magnetohydrodynamic flows," *International Journal of Heat and Mass Transfer,* vol. 93, pp. 186-199, 2016.
[150] M. Kiyasatfar and N. Pourmahmoud, "Laminar MHD flow and heat transfer of power-law fluids in square microchannels," *International Journal of Thermal Sciences,* vol. 99, pp. 26-35, 2016.
[151] J. Lee and C.-J. Kim, "Surface-tension-driven microactuation based on continuous electrowetting," *Journal of Microelectromechanical Systems,* vol. 9, pp. 171-180, 2000.
[152] S.-Y. Tang, V. Sivan, K. Khoshmanesh, A. P. O'Mullane, X. Tang, B. Gol, *et al.*, "Electrochemically induced actuation of liquid metal marbles," *Nanoscale,* vol. 5, pp. 5949-5957, 2013.

[153] M. Gao and L. Gui, "A handy liquid metal based electroosmotic flow pump," *Lab on a Chip*, vol. 14, pp. 1866-1872, 2014.
[154] E. Stemme and G. Stemme, "A valveless diffuser/nozzle-based fluid pump," *Sensors and Actuators A: physical*, vol. 39, pp. 159-167, 1993.
[155] K. Yang, M. Liu, I. Chen, and C. Wang, "Analysis of microdiffuser/nozzles," *Proceedings of the Institution of Mechanical Engineers, Part C: Journal of Mechanical Engineering Science*, vol. 220, pp. 1289-1296, 2006.
[156] S. C. Lee, S. Hur, D. Kang, B. H. Kim, and S. J. Lee, "The performance of bioinspired valveless piezoelectric micropump with respect to viscosity change," *Bioinspiration & biomimetics*, vol. 11, p. 036006, 2016.
[157] Z. Ma, Y. Zhou, D. J. Collins, and Y. Ai, "Fluorescence activated cell sorting via a focused traveling surface acoustic beam," *Lab on a Chip*, vol. 17, pp. 3176-3185, 2017.
[158] L.-J. Yang, T.-Y. Lin, and Y.-C. Ou, "A Thermopneumatic Valveless Micropump With PDMS-Based Nozzle/Diffuser Structure for Microfluidic System," in *ASME 2008 First International Conference on Micro/Nanoscale Heat Transfer*, 2008, pp. 293-296.
[159] K. Kikuchi, M. A. Stremler, S. Chatterjee, W.-K. Lee, O. Mochizuki, and J. J. Socha, "Burst mode pumping: A new mechanism of drinking in mosquitoes," *Scientific reports*, vol. 8, pp. 1-15, 2018.
[160] S. C. Lee, B. H. Kim, and S. J. Lee, "Experimental analysis of the liquid-feeding mechanism of the butterfly Pieris rapae," *Journal of Experimental Biology*, vol. 217, pp. 2013-2019, 2014.
[161] A. Azarbadegan, C. Cortes-Quiroz, I. Eames, and M. Zangeneh, "Analysis of double-chamber parallel valveless micropumps," *Microfluidics and Nanofluidics*, vol. 9, pp. 171-180, 2010.
[162] J. Kan, K. Tang, G. Liu, G. Zhu, and C. Shao, "Development of serial-connection piezoelectric pumps," *Sensors and Actuators A: Physical*, vol. 144, pp. 321-327, 2008.
[163] Y.-Y. Tsui and S.-L. Lu, "Evaluation of the performance of a valveless micropump by CFD and lumped-system analyses," *Sensors and Actuators A: Physical*, vol. 148, pp. 138-148, 2008.
[164] A. Ullmann, "The piezoelectric valve-less pump—performance enhancement analysis," *Sensors and Actuators A: Physical*, vol. 69, pp. 97-105, 1998.
[165] C.-J. Lee, H.-J. Sheen, Z.-K. Tu, U. Lei, and C.-Y. Yang, "A study of PZT valveless micropump with asymmetric obstacles," *Microsystem technologies*, vol. 15, pp. 993-1000, 2009.
[166] F. Farzbod, M. Naghdi, and P. M. Goggans, "Using Liquid Metal in an Electromechanical Motor With Breathing Mode Motion," *Journal of Vibration and Acoustics*, vol. 141, p. 014501, 2019.
[167] B. H. Kim, Kim, H.K. and Lee, S.J., "Experimental analysis of the blood-sucking mechanism of female mosquitoes," *Journal of Experimental Biology*, vol. 214, pp. 1163-1169, 2011.
[168] S. J. Lee, Kang, D., Lee, S.C. and Ha, Y.R, "Peculiar liquid-feeding and pathogen transmission behavior of Aedes togoi and comparison with Anopheles sinensis," *Scientific reports*, vol. 6, p. 20464, 2016.
[169] A. Olsson, P. Enoksson, G. Stemme, and E. Stemme, "A valve-less planar pump isotropically etched in silicon," *Journal of Micromechanics and Microengineering*, vol. 6, p. 87, 1996.
[170] A. Olsson, P. Enoksson, G. Stemme, and E. Stemme, "Micromachined flat-walled valveless diffuser pumps," *Journal of microelectromechanical systems*, vol. 6, pp. 161-166, 1997.
[171] R. Tanton, G. Sullivan, and M. Matevia, "Platinum-Cure Technology Eases Processing 01 Molded Silicone Rubber," 1992.

APPENDIX

LIST OF APPENDENCES

MATLAB Code for the Top 10%, and Top 30%

```
% top 10%
clear all
clc
mm=load ('4k1500.txt');
x=mm(:,1); y=mm(:,2); u1=mm(:,3);
uf=[x y u1];
uu=0; i=0;
for j=1:length(x)
    if uf(j,3)>.90*max(mm(:,3))
        i=i+1;
        uu(i,1)=uf(j,1);
        uu(i,2)=uf(j,2);
        uu(i,3)=uf(j,3);
    end;
end
xm=mean(uu(:,1));
ym=mean(uu(:,2));
theta=atan(ym/xm)*180/pi
rm=sqrt(xm^2+ym^2)
```

```
% top 30%
clear all
clc
mm=load ('20k1700.txt');
x=mm(:,1); y=mm(:,2); u1=mm(:,3);
uf=[x y u1];
uu=0; i=0;
for j=1:length(x)
    if uf(j,3)>.70*max(mm(:,3))
        i=i+1;
        uu(i,1)=uf(j,1);
        uu(i,2)=uf(j,2);
        uu(i,3)=uf(j,3);
    end;
end
xm=mean(uu(:,1));
ym=mean(uu(:,2));
theta=atan(ym/xm)*180/pi
rm=sqrt(xm^2+ym^2)
```

Micropump CAD Details
(all Dimensions in inch)

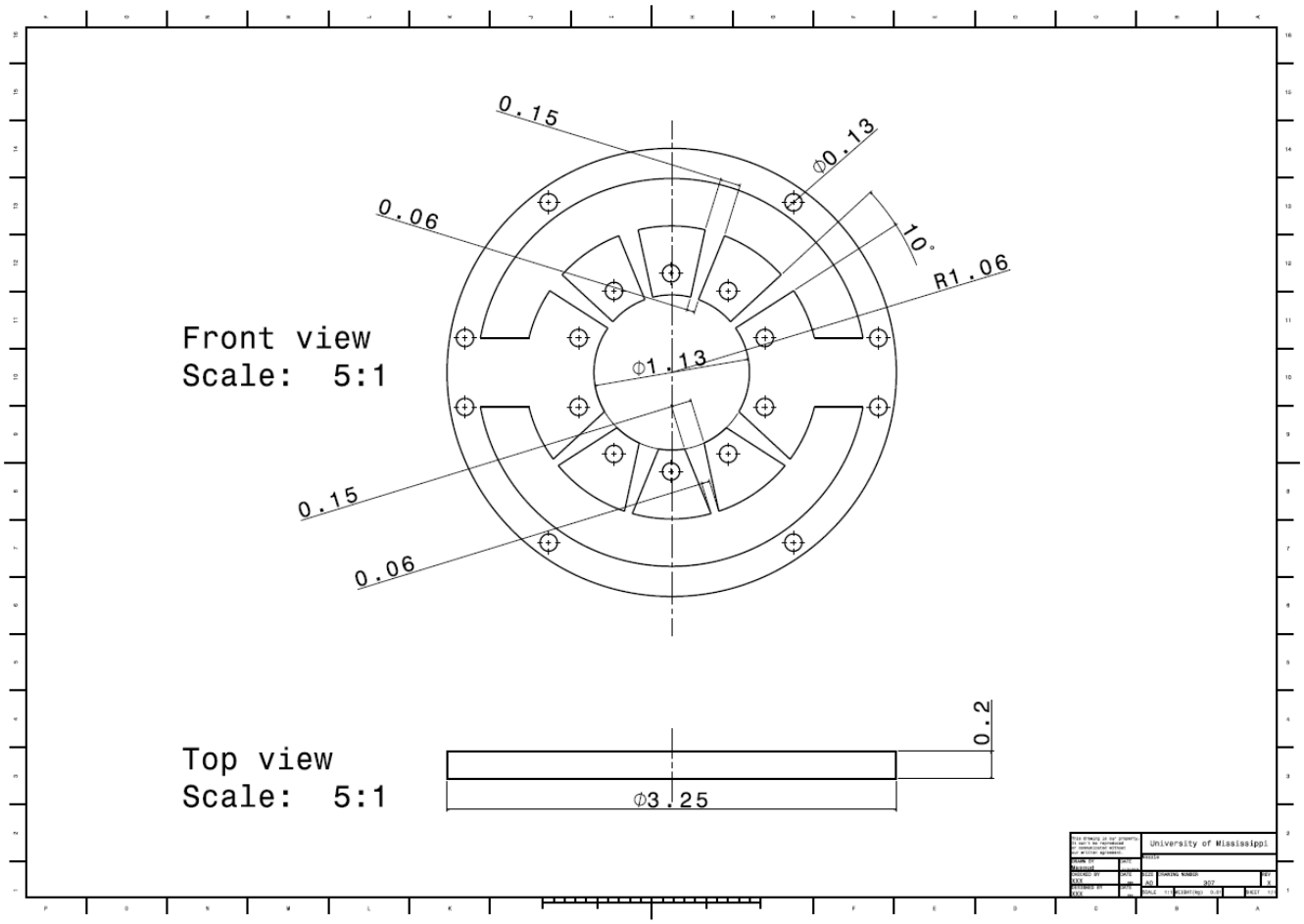

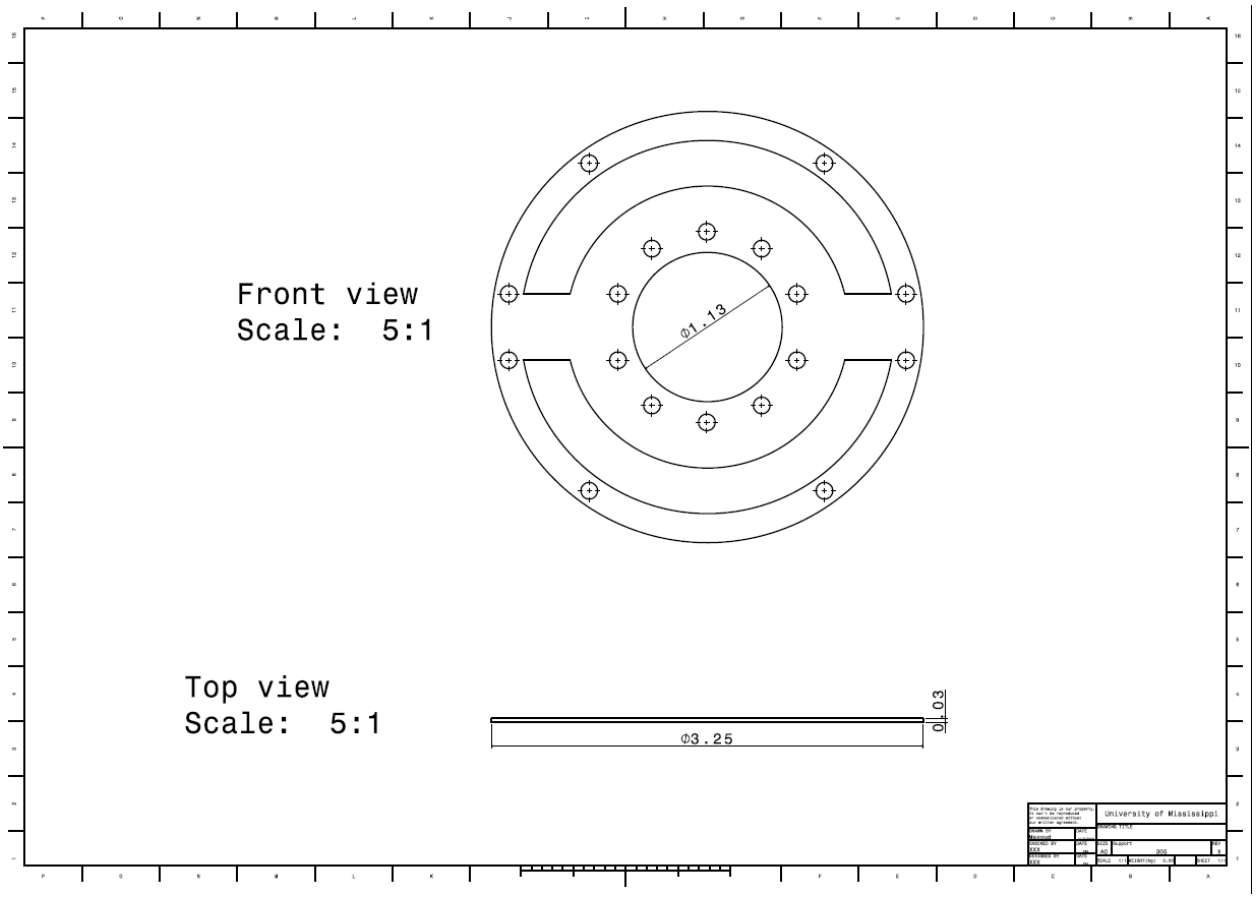
Front view
Scale: 5:1
Φ1.13
Top view
Scale: 5:1
0.03
Φ3.25

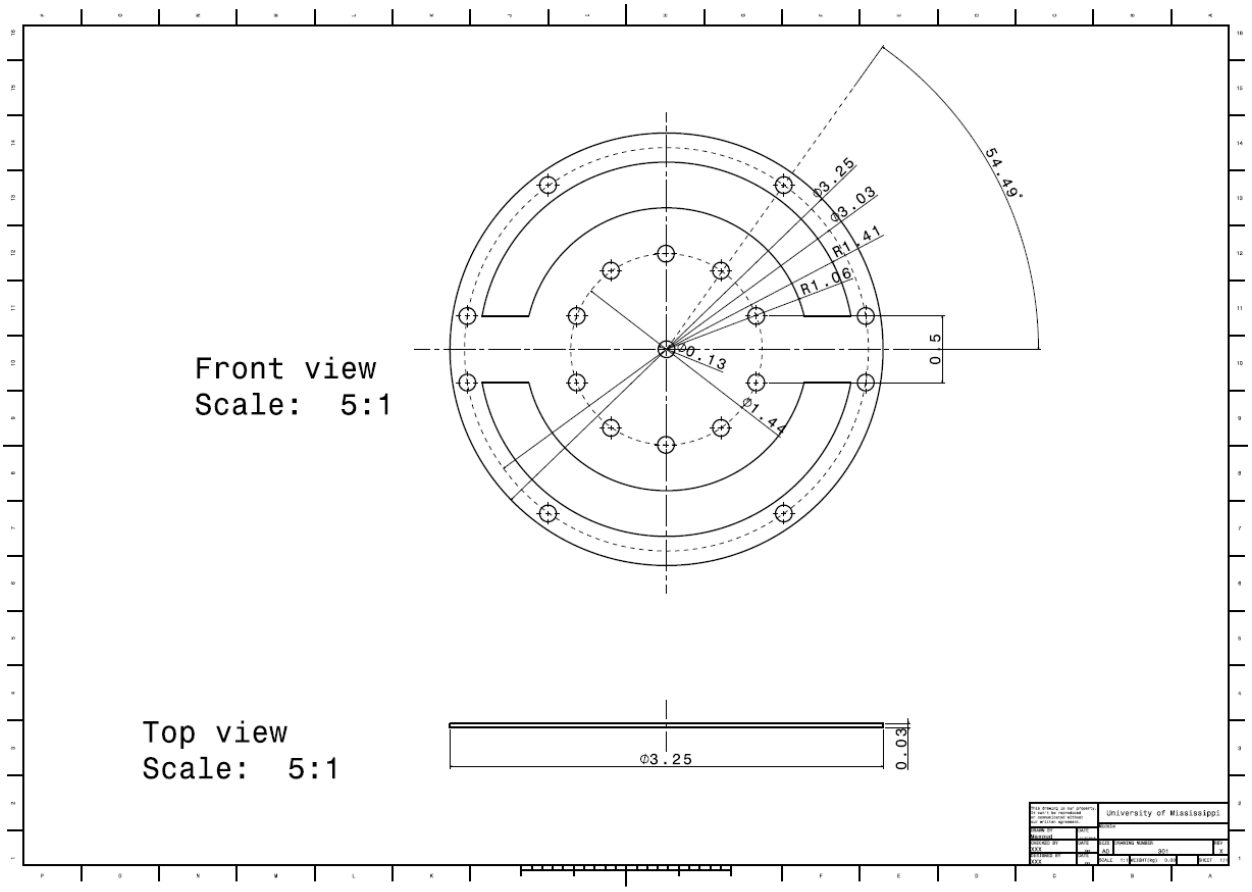
Front view
Scale: 5:1
54.49°
Ø3.25
Ø3.03
R1.41
R1.06
0.5
Ø0.13
Ø1.44
Top view
Scale: 5:1
Ø3.25
0.03
University of Mississippi

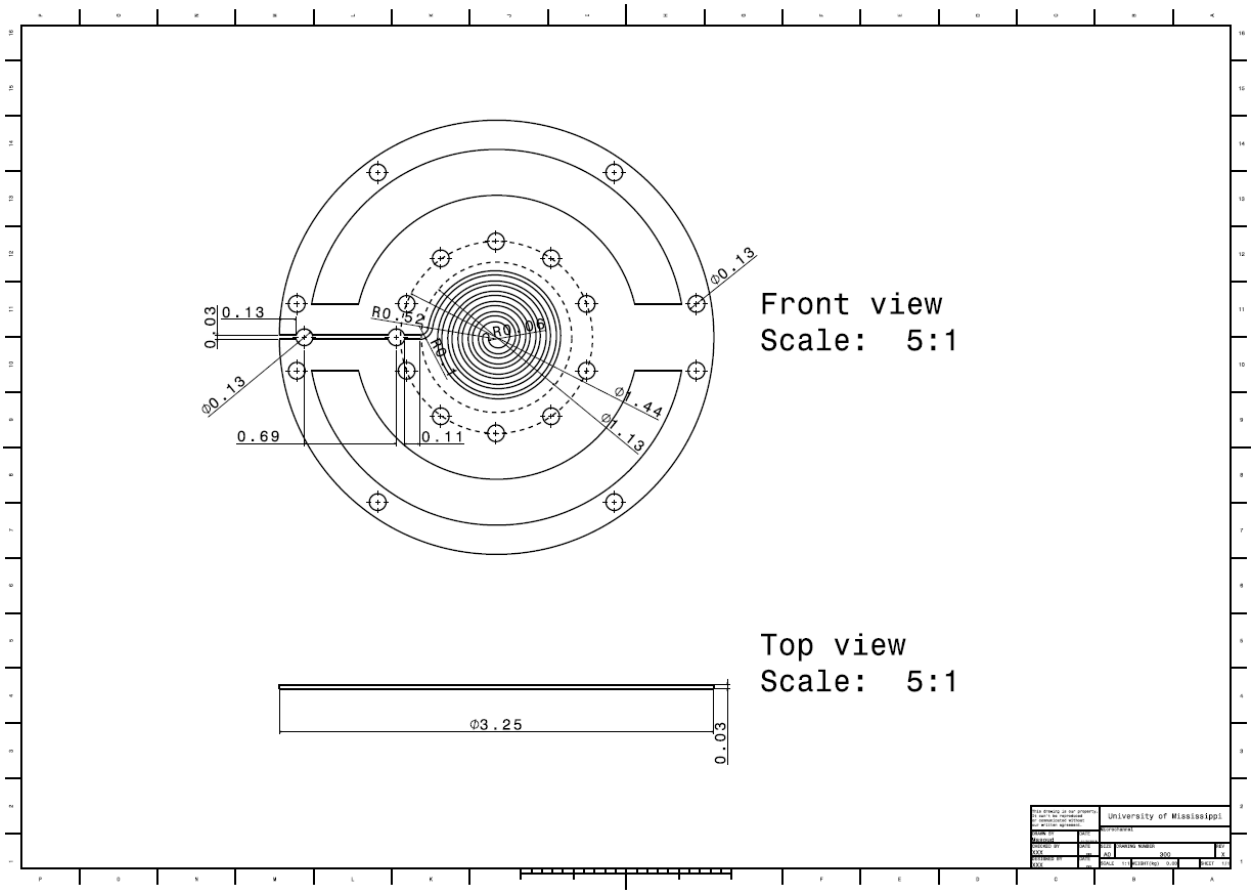
Front view
Scale: 5:1
Top view
Scale: 5:1
0.13
0.03
R0.52
R0.08
R0.4
Ø0.13
Ø0.13
Ø1.44
Ø1.13
0.69
0.11
Ø3.25
0.03
University of Mississippi

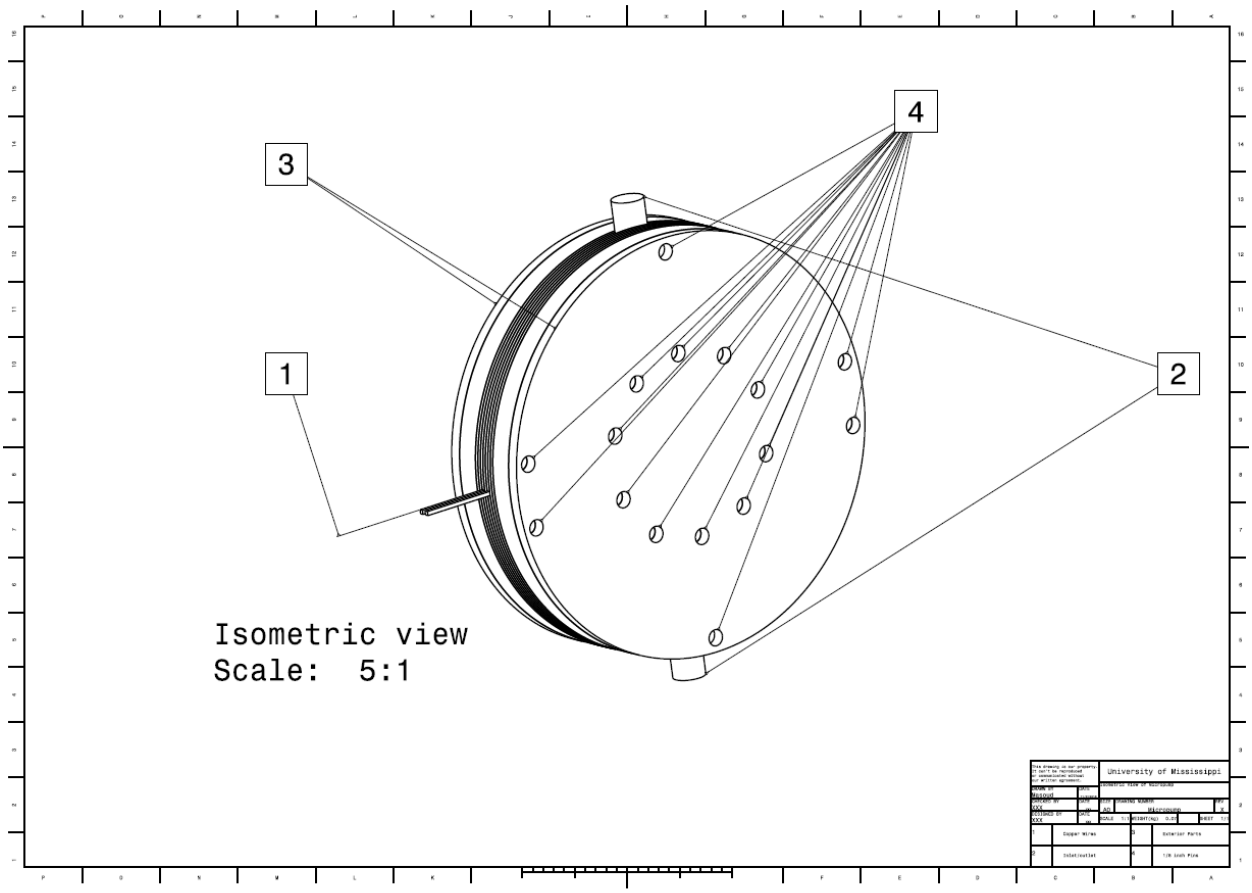
4
3
2
1
Isometric view
Scale: 5:1
University of Mississippi

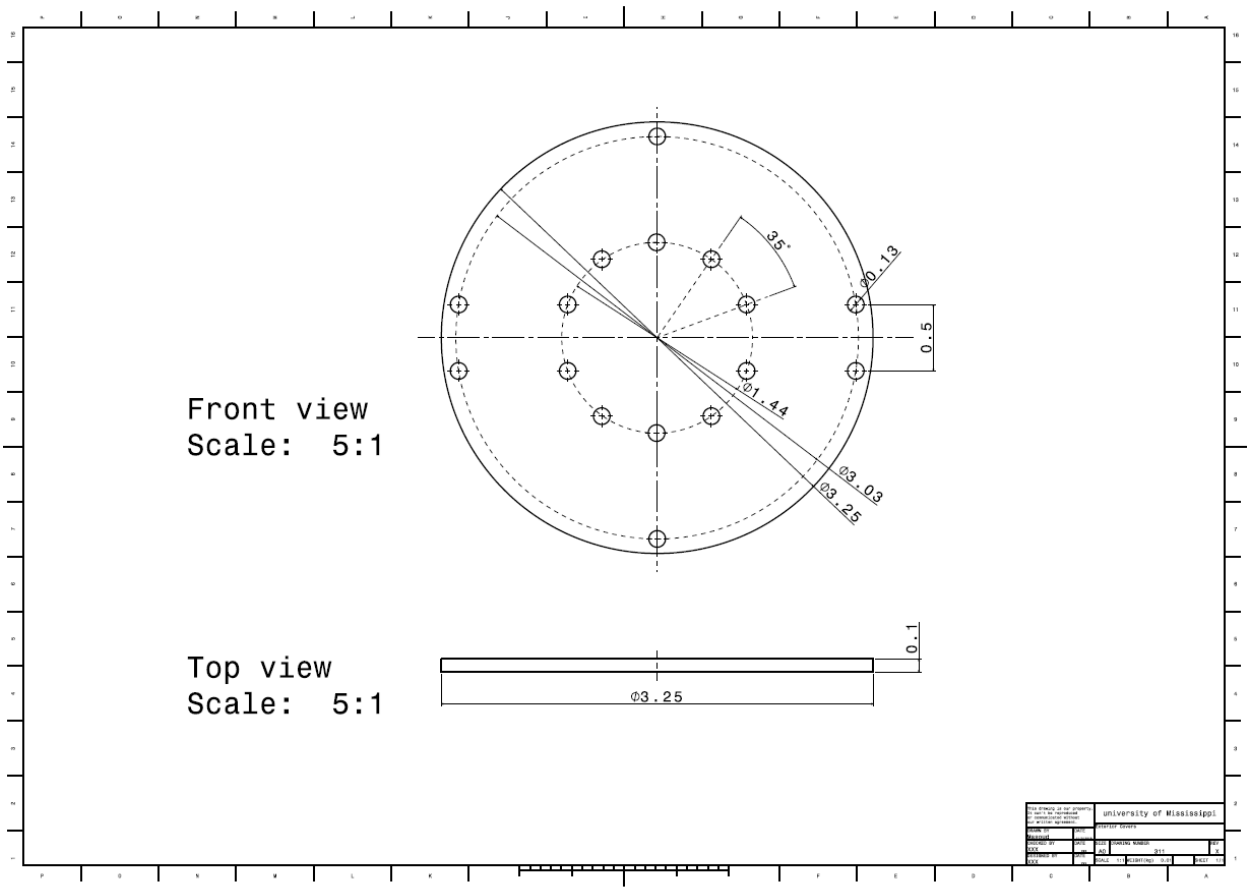
Front view
Scale: 5:1
35°
Ø0.13
0.5
Ø1.44
Ø3.03
Ø3.25
Top view
Scale: 5:1
0.1
Ø3.25
university of Mississippi

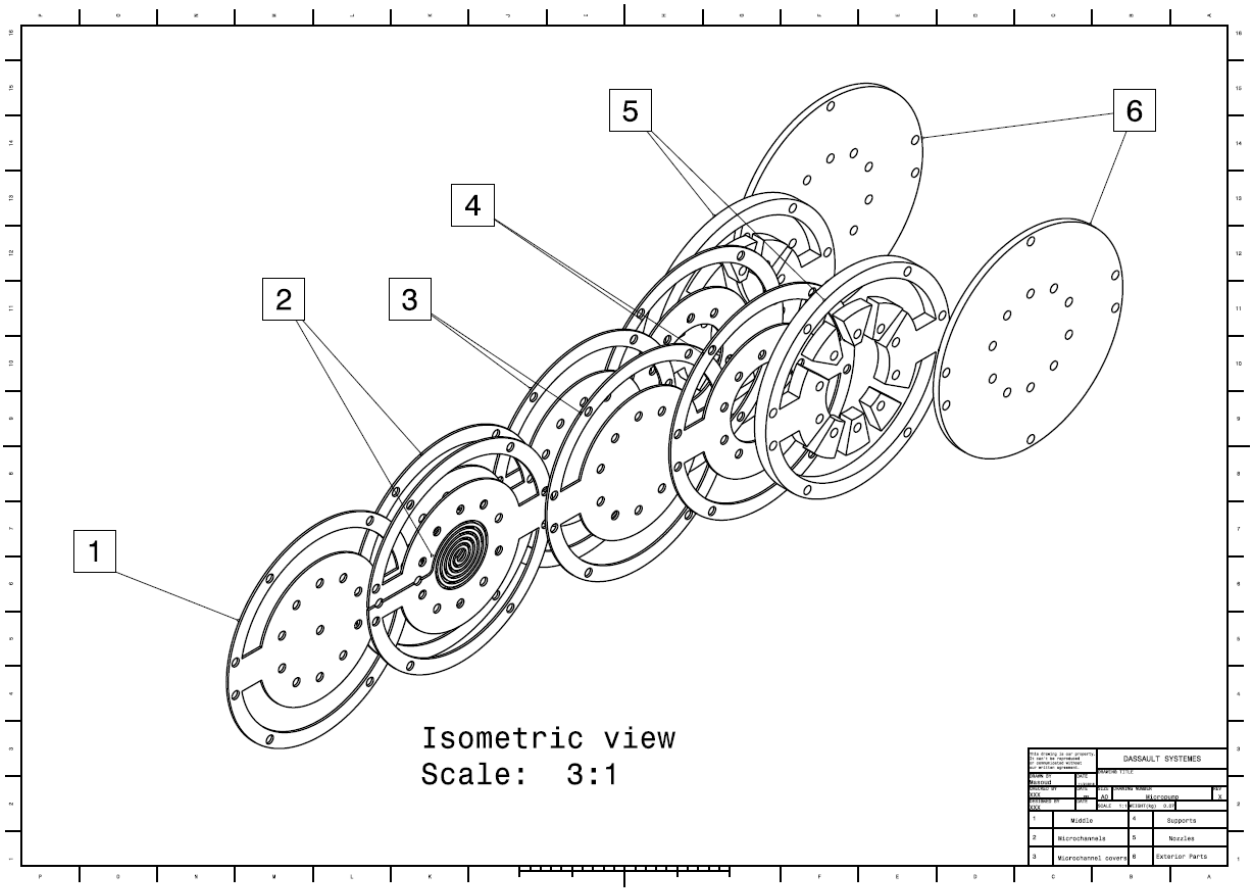
1
2
3
4
5
6
Isometric view
Scale: 3:1
DASSAULT SYSTEMES
Microcopper
A0
1 Middle
2 Microchannels
3 Microchannel covers
4 Supports
5 Nozzles
6 Exterior Parts

VITA

EDUCATIONAL BACKGROUND

- **PhD in Mechanical Engineering (GPA: 3.9/4.0)** **Aug 2016 – Aug 2021**
  Department of Mechanical Engineering – University of Mississippi, Oxford, MS, USA
  Advisor: Dr. Farhad Farzbod

- **Master of Science in Mechanical Engineering** **Sep 2011 - Sep 2013**
  Department of Mechanical Engineering - Isfahan University of Technology (IUT), Isfahan, Iran
  Advisors: Dr. Hamidreza Mirdamadi

- **Bachelor of Science in Mechanical Engineering** **Sep 2007 - May 2011**
  Department of Mechanical Engineering – Imam Khomeini International University (IKIU), Qazvin, Iran
  Advisor: Dr. Seyed Abbassosadat Sakak

- **Sadra High School** **Aug 2004 - Jun 2007**
  Qazvin, Iran
  Major: Mathematics and Physics

Thesis and Dissertation

- **PhD's Dissertation Title:** "Nonreciprocity Applications in Acoustics and Microfluidic Systems", University of Mississippi.
- **Master's Thesis Title:** "Analytical Measurement of Welding Residual Stress Using Critically Refracted Longitudinal (Lcr) Wave Technique", Isfahan University of Technology,
- **Senior Project:** "Analysis of Tensions in Pressure Vessels due to Explosion", Imam Khomeini International University,

ACADEMIC EXPERIENCE

TEACHING EXPERIENCE

- **Teaching Assistant** for Engr. 330 (Engineering Systems and Analysis) - Fall 2016, Fall 2017 and Fall 2018.
  Mechanical Engineering department at University of Mississippi, Oxford, MS, USA.
- **Lab Instructor** for "Mechatronics Systems and Engineering" – Spring 2018 and Spring 2019.
  Mechanical Engineering department at Kashan University, Kashan, Iran.

- **Teaching Assistant** for Engr. 323 (Fluid Mechanics) - Spring 2018.
  Mechanical Engineering department at University of Mississippi, Oxford, MS, USA.
- **Teaching Assistant** for Engr. 325 (Intermediate Dynamics) - Spring 2017 and Spring 2018.
  Mechanical Engineering department at University of Mississippi, Oxford, MS, USA.

RESEARCH EXPERIENCE

- **Graduate Research Assistant:** Fall 2016-Present.
  Mechanical Engineering department at University of Mississippi, Oxford, MS, USA.

PUBLICATIONS

JOURNAL PAPERS

1. **Naghdi, M**. and Farzbod, F., 2018. Acoustic nonreciprocity in Coriolis mean flow systems. The Journal of the Acoustical Society of America, 143(1), pp.230-236.

2. Farzbod, F., **Naghdi, M**. and Goggans, P.M., 2019. Using Liquid Metal in an Electromechanical Motor with Breathing Mode Motion. Journal of Vibration and Acoustics, 141(1), p.014501.

CONFERENCE PAPERS

1. **Masoud Naghdi,** Farhad Farzbod, Paul Goggans. Flexible Valvelss Pump for Bio Applications, International Mechanical Engineering Congress and Exposition, IMECE2019, November 11-14, 2019, Salt Lake City, UT, USA.

2. Amir Mirzaeinia, Mostafa Hassanalian**, Masoud Naghdi**. Flexible Harvesting Energy by Base Excitations of Troops' Backpacks for Charging Drones, AIAA Propulsion and Energy Forum and, August 19-22, JW Marriot Indianapolis, Indiana, 2019.